PREPARATION OF POWDER LAYERS IN SELECTIVE LASER SINTERING PROCESS

Marco Lupo

UNIVERSITY OF SALERNO

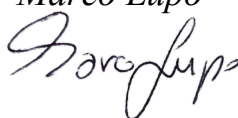*DEPARTMENT OF INDUSTRIAL ENGINEERING*

*Ph.D. Course in Industrial Engineering
Curriculum in Chemical Engineering - XXXIII Cycle*

Doctoral thesis in Chemical Engineering
PREPARATION OF POWDER LAYERS IN SELECTIVE LASER SINTERING PROCESS

Supervisors[1]
Prof. Massimo Poletto
Prof. Diego Barletta
Dr. Daniele Sofia

Ph.D. student
Marco Lupo

Ph.D. Course Coordinator
Prof. Francesco Donsì

Academic year
2020/2021

Publications

1. **Lupo, M.**, Sofia, D., Barletta, D. and Poletto, M. (2019) Calibration of DEM Simulation of Cohesive Particles. *Chemical Engineering Transactions*, **74**, 379–384.

2. Sofia, D., **Lupo, M.**, Barletta, D. and Poletto, M. (2019) Validation of an experimental procedure to quantify the effects of powder spreadability on selective laser sintering process. *Chemical Engineering Transactions*, **74**, 397–402.

3. Ruggi, D., **Lupo, M.**, Sofia, D., Barrès, C., Barletta, D. and Poletto, M. (2020) Flow properties of polymeric powders for selective laser sintering. *Powder Technology*, **370**(15), 288–297.

4. **Lupo, M.**, Sofia, D., Barletta, D. and Poletto, M. (2021) Calibration of DEM for cohesive particles in the SLS powder spreading process. *Processes*, **9**(10), 1715.

Table of contents

II

List of figures

IV

VI

List of tables

X

Abstract

Selective Laser Sintering (SLS) is an additive manufacturing process by means of which three-dimensional objects can be manufactured using a laser beam to selectively sinter powder particles. Many are the advantages of SLS, among which are the capacity to build high resolution and very complex shaped objects by using a range of materials. Because of these qualities, SLS is used in advanced applications, e.g. scaffolds for tissue engineering. However, one drawback of SLS is the quality of the powder layer, which depends not only on the powder flow properties but also on the operating conditions. In particular, spreading of powder is a crucial step. Collecting information about the spreadability, that is the capacity of the powder to be spread, is relevant to optimize the distribution and the layering of powder.

A new experimental setup able to simulate the powder spreading process and its DEM model were developed with the purpose of achieving this objective. The Johanson's model was applied to the compaction of the powder layer to understand whether it is possible to increase the density of the layer. Based on the results of the model, a new configuration was designed and built. It combines the action of the blade and of the roller so as to spread and compact the layer, respectively.

The Domo's Sinterline unfilled polyamide 6 3400 HT110 Natural was used as a test material. Layers of the powder were produced with a blade running at two different scrolling velocities, namely 3 mm s^{-1} and 3 cm s^{-1}.

An optical system was set up to observe the powder layer at the particle level. It consists of a microscope coupled with a camera, that can be positioned on the powder surface in defined locations.

Quality of the powder surface was analysed in terms of characteristic length of roughness, calculated by applying the power spectrum of the wavelet transform to greyscale images of the deposited layers. Comparison between the tests at different blade velocities showed slight differences in the powder surface quality. The slight dependence of surface asperities from the scrolling velocity of the blade would suggest that there is not a direct relationship between characteristic length of roughness and dimension of aggregates, which depends on the Bond number.

The effect of recycling the powder was also analysed suggesting that adequate preparation of the used powder and proper test conditions are necessary.

A DEM model was created to simulate the spreading of powders with the future aim of understanding the mechanisms and the powder properties which are responsible for good or bad quality of the layer. The Hertz-Mindlin (no slip) with JKR cohesive model was used to describe interparticle interactions.

Three different approaches were tried to calibrate the model parameters and the one based on the comparison between the experimental bulk density and porosity with those measured from the simulations turned out to be the right one.

DEM model was validated by applying the wavelet power spectrum to greyscale images of the layers obtained with the simulations and by comparing the characteristic length of roughness of the experimental layers with the simulated ones.

Therefore, the DEM model allows to quantitatively evaluate the quality of the powder layer, i.e. in terms of dimension of surface asperities, obtained through deposition in the same spreading conditions of the experiment. To the best of my knowledge, this procedure of analysis has been applied for the first time to experimental and simulated layers of additive manufacturing processes. Analysis of simulated powder layer can be used to choose the suitable spreading configuration for a certain powder or to properly engineer powders with desired particle properties to obtain good quality layers with a given spreading configuration.

Introduction and aim of the work

Additive Manufacturing (AM) or 3D printing is a rapidly developing manufacturing technology with the ability to create unique and complex multi-material artefacts directly from the raw material with a waste minimization.

Starting from three-dimensional model data, 3D printers can build objects by depositing layers of material until a desired shape is obtained. After the deposition, post processing is needed, which can include surface finishing, sintering, infiltration, depending on the used printing method (Bhushan and Caspers, 2017).

Interest in AM is growing in many applications, among which are biomedical, aerospace, buildings (Ngo *et al.*, 2018).

The expiry of earlier patents has given manufacturers the ability to develop new 3D printing devices, making AM more accessible. At the beginning, 3D printing has been extensively used by architects and designers to create aesthetic and functional prototypes, due to its rapid and cheap prototyping capability. Nowadays, 3D printing is used in various industries from prototypes to products. For example, in the biomedical field, AM is very useful to produce unique patient-customised products with relatively low costs (Ngo *et al.*, 2018). In the construction field, AM is even used to print houses (Wu, Wang and Wang, 2016).

AM allows to use many types of materials such as metals, ceramics, polymers, concrete and composites (Liu and Shin, 2019). Moreover, powders can be reused, making AM more affordable compared to traditional manufacturing methods. Other advantages are the time and cost reduction (Wong and Hernandez, 2012). Compared to Subtractive Manufacturing, in which material is removed from a solid block to carve out a part, AM has several advantages including fabrication of high-precision complex geometries, considerable material savings as the part is built in additive layers, flexibility in design, and personal customisation. However, 3D objects often have poor mechanical properties and anisotropic material properties, which limit the large-scale printing. Therefore, it is important, for example, to properly design the parts to avoid any anisotropic behaviour or weak points in

the object. Other disadvantages of AM processes are poor surface finish and low bonding between subsequent layers. Moreover, while small-scale production is relatively fast and economical, large-scale production of parts is generally not cost effective due to excessive time.

Among the AM processes is the Selective Laser Sintering (SLS) process.

In the SLS, after the powder layer deposition, particles are sintered by means of a laser beam. Deposition and sintering steps are alternated and repeated many times until the final artefact is obtained. (Sing *et al.*, 2017). Although many are the parameters which affect the quality of the artefact, such as the sintering parameters (Williams and Deckard, 1998; Bertrand *et al.*, 2007), however the structural, mechanical and thermal properties of final object are strongly dependent on the quality of spreading (Ziegelmeier *et al.*, 2015; Sofia, Barletta and Poletto, 2018). Therefore, in recent years many studies have been carried out both from modelling (Chen *et al.*, 2017a; Meier *et al.*, 2019; Wang *et al.*, 2020) and experimental (Escano *et al.*, 2018; Ahmed *et al.*, 2020; Ruggi, Lupo, *et al.*, 2020) points of view to understand the factors which affect the homogeneity of the deposited powder layer. However, very few methods have been proposed in the scientific literature by which it is possible to quantify the quality of the spread powder layer in the SLS process and, more in general in AM processes. Quantitative analysis of quality of the layer means to find some variables, by which it is possible to define how good or bad is the quality of the deposited powder layer. Therefore, new and alternative methods of quantitative analysis of the quality of the powder layer are necessary to achieve this goal.

Another limit of the SLS process is the use of powders specifically designed so as to be easily and properly spread. However, getting particles with desired shapes, usually spherical and with a high spreadability, requires high costs of production, which result in high sales costs of the powder. For this reason, new spreading configurations need to be thought with the purpose of obtaining layers with a good quality even when using more irregular shape or edged particles and/or without flow enhancers.

The strategy adopted in this thesis work to achieve these objectives has been to:

1) develop a new experimental setup with the possibility to use conventional as well new and different spreading configurations in order to study experimentally the quality of the deposited powder layers and find the best configuration for the tested powder;
2) develop a DEM model to simulate the deposition of the powder layer in different spreading configurations to try to understand the mechanisms and the powder properties which determine the formation of a good quality powder layer;
3) draw up methods of qualitative and quantitative analysis of the quality of the powder layer to demonstrate the suitability or inadequacy of the

XIV

spreading configuration and/or the type of powder employed and to compare experiments and model results.

The details about the setup are reported in paragraph III.2.1.1, the DEM model is described in paragraph IV.6 and the procedures to characterize the layers are reported in paragraphs III.4, III.4.2 and IV.6.1.

Chapter I
Selective Laser Sintering

I.1   Introduction

Selective Laser Sintering (SLS) belongs to the category of powder bed fusion manufacturing technologies, which use a laser beam as an energy source to fuse powder particles together (Sing *et al.*, 2017).

In the SLS various materials can be used: polymers, metals, alloys, combinations of metals and polymers, and combinations of metals and ceramics (Tang, Chiu and Yen, 2011). Among the polymers used are acrylic styrene and polyamide. It is also possible to use composites or reinforced polymers, such as polyamide with fiberglass or metals like copper. For metals, a binder is necessary, like a polymer, which is then removed by heating (Wong and Hernandez, 2012). Examples of metal/metal and ceramic/metal composites are iron/copper and tungsten carbide/copper, respectively.

In a SLS machine, the chamber is heated to almost the melting point of the material, then the platform inside the powder delivery cylinder (Figure I.1) raises a certain level while the platform inside the fabrication cylinder goes down a distance equal to a single powder layer thickness, that is of around 100 μm. In fact, such a dimension has to correspond to approximately 2÷3 times the average particle size in order to ensure that the majority of particles receive direct contact from the laser, rather than from particle-to-particle conduction. (Goodridge, Tuck and Hague, 2012). Then, the particulate delivery tool, such as a roller or a blade, moves from left to the right in order to displace the powder on top of previous layers and create a new powder layer. Once the layer is obtained, on the basis of a CAD file, a laser beam fuses the particles at the molecular level, due to the elevated local temperature on the surface of the grains (Ngo *et al.*, 2018). The whole procedure is repeated many times until the completion of the object.

Powder size distribution and layer packing density determine the density of the printed part. Therefore, these properties are crucial to the efficacy of this method (Utela *et al.*, 2008).

Laser power and speed of scanning are the main parameters affecting the sintering process (Lee *et al.*, 2017).
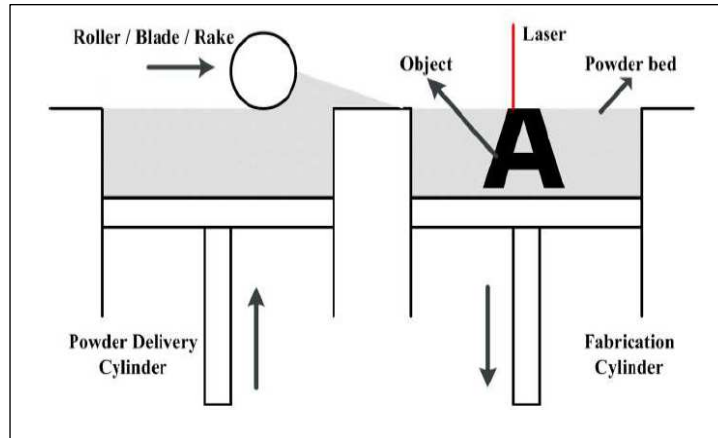
Figure I.1 *Schematic representation of the SLS process* (Xiang *et al.*, 2016).

I.1.1   Advantages and disadvantages

SLS has many advantages:
1)   wide range of materials can be used;
2)   unused powder can be recycled;
3)   the powder bed is used as the support, which overcomes difficulties in removing supporting material;
4)   objects of higher resolution due to the laser precision can be produced (Fina *et al.*, 2017);
5)   products with complex shapes can be fabricated (Danezan *et al.*, 2018);
6)   SLS can be used for advanced applications, e.g. scaffolds for tissue engineering;

However, SLS could also be characterized by some drawbacks:
1)   slow process;
2)   high costs;
3)   high porosity when the powder is fused with a binder;
4)   low part density;
5)   low resolution of the object due to the limitations of powder-based material;
6)   low strength of the object (Wong and Hernandez, 2012; Bhushan and Caspers, 2017; Ngo *et al.*, 2018).

Some comments about SLS are:

- resolution is highly dependent on particle size and machine (Bhushan and Caspers, 2017);
- agglomeration and oxidation issues occur with smaller particles. Therefore, there is the need to avoid oxidation by executing the process in an inert gas atmosphere;
- SLS requires post processing;
- the process has to occur at constant temperature, which has to be higher than the ambient one but not necessarily close to the melting point of the powder (Ruggi, Lupo, *et al.*, 2020);

I.1.2 Particulate delivery mechanisms

In addition to the individual powder flow characteristics, the particulate delivery mechanism also has some influence on the successful deposition of powder over the build area.

Van der Schueren et al. (Schueren and Kruth, 1995) made a comparison among three different kinds of particulate delivery tools: scraper blade, counter rolling cylinder and slot feeder (Figure I.2).
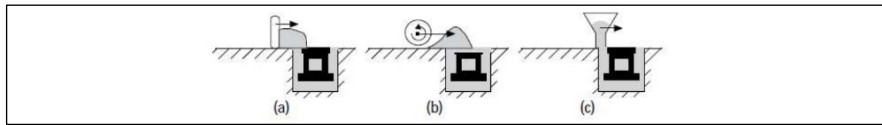
Figure I.2 *Three different particulate delivery mechanisms: (a) scraper blade, (b) counter rolling cylinder and (c) slot feeder* (Schueren and Kruth, 1995).

The main advantages and drawbacks of these mechanisms are reported in Table I.1.

Table I.1 *Comparison among the scraper blade, the counter rolling cylinder and the slot feeder.*

PARTICULATE DELIVERY TOOLS	ADVANTAGES	DRAWBACKS
SCRAPER BLADE	Does not require highly flowable powders.	1) Friction between the new and the underlying layer; 2) Low smoothness of the layer surface due to irregularities in the powder material, e.g. conglomerates of some particles;

3

		3) Impossibility of a direct compaction of the layer.
COUNTER ROLLING CYLINDER	1) Lower irregularities on the layer surface; 2) Possibility to compact (e.g. by means of a vertical vibration during the deposition); 3) Does not require highly flowable powders.	The underlying layers shear due to the friction of the powder heap pushed in front of the deposition device.
SLOT FEEDER	Minimal friction between the newly deposited powder and the powder bed underneath.	1) Does not offer an intrinsic controlled way of compacting the powders; 2) Requires highly flowable powders.

In the case of the *scraper blade*, a surplus of powder has to be put in front of the blade to guarantee the formation of a whole new layer. This surplus causes more weight of the powder on the surface of the previous deposited layer, causing friction between the powder heap and the underlying layer. Moreover, the fixed contact line between the scraper blade and the underlying layer may cause the formation of grooves in the layer if the powder heap contains some irregularities, e.g. clusters of particles. Finally, this approach does not allow the layer to be compacted after its deposition.

In the case of the *counter rolling cylinder*, the problem of the continuous contact line of the blade is partially solved due to its rotatory movement. As a result, only short grooves may appear along the underlying layer. The cylinder can also compact the layer if, for example, it vibrates during the spreading. In fact, vibration resembles the tapping operation, allowing the increase of density of the deposited layer, which in turn leads to higher density of the sintered layer and higher strength of the object (Ziegelmeier *et al.*, 2015)

Both the blade and the roller (cylinder) do not need high flowability of the powder. On the contrary, the *slot feed* requires high powder flowability because of the way in which the powder is deposited. In this case, the powder flows out of the feeder vertically. Therefore, the interparticle forces have to be minimised, for example by reducing the humidity of the environment or by using spherical particles. However, the great advantage of the feeder is the gap

between the slot and the underlying layer, which reduces the friction between the falling powder and the deposited layer. Like for the blade, also the feeder does not allow the compaction of the layer.

According to Van der Schueren et al., the best solution is a combination of the slot feeder and the cylinder, which is not counter rolling, but rolls in the direction of motion, since its only task is to compact the deposited layer without spreading it.

They also suggested to add a vertical vibration on the cylinder to improve the density of the compacted layer. Such a solution was adopted by N.K. Roy et al. (Roy and Cullinan, 2015) to achieve layer thicknesses of few microns in selective laser micro sintering, which is a modification of selective laser sintering. Selective laser micro sintering was developed by Laserinstitut Mittelsachsen e.V. to generate metal micro parts with a structural resolution of < 12 μm (Regenfuss *et al.*, 2004). Nanopowders tend to form agglomerates because of their high surface energy, due to high surface area/volume ratios, and the presence of attractive van der Waals forces, which start dominating the gravitational forces. To overcome this problem, N.K. Roy et al. presented a new powder spreading mechanism design in which vibration is used to produce a uniform powder distribution in the bed and increase the powder bed packing density.

The main steps are: 1) spreading of the powder layer by using a precision blade; 2) compaction of the deposited powder layer by using a vibrating counter rolling cylinder.

The importance of achieving higher packing density has been demonstrated by Streek and his co-workers (Streek *et al.*, 2008). In laser micro sintering of metal powders there is the problem that particles, because of the diameter of a few micrometres, settle to very poor densities, which are lower than those achieved with powders in the conventional SLS. To compensate the poor density of the powder layers, a solution could be to increase the density of the powder layers by compacting the layer before the sintering. The steps of this process are: 1) the fabrication cylinder, where the powder is sintered, is lowered by a height of several powder layers; 2) it is loaded with the powder; 3) it is closed with an external lid; 4) the piston, which holds the cylinder, raises a certain height, compressing the powder against the lid; 5) the lid is pulled off horizontally; 6) the layer is sintered. Then, the whole procedure is repeated many times until the creation of the final object. The results of their experiments showed that this method allows to obtain higher sinter densities and a lower sinter surface roughness compared to the application of short and intensive laser pulses without compaction.

Niino and Sato (Niino, 2009) demonstrated the advantage of powder compaction in SLS. They presented an experimental method that enables powder compaction without adding major change in mechanism of commercially available SLS systems. First, a counter rolling cylinder spreads the powder; then, after the piston raises a certain height, the cylinder rotates

in the direction of motion to compress the powder layer. They defined the compaction factor, which indicates how much the powder bed is compacted. It is ≥ 0. The higher the compaction factor, the higher the compression of the layer. They also defined the unsintered powder packing density in a hollow box. They found that the lower the roller speed, the higher the packing density. The main difficulty of this method is to properly combine the roller scrolling speed, the roller rim speed and the compaction factor in order to have a good layer compaction without dragging the previous layers. In the case of polyamide powder, a small increase in packing density led to a significant reduction of the porosity. Another interesting result was the reduction of curl distortion, a phenomenon typical of insufficient powder bed temperature control over the whole build area, when the layer is compressed. Compaction also improved the mechanical properties of the final object in terms of yield stress, elongation at break, flexural stress, flexural modulus and impact strength. These results can be explained saying that the compressing force increases adhesion between particles or layers.

In the case of amorphous plastic, like polystyrene, a compaction factor of 1 led to an increment of density of the sintered, which is still not sufficient to use the sintered object as structural part.

Sofia et al. (Sofia, 2019) also studied the effect of the compression of the powder bed, composed of glass beads with different average particle diameters, by using a roller which rotates counterclockwise. They found that the compression process loses effectiveness with the increasing of the particle diameter. The effect of compaction has been measured in terms of stiffness of the compressed powder layer, by means of the indentation test, and of tensile strength of the sintered powder layer, by means of a bending test. In particular, the final sintered resistance increased by 198% in the case of compressed fine powder.

Current designs of recoating blades do not allow to uniformly deposit fine powders due to powder grain agglomeration; however, optimisation of the angle and shape of the blade was investigated.

For example, Haeri (Haeri, 2017), by means of a set of Discrete Element Method (DEM) simulations, tried to optimise the geometry of the blade to obtain the lowest powder bed void fraction, that is the highest bed compaction. The blade profile was parametrised using a super-ellipse with three geometrical parameters, which control width, height and the overall shape of the profile. He demonstrated that geometric optimisation of a blade profile is a possible alternative to using more complex spreading devices. In fact, the optimised blade spreader generated a bed with volume fractions similar to that of the roller (cylinder) and even a smoother bed surface. In addition, compared to the roller, the optimised blade is less sensitive to the increase of the translational velocity and at higher velocities it allows to have a lower powder bed void fraction. This result translates into faster production without compromising the quality.

In another work, Haeri and his co-workers (Haeri *et al.*, 2017) studied the spreading of non-spherical particles in AM by using DEM simulations. They compared the roller and the blade to understand which is the best tool to obtain better powder bed qualities in terms of surface roughness and solid volume fraction. The results of their study confirm what was experimentally demonstrated by Van der Schueren at al. (Schueren and Kruth, 1995), namely in the same operating conditions the roller significantly outperforms the blade. In fact, the results show that the blade generates a bed with higher surface roughness and smaller powder bed density compared to the roller. This can be explained by saying that the blade has an inadequate contact with the bed because interacts with the bed at a single point (its edge), which causes particle dragging, and degrades the bed quality. At the contrary, the roller provides a large contact area and allows for gradual particle rearrangement. In fact, the results show that the blade yields a bed with higher surface roughness and smaller powder bed density compared to the roller. Also, the translational velocity influences the powder bed quality. In fact, the higher the velocity, the worse the bed quality for both the roller and the blade. Of course, it is necessary a trade-off between an acceptable bed quality and a reasonable production rate, depending on the operational constraints.

Comparison between different particulate delivery mechanisms has revealed that it is likely that no single spreading tool is better than the others but a proper combination of them could result in good quality of the powder layers.

I.1.3 Powder flowability in the spreading process

Prescott and Barnum (Prescott and Barnum, 2000) defined the powder *flowability* as the capacity of a given material to flow in a desired manner in a specific equipment. Therefore, the same material can behave differently in different flow equipment conditions. In SLS, flowability plays a key role because it directly affects the quality of the sintered components (Amado, Schmid and Wegener, 2013). In fact, one of the main bottlenecks in AM is the uniform spreading of powder layer by layer (Escano *et al.*, 2018). Good dispersion conditions are necessary to have higher powder packing, more homogeneous powder layers and higher smoothness of their surface, which in turn lead to better mechanical and surface properties of the final object (Amado *et al.*, 2011)(Ziegelmeier *et al.*, 2015). At contrary, higher porosity or large roughness of the layer could lead to weaker bonding between the layers and, consequently, poor mechanical performance of the artefact (Haeri *et al.*, 2017). Therefore, it is important to understand whether a powder is suitable to be used in the SLS process by evaluating its capacity to be spread (Krantz, Zhang and Zhu, 2009).

In literature various methods to evaluate the flowability of powders have been reported, but very few characterization techniques, able to predict the *spreadability* of powders in AM processes, have been presented.

Spreadability is the ability of powders to be uniformly spread across a build plate (Snow, Martukanitz and Joshi, 2019).

Schmid and Amado (Schmid *et al.*, 2014) proposed a simple method to measure the Hausner ratio (HR), which is the ratio between tap and bulk density, and gives an idea of the capacity of the powder to flow. The bulk density can be obtained by simply pouring the powder in a predefined volume while the tap density corresponds to the bulk density of a powder after that the powder has reached a more consolidated state by tapping, jolting, or vibrating the measuring vessel. Based on the definition of the HR, they classified the powders as follows:

- HR < 1.25 corresponds to high powder flowability;
- 1.25 < HR < 1.4 corresponds to decreased powder flowability;
- HR > 1.4 corresponds to a cohesive powder.

Therefore, powders suitable for SLS should have HR < 1.25.

Often individual measured results, obtained from different laboratories on the same material, can be different because of some possible factors such as the operator, the equipment and its calibration, the environmental conditions during the test (temperature, humidity, etc.). Schmid and Amado proposed a simplified procedure for determining bulk and tap density, listing the instructions to follow rigorously. The procedure requires only a plastic measuring cylinder with a volume of 100 ml and a powder funnel. The results of different laboratories, which took part in an interlaboratory comparison, showed that this simplified procedure of determining bulk and tap density is adequate to qualify and distinguish between different SLS powders.

However, HR does not seem the ideal way to evaluate the flowability of powders in SLS, where thin powder layers are created and often no significant compression or tapping is applied to the powder.

Often, the ring shear cell tester (Schulze, 2010) is used to evaluate the powder properties and the powder flowability, which is assessed from the flow factor (FF), namely the ratio between the major principal stress at steady state flow, called major consolidation stress, and the unconfined yield strength (Jenike, 1964). According to the Jenike's classification, the behaviour of a powder can be classified as follows:

1) FF < 1, hardened
2) 1 < FF < 2, very cohesive
3) 2 < FF < 4, cohesive
4) 4 < FF < 10, easy flowing
5) 10 < FF, free flowing

However, this valuation technique does not seem suited for the flowability evaluation in the SLS process, because in the ring shear cell the powder is

tested under a compressive load, that is a condition which may differ from that experienced during the spreading.

Ruggi et al. (Ruggi, Lupo, *et al.*, 2020) proposed a procedure to derive an assessment of interparticle forces from powder flow properties, evaluated with the ring shear cell, in order to evaluate the granular Bond (Bo) number. The latter is the ratio between the interparticle force for the unconsolidated material and the particle weight and appears as the most appropriate measure of powder propensity to flow in the SLS process. Comparison between the inferred values of the Bo number and the quality of layers produced under typical SLS working conditions indicates that the Bo number of the powder should not exceed 100 in order to obtain satisfactory layer quality after spreading it with a blade. By using the High Temperature-Annular Shear Cell (HT-ASC), developed at the University of Salerno by Tomasetta et al. (Tomasetta, Barletta and Poletto, 2013), Ruggi et al. studied the effect of temperature on the flow properties of three different polymeric powders, namely polyamide 12, polyamide 6 with and without flow promoter, in order to properly take into account real temperature conditions relevant to SLS. In particular, the Bo number was evaluated at temperatures from ambient conditions to values close to the melting temperature of the polymers. Ruggi et al. demonstrated that the tested flowability significantly worsens at temperatures $20 \div 30\ °C$ lower than the powder melting point.

Amado and his co-workers (Amado *et al.*, 2011) used a setup, called Revolution Powder Analyzer (Figure I.3), in order to reproduce the dynamic behaviour of the powder during the spreading in the SLS. This new characterization indicator could help to rank powders for the SLS.

The Revolution Powder Analyzer, made by Mercury Scientific Inc., consists of a rotating drum and an image acquisition system. Both the lateral sides of the drum are covered with transparent glass, in order to see the powder behaviour inside the drum. In fact, by means of a backlight source, it is possible to record the powder surface boundary and the cross-section of the powder. It is possible to adjust the turning speed. In this way two different tests can be performed: the flowability test, at low values of the speed; and the fluidization test at the higher ones.

Figure I.3 *Revolution Powder Analyzer.*

Amado et al. tested different SLS commercial powders with different polymeric powders namely polyamide 12, a thermoplastic elastomer and copolymer polypropylene. In order to evaluate the flowability of the powders, they measured the following characterization parameters: the avalanche angle, the surface fractal and the volume expansion ratio (VER).

The first one (Figure I.4) corresponds to the angle that the powder surface contour forms with a horizontal line in correspondence with the maximum potential energy before the fall of the powder. The higher the avalanche angle the poorer the flowability.

The surface fractal (Figure I.4), which corresponds to the fractal dimension of the free surface of the powder, is an indication of the rugosity of the powder surface. If the powder surface is smooth, the surface fractal is close to one, if it is rough the surface fractal is greater than one. A low surface fractal means low rugosity and therefore a good distribution of the powder.

VER is the ratio between the volume measured inside the drum and the volume occupied by the powder in the sample container before the filling of the drum and after the tapping procedure. The lower the VER, the better is the capacity of powders to flow.

Therefore, optimal SLS powders should have low avalanche angle, surface fractal and VER.
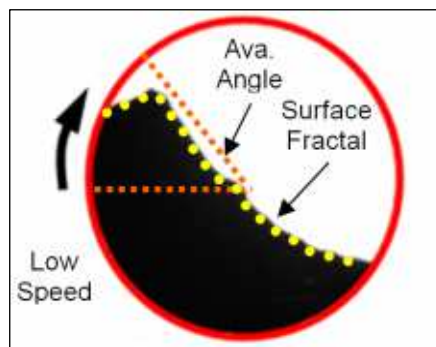
Figure I.4 *Avalanche angle and surface fractal.*

However, by analysing the results, Amado et al. observed that sometimes variations of VER and of surface fractal with the material are not consistent. For example, the tested thermoplastic elastomer revealed to have higher surface fractal than a polyamide-based material, but lower VER. Therefore, Amado et al. combined VER and the surface fractal in one parameter in order to consider both the effects and give a more realistic prediction of the flowability of powders. Such a parameter is the Rank Index, which is the ratio between VER and the surface fractal. The higher the index, the higher the ease of processing the powder in SLS.

Later Amado and his co-workers (Amado, Schmid and Wegener, 2013) equipped the aluminium rotating drum with a heated core cylinder, able to heat the powder from 25 ºC up to 120 ºC. The objective was to evaluate the flowability at temperatures higher than the ambient one and closer to those used in conventional SLS process, where powder is heated to a temperature just below the melting point of the material (Aldahsh, 2013).

They tested a commercial polyamide 12 (PA2200, EOS GmbH, Germany) and a random co-polypropylene at different temperatures and discovered that the temperature has a clear effect on the powder flowability. In particular, the glass transition temperature defines a change between different behaviours. For example, there is a reduction of the surface fractal value above the glass transition temperature for PA2200, which indicates a better flowing capacity and suggests an increased and homogenous powder packing deposition.

Lumay et al. (Lumay *et al.*, 2012) used the GranuDrum, that is a rotating drum produced by the Granutools, to evaluate the powder flowability at different rotating speeds corresponding to different applied shear rates. They evaluated the powder flowability of non-cohesive powders through the flowing angle. In particular, the higher the cohesion, the higher the flowing angle. Similarly, the parameter corresponding to the fluctuations of the flow can increase for both the increase of cohesive forces and the elongation of the grains. However, when used alone, this method does not allow to distinguish between a better and a worse flowability behaviour of cohesive powders. For example, in the case of "Francine fluid" the parameter corresponding to the fluctuations of the flow is low, but the flowing angle is higher compared to that of other flours. This result suggests that complementary methods for the flowability evaluation are necessary.

The Freeman FT4 Powder Rheometer (Freeman, 2007) is an instrument by means of which the torque, necessary to rotate a twisted blade impeller in the powder bed, is measured and the specific energy is inferred. The latter measures the resistance to flow of powders when close to a non-consolidated or stress free condition and hence it is an indirect measurement of the powder flowability. The higher the specific energy the lower the flowability of the powder.

I.1.4 Methods of analysis of quality of the powder layer: state of the art

An interesting work about the analysis of quality of powder layers was done by Irene Yee (Yee, 2018). The Lawrence Livermore National Laboratory designed a powder spreading machine that simulates the powder bed fusion process without the laser, and Irene Yee tested the machine with the aim of studying how the dosage rate and the blade velocity affect the surface roughness of the powder layer and the particle size distribution (PSD) in different points of the layer. The dosage rate is a number which is multiplied by the desired layer thickness to choose a sufficient initial amount of powder in the powder delivery cylinder (Figure I.1). In fact, the higher the initial powder bed, the higher the probability to complete a powder layer in the fabrication cylinder.

Yee studied the 316L stainless steel powder for Selective Laser Melting (SLM), which differs from the SLS because the particles are completely molten rather than at molecular level (Kruth *et al.*, 2004).

In the tests, the layer thickness was set at 30 μm, while the dosage rate at 2, 3 and 4. The blade velocity was set at 100 and 200 mm s^{-1}.

Surface roughness of powder layers was evaluated by using the Mikrotron 1362 camera, with the lens facing downward for taking photos of the layer. 9 different regions across the surface of the layer were chosen to analyse the quality of the layer in different points.

The macro camera lens was unable to capture individual powder particles but was able to identify clusters of them. However, images provided qualitative insight about the surface quality of the layer.

Proper lighting was chosen to have high contrasts, being the images in greyscale and given the fine grain size and smooth texture of the powder. However, to maintain consistent lighting, the light would have to move with the camera.

All the images taken were processed by using a MATLAB code.

The method used to quantify the surface quality or roughness for comparison of the 9 regions across the surface of the layer consisted of the measurement of the brightness to darkness ratio for each region in combination with the pixel area.

After that the images were converted to binary, the number of bright pixels (B) and dark pixels (D) were counted and the dimensionless ratio B/D was measured for each image. Lower B/D ratios corresponds to a worst surface roughness.

Yee demonstrated that, in relation to surface roughness, the B/D ratio did not indicate the size of objects. In fact, the B/D value does not account for size of objects, just the total white and black areas, and hence the size, which is crucial for the evaluation of the surface roughness, is lost. Therefore, Yee looked at pixel area means and standard deviations.

Pixel area is the pixel count of a closed white object surrounded by background pixels. Objects with a higher pixel area correspond to a larger size, whereas those with lower pixel area are smaller. Therefore, the higher the pixel area the worst the surface roughness. The smaller the pixel area the smoother the surface quality.

The standard deviation of the pixel areas in an image would provide a good idea of the spread of the data, indicating how rough or uneven the powder surface is qualitatively. The smaller the standard deviation, the more even the surface.

Yee also looked at PSD in the 9 regions. For this purpose, Yee used a frame with an inner grid made of 9 squares (Figure I.5). The frame with the inner grid was put on the layer in order to divide it in 9 different regions for sampling. The walls of both the frame and the grid were thin sheets of metal in order not to displace too much the powder during the placing of the grid. The powder was then scooped out from each region and placed in a plastic container. PSD for powder contained in each sample was measured.

Some interesting experimental results are:

1) Repeated tests were not consistent, as demonstrated by different pixel area mean and standard deviation from run to run;

2) Pixel area mean and standard deviation little differ with dosages rates of 3× and 4× compared to a 2× dosage rate;

3) The higher the blade velocity, the worse the quality of the layer surface, as demonstrated by higher pixel area means and standard deviations;

4) The layer surface increases in surface roughness in the direction of the spreading.
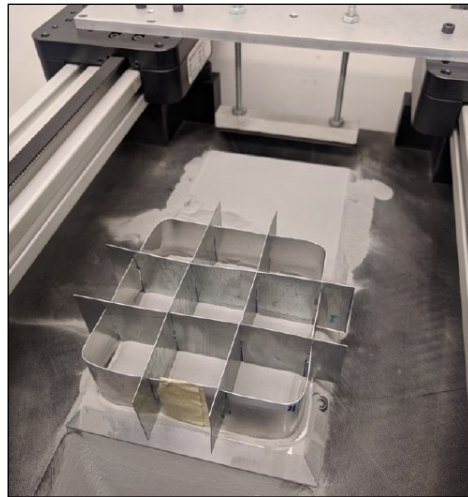
Figure I.5 *Sampling grid placed onto the build plate.*

Ahmed at al. (Ahmed *et al.*, 2020) proposed a simple technique for assessing the powder spreadability. A cutter blade, with a segment cut along its length to produce a gap, is used to manually spread a small heap of powder above an abrasive paper as a fully rough frictional base. The powder was placed on the paper by using a mold and then swiped by a blade manually. The produced layer was then immobilised using an adhesive spray, and the quality of the layer surface was analysed using the scanning electron microscopy (SEM) and MATLAB to check the uniformity of the spread layer. The test was repeated three times for a number of blades of different gap heights, between 45 and 135 μm, that is multiples of D_{90} by number (i.e. the particle size, based on the projected-area diameter, for which 90% of particles by number are smaller than this value). The spreadability of powder was quantified by measuring the dimension of the empty patches of the spread layer and the frequency of formation of empty patches. They both were evaluated by image analysis of scanning electron micrographs. Results showed that both decrease significantly with increasing gap height. Large empty patches were formed in small gap heights and are a manifestation of transient jamming (Nan *et al.*, 2018) of the powder in the heap over the gap. Ahmed at al. proposed a criterion to identify an empty patch and predict its location along the spreading direction.

Snow et al. (Snow, Martukanitz and Joshi, 2019) constructed and used a spreadability testing rig to study the ability of powder feedstock for metal powder bed fusion (PBF) to spread across a machined build plate. They measured 4 different quantitative powder spreadability parameters by using data collected from various sensors. They demonstrated that only 3 of them were viable: the percentage of the building plate covered by powder, the rate of powder deposition, and the rate of the change of the avalanching angle. These parameters were used to quantitatively assess powder spreadability.

Snow et al. showed that these parameters have a significant dependence on the angle of repose. Increasing the angle of repose resulted in significantly worse powder spreading, i.e. poor building plate coverage and powder clumping. Other processing parameters, such as the recoating speed and the blade material were shown to also influence the spread quality.

Escano et al. (Escano *et al.*, 2018) studied particle-scale powder dynamics during the powder spreading process by using in situ high-speed high-energy x-ray imaging. They quantified the evolution of the repose angle, the slope surface speed, the slope surface roughness of the powder front during the spreading process, and the dynamics of powder clusters at the powder front as indicators of powder flow behaviour during spreading. From the experiments they observed that smaller average size particles have reduced slope surface flow speed and higher flowing variations. These results are consistent with instabilities found in the dynamic repose angle, that is the average repose angle during the powder spreading. In fact, powders with smaller average

particle size showed a higher dynamic repose angle, larger fluctuation, and a higher standard deviation.

Powders with larger average particle diameter showed lower average slope surface roughness and better flowability compared to the powder with smaller average particle diameter.

Analysis of two different powder agglomerates show that they have slower average flow speed than the slope surface low speed of the powder. This information indicates that the clusters could not easily flow through the slope surface.

Van den Eynde and his co-workers (Van den Eynde et al., 2015) introduced an alternative technique to determine powder flow quality for SLS. The setup (Figure I.6) consists of a spreading blade which distributes and deposits the powder sample to form a thin layer on a measurement plate. The thickness of this layer can be regulated by adjusting the distance between the spreading blade and the plate, which rests on a balance. The balance provides a measurement of the layer weight and, being the layer dimensions known, also of the layer density (ρ_{layer}).

ρ_{layer} is a relevant parameter for SLS because the higher the layer density, the lower the artefact porosity and the better the object accuracy (Ziegelmeier *et al.*, 2015).

They defined a dimensionless density, called packing density (ρ_P), to make a quantitative comparison among different polymeric powders. ρ_P is defined as the ratio of ρ_{layer} to the material density of the polymer (ρ_m):

$$\rho_P = \frac{\rho_{layer}}{\rho_m} \tag{1}$$

Moreover, they defined the maximal packing density ($\rho_{P,max}$), which is given by the ratio between the dense or tapped density (ρ_{tap}) and ρ_m.

ρ_{tap} is roughly the maximum possible density of the powder. In fact, when a container of powder is subjected to tapping, there is a reduction of friction among the particles, which therefore improves their packing.

$\rho_{P,max}$ allows to exclude the geometrical limitations of the powder, given by the particle geometry and size distribution.

Finally, they defined an index, the packing ratio (PR), which does not consider the material density as well as the geometrical limitations of the powder but looks only at the powder flowability. PR is defined as the ratio between the ρ_P and $\rho_{P,max}$, or alternatively between ρ_{layer} and ρ_{tap}:

$$PR = \frac{\rho_P}{\rho_{P,max}} = \frac{\rho_{layer}}{\rho_{tap}} \tag{2}$$

15

PR is similar to the inverse of HR, but in the definition of the HR there is the bulk density of freely poured powder instead of the layer density. The layer density is different compared to the bulk density because different is the flow field. Therefore, the PR is a more appropriate index compared to the HR because considers the actual state of stress of the powder during the formation of the layer. The higher the PR, the denser the sintered parts.
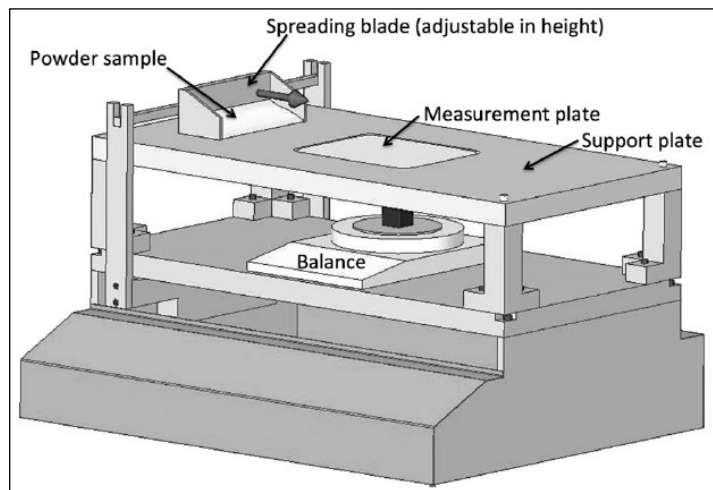
Figure I.6 *Powder spreader device for the measurement of the packing ratio (Van den Eynde et al., 2015)*

Van den Eynde et al. tested the following powders: three different kinds of polyamide 12 (PA12), which differ a bit from each other for the average particle size and for the smoothness of particle edges; polystyrene and polymethylmethacrylate, which consist of monodisperse spheres; and thermoplastic polyurethane (TPU), characterized by very irregular particle shapes and sizes. For each of them they measured both ρ_P and PR. They also evaluated qualitatively the layer quality by observing the layer surface.

The spherical powders showed the highest packing densities and packing ratios and the layer formed presented the highest smoothness.

PA12 formed layers of sufficient quality for SLS. TPU particles formed layers with defects and sometimes the layers were incomplete.

The results do not seem to surprise, since irregular and edgy shaped particles naturally tend to interlock with each other forming cakes, arches and voids inside the powder and hence causing poor flowability, higher cohesive behaviour and shear stresses. On the contrary, particles with a more spherical shape and smooth surface have generally higher flow capacity (Fu *et al.*, 2012).

Van den Eynde et al. (Van den Eynde et al., 2017) also proved that the temperature can affect the flowability of powders. In fact, above the glass

transition of the polyamide PA12 2200, distributed by EOS, there was a slight increase in the packing ratio.

I.1.5 Powder characteristics required in the SLS process

The creation of new powders suitable for the SLS process is not easy as a lot of material properties have to be fulfilled. Characteristics of these powders such as the flowability, the optical and the thermal properties depend on the material production process as well as the spreading in the SLS process (Figure I.7). The production process defines the kind of powder. If the powder is a mixture, composed of different phases, the production process defines the structure, the composition and the rheological behaviour of the phases. However, the spreading process can influence the capacity of the powder to create suitable powder layers. The density of these layers depends on both the state of stress experienced by the powder during the spreading, which is a function of the particulate delivery mechanism used, as well as the characteristics of the powder, namely the particle shape, the particle size distribution, the characteristics of the particle surface such as the level of smoothness, which are consequence of the production process adopted to obtain the powder.
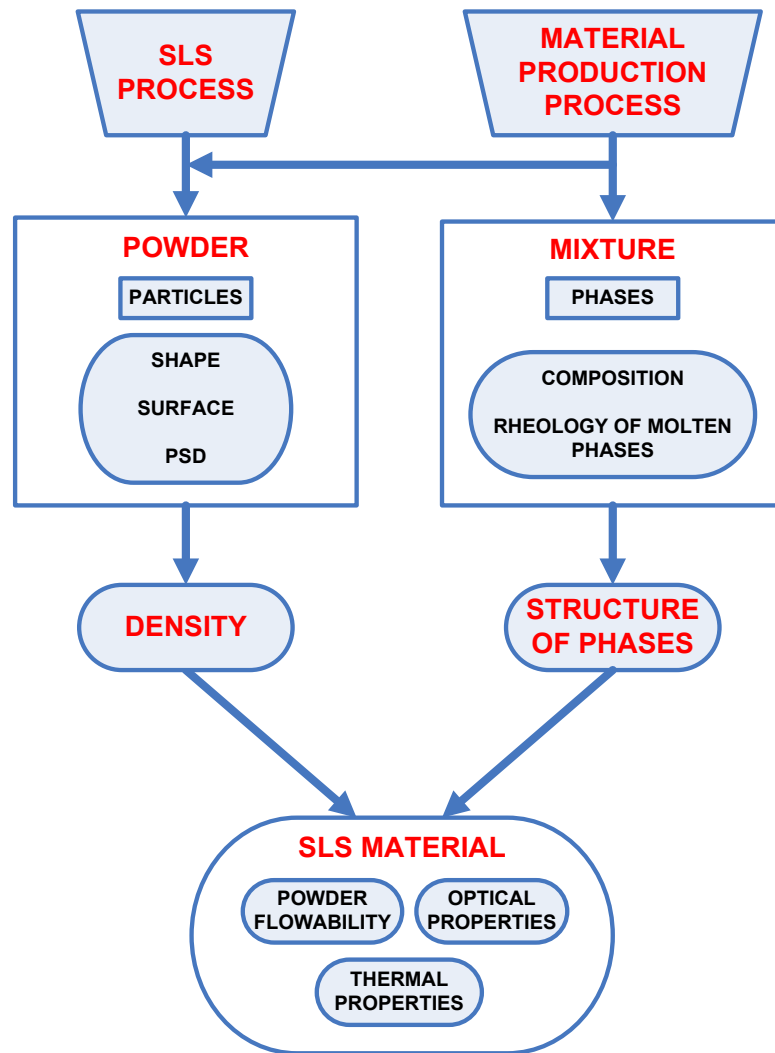
Figure I.7 *Properties of a SLS material.*

The properties of parts produced by AM processes are also strongly affected by sintering process parameters such as the laser beam power, the spot size, the scanning speed, the preheat temperature (Williams and Deckard, 1998)(Bertrand *et al.*, 2007)

However, significant impact on the properties of the manufactured objects as well as on the spreading performance and on the packing ability is given by the powder properties such as the morphology, the particle size distribution (Averardi *et al.*, 2020), and the purity of powders.

Normally, spherical and smooth particles with a defined size distribution are used because of a better spreadability and a denser packing of the deposited layer. In fact, the more spherical is the particle shape the less the internal

friction in the powder (Berretta *et al.*, 2014). This allows for easier deposition of powder and higher layer density (Strondl *et al.*, 2015).

Sun et al. (Sun *et al.*, 2015) used a shape factor to study the effect of changes in the morphology of particles after repeated reuse of a titanium powder in an AM process, that is the electron beam melting. Results showed that the average circularity of the powder reduced because of formation of agglomerates after successive build iterations. As a result, interparticle friction increased and the flowability of the recycled powder decreased. Virgin powder provided more uniform layers compared to the recycled powder. Hence, powder-bed based AM processes can be very sensitive to irregularly shaped particle. Therefore, particles with high spherical shape, smoothness and dry surface are desired as these characteristics are known to provide the least amount of interparticle friction and consequently the best flowability.

However, because of the requirements of spherical morphology, defined particle size ranges and chemical purity, AM powders in the current market are mainly produced by high operating cost processes. In fact, production of micron-sized plastic or visco-elastic particles, like those used in SLS, are costly and energy-intensive process. For example low temperature processes like cryogenic milling (Wilczek, Bertling and Hintemann, 2004), cutting mills, rotor impact mills and jet mills are used for particle comminution. Subsequently, rounding processes are applied to the edged polymer particles obtained with the comminution process. In some cases, coating with nanoparticles to reduce interparticle cohesive forces, is used (Schmidt *et al.*, 2014; Ruggi, Lupo, *et al.*, 2020).

Moreover, some AM equipment sellers make available their own proprietary set of powders for their specific machines. As a result, the costs of powders and finished objects are high for most AM processes and applications (Sun *et al.*, 2015)

I.1.6 Knowledge gap

All the methods, which have been reported in paragraph I.1.3, try to predict whether a powder has sufficient flowability for the SLS process or not. However, all of them are indirect and do not necessarily provide truthful information on powder spreadability. In fact, during the spreading process, it is likely that powders experience a state of stress which can be different compared to that occurring during the tests with indirect instruments such as the Revolution Powder Analyzer or the ring shear cell. To verify whether a powder is suitable for the SLS process, it is necessary to use a direct method, namely to verify directly the spreadability of powders in conditions as similar as possible to those occurring during the spreading with a tool such as a blade or a roller.

In paragraph I.1.4, some examples of direct methods have been reported.

However, based on the literary review, there is no experimental setup by which it is possible to test powders by easily changing a large number of spreading conditions such as: 1) type of spreading tool; 2) scrolling velocity of the spreading tool; 3) rotational velocity of the roller; 4) direction of rotation of the roller; 5) inclination of the blade with respect to the spreading direction; 6) angle of the blade's tip; 7) thickness of the deposited powder layer, which has to change according to the average particle size.

Moreover, although majority of the methods presented in the scientific literature provide qualitative information about the quality of the deposited powder layer such as the existence of local empty patches (Ahmed *et al.*, 2020); the particle-scale powder dynamics during the powder spreading process (Escano *et al.*, 2018); macroscopic observation of the layer surface (Van den Eynde, Verbelen and Van Puyvelde, 2015), they lack the quantitative information on the surface asperities, e.g. the size of the asperities. Therefore, new, alternative and more accurate methods of characterisation of quality of the powder layer from a qualitative as well as quantitative point of view are necessary to properly choose the spreading configuration for a given powder or, in principle, to specifically engineer the powder for a specific spreading configuration.

Chapter II
Discrete Element Method

II.1 Introduction

Discrete element method (DEM) is a computational method by which granular flow at an individual particle level is analyzed. DEM is used in many fields, such as mining, agriculture, geotechnical, mixing and milling applications, in order to design, study and optimise equipments or handle systems for loose granular materials (Coetzee, 2017). All these applications can include interparticle cohesive forces (Obermayr *et al.*, 2014), which can be caused by: the formation of liquid bridges among the particles (Xu *et al.*, 2017), van der Waals and electrostatic forces (Chirone *et al.*, 2018).

This method has been also used for the AM processes to investigate different properties of the deposited powder layer such as the packing density (Haeri *et al.*, 2017) or the superficial roughness (Parteli and Pöschel, 2016) and powder behaviour during spreading (Fouda and Bayly, 2020) with changes of parameters such as the particle size (Xiang *et al.*, 2016), the spreader velocity (Chen *et al.*, 2017b) and the gap height (Nan *et al.*, 2018; Nan, Pasha and Ghadiri, 2020).

There are two main approaches that can be followed in DEM: the *hard-sphere* approach and the *soft-sphere* approach (Di Renzo and Di Maio, 2004). In the first case, proposed by Alder and Wainwright (Alder and Wainwright, 1957), particles are considered to be rigid and single binary collisions are modelled as instantaneous processes and the properties of the particles after the collision are related to the properties of the particles before the collision through momentum and energy balances. Energy is dissipated during collisions due to surface friction and coefficients of restitution.

However, the binary collision concept limits the application of this method to systems where multiple and simultaneous collisions are unlikely to occur, e.g. to dilute systems. In fact, simulations of rigid spheres are "event driven" in that the time step used to advance the simulation is the time between

subsequent collisions. This time changes during a simulation and, in case of simultaneous or continuous contacts, the time step goes to zero and the hard sphere approach is no longer applicable.

On the contrary, the soft-sphere approach, originated with the work of Cundall (Cundall, 1971), and defined as the Distinct Element Method, today known as Discrete Element Method, allows to deal with multi-particle collisions and the inter-particle forces can be easily implemented, even if with higher computational time. In fact, the evolutions of forces, velocities and displacements are simulated during the collision, and the contact is modelled as a mechanical system such as a linear spring–dashpot model or a more complex non-linear system.

In the soft sphere approach, the particles are modelled as discrete entities and their motions and trajectories are described by the translational and rotational motion, given by the Newton's second law:

$$m_i \frac{dv_i}{dt} = \sum_j F_{ij}^c + \sum_k F_{ik}^{nc} + F_i^f + m_i g \tag{3}$$

$$\frac{d\omega_i}{dt} = \frac{\sum_j F_{ij}^t R}{I_i} \tag{4}$$

where m_i, v_i and ω_i are the mass, translational velocity and angular velocity of particle i , respectively; t is the time, F_{ij}^c is the contact force due to interaction between the particle i and the nearby ones j or the wall; F_{ik}^{nc} represents the non-contact forces like van der Waals and electrostatic forces acting on particle i by particle k or the other possible forces; F_i^f is the particle-fluid interaction force; $F_{ij}^t R$ is the torque imposed on particle i by particle j, I_i is the moment of inertia and g is the acceleration due to the gravity. By integrating (3) and (4), new velocities and positions of the particles are obtained (Cundall and Strack, 1979; Thornton, 2015).

In this approach, a contact force model is used to account for particle–particle interaction, based on the deformation represented by overlap of colliding particles (Buist *et al.*, 2016).

In the original paper, Cundall and Strack (Cundall and Strack, 1979) considered particles as connected by linear springs in the normal and tangential directions. The corresponding normal and tangential contact forces were calculated incrementally as the product of the spring stiffnesses and the relative surface displacement increments of the two contacting particles. However, a number of contact force models can be used.

Most of the modelling cases being carried out nowadays use the soft-sphere approach due to its higher capability and accuracy.

II.2   Contact force models

To start a DEM simulation, a contact model must be implemented with the corresponding input parameters. A contact model describes how elements behave when they come into contact with each other, i.e. describes the forces deriving from particle collisions and contacts. As a result, particle interactions are considered in the calculations. There exist a number of force models which mostly allow particles to have deformation, modelled as an overlap between them. Among the most used contact models are: the Hertz-Mindlin (no slip), the Hertz Mindlin with JKR (Johnson-Kendall-Roberts) cohesive model (Baran *et al.*, 2009), the Linear Cohesion (Romaní Fernández and Nirschl, 2013).

The Hertz-Mindlin (no slip) is the default model used in the EDEM software (provided by DEM solutions Ltd, Edinburgh, UK) due to its accurate and efficient force calculation. It accounts for the effects of contact of two elastic spheres. In this model: the normal force component is based on Hertzian contact theory (Hertz, 1881), the tangential force model is based on Mindlin-Deresiewicz work (Mindlin, 1989; Mindlin and Deresiewicz, 1989). Both normal and tangential forces have damping components (Tsuji, Tanaka and Ishida 1992).

Hertz-Mindlin (no slip) with JKR cohesive model is a cohesion contact model that accounts also for the influence of van der Waals forces within the contact zone and allows the user to model strongly adhesive systems, e.g. dry powders or wet materials.

The Linear Cohesion model modifies a certain base contact model (e.g. the Hertz Mindlin) by adding a normal cohesion force.

II.2.1   Hertz-Mindlin model

The Hertz-Mindlin model merges the Hertz normal contact model, which is based on the normal force between two perfectly spherical objects in contact, and the Mindlin tangential contact model, which considers the tangential force at the interface of the particles because of the friction.

The assumptions behind the Hertz model are the following (Dintwa, Tijskens and Ramon, 2008):

1)   the contacting bodies are isotropic and homogeneous;
2)   the loads applied are static;
3)   the area of contact between the two objects is circular and it is subjected to surface tractions or pressures, while zero tractions and displacements are present elsewhere on their surface;
4)   the area of contact between the two objects is much smaller than the size of the objects in contact, i.e. the radii of curvature of the contacting bodies are much larger than the contact radius. This

assumption ensures that the stresses that arise due to the contact vanish at the opposite end of the body;

5) the deformation of the objects is elastic and very small. Hence geometric nonlinearities that arise due to large deformations are not taken into account. The constitutive law for the material behaviour is then considered to be the Hooke's law;

6) the contacting surfaces are smooth. Therefore, no friction effects at the contact surfaces are considered and the normal contact force is the only one;

However, the contacting objects have friction and therefore a tangential force should be considered at the interface. Mindlin (Mindlin, 1989) showed that may be either sticking or slipping between the points in the contact area. The stick region is at the center of the contact area and it is characterized by no relative motion between adjacent points of the two objects. At the slip region, the objects have a relative velocity at the point of contact. According the Hertz–Mindlin collision model, the elastic repulsive force (F_n^{el}) between two perfectly elastic spherical objects in contact is a function of normal overlap between two particles (α_O) and is given by (Bortolotti *et al.*, 2013):

$$F_n^{el} = \frac{4}{3} \, E^* \, \sqrt{R^*} \, \alpha_O^{\,3/2} \tag{5}$$

with:

$$\frac{1}{E^*} = \frac{1 - \nu_i^2}{E_i} + \frac{1 - \nu_j^2}{E_j} \tag{6}$$

and

$$\frac{1}{R^*} = \frac{1}{R_i} + \frac{1}{R_j} \tag{7}$$

where E^* and R^* are the equivalent Young's Modulus and the equivalent radius, respectively; E_i, ν_i, R_i, and E_j, ν_j, R_j, are the Young's Modulus, the Poisson ratio and the radius of each sphere in contact, respectively.

II.2.2 Hertz-Mindlin (no slip) model in the EDEM software

The Hertz-Mindlin (no slip) model is a viscoelastic model, that is the contact force between two colliding bodies includes two parts, one for the elastic repulsion, modelled by a spring, and the other for the viscous dissipation, modelled by a dashpot (Ji and Shen, 2006). No slip means that there are not regions in the contact area where the shear stress exceeds the

Coulomb's limit (Courtney Pratt and Eisner, 1957). Therefore, no small local tangential displacement occurs at the contact area.

The energy dissipation due to the contact is considered by means of viscous damping terms for both normal and tangential forces (Hesse, Krull and Antonyuk, 2021). The viscous damping coefficient is related to the coefficient of restitution according to the model of Tsuji et al. (Tsuji, Tanaka and Ishida, 1992). The tangential friction force follows the Coulomb law of friction model (Cundall and Strack, 1979). The rolling friction is implemented as the contact independent directional constant torque model (Sakaguchi, Ozaki and Igarashi, 1993).

The normal force, F_n, experienced by a particle during impact is given by the sum of two components: the elastic repulsive force, F_n^{el}, based on Hertz contact theory and the viscous damping force, F_n^d (Alizadeh, Bertrand and Chaouki, 2013).

The normal viscous damping force, F_n^d, is given by:

$$F_n^d = -2\sqrt{5/6}\,\beta\,\sqrt{S_n m^*}\,\overrightarrow{v_n^{rel}} \tag{8}$$

where:

$$m^* = \left(\frac{1}{m_i} + \frac{1}{m_j}\right)^{-1} \tag{9}$$

is the equivalent mass, where m_i and m_j are the masses of the two objects in contact, $\overrightarrow{v_n^{rel}}$ is the normal component of the relative velocity, and β (damping parameter) and S_n (normal stiffness) are given by:

$$\beta = \frac{\ln e}{\sqrt{\ln^2 e + \pi^2}} \tag{10}$$

$$S_n = 2\,E^*\sqrt{R^*\alpha_O} \tag{11}$$

where e is the coefficient of restitution, which describes the ratio between rebound and impact velocity and it is related to the loss of kinetic energy (E_{kin}) after a collision (Hesse, Krull and Antonyuk, 2021). Therefore:

$$e = \frac{|v_{rebound}|}{|v_{impact}|} = \sqrt{\frac{E_{kin,rebound}}{E_{kin,impact}}} \tag{12}$$

The tangential force (F_t) includes two terms: the tangential elastic force (F_t^{el}), according to the Mindlin's no-slip tangential contact model without the micro slip at the contact area (Mindlin, 1949), and the tangential damping

force (F_t^d). The first one depends on the tangential overlap (α_t) and the tangential stiffness (S_t):

$$F_t^{el} = -S_t \alpha_t \tag{13}$$

where:

$$S_t = 8\, G^* \sqrt{R^* \alpha_O} \tag{14}$$

G^* is the equivalent shear modulus. It is defined as follows:

$$\frac{1}{G^*} = \frac{2 - v_i^2}{G_i} + \frac{2 - v_j^2}{G_j} \tag{15}$$

where G_i and G_j are the shear modulus of each sphere in contact.

Tangential damping is given by:

$$F_t^d = -2\sqrt{5/6}\, \beta \sqrt{S_t m^*}\, \overrightarrow{v_t^{rel}} \tag{16}$$

where $\overrightarrow{v_t^{rel}}$ is the relative tangential velocity. The tangential force is limited by Coulomb friction $\mu_S F_n$ where μ_S is the coefficient of static or sliding friction, that is (Di Renzo and Paolo Di Maio, 2005):

$$|F_t| \leq \mu_S |F_n| \tag{17}$$

For simulations in which rolling friction is important, this is accounted for by applying a torque to the contacting surfaces (T_i), according to the model of Zhou et al. (Zhou *et al.*, 1999):

$$T_i = -\mu_R\, F_n^{el}\, R_i\, \widehat{\omega_i} \tag{18}$$

with μ_R the coefficient of rolling friction, R_i the distance of the contact point from the center of mass and $\widehat{\omega_i}$, the unit angular velocity vector of the object at the contact point (Ai *et al.*, 2011).

II.2.3 Johnson Kendall Roberts (JKR) model

According to the JKR theory (Johnson, Kendall and Roberts, 1971), when a spherical particle is pressed against another particle, the stresses between the surfaces into contact are tensile (T) at the edge of the contact area and compressive (P) in the center (see curve B in Figure II.1). In the absence of the adhesive forces, the deformed profile (Figure II.2) of each sphere immediately outside the contact area would correspond to the broken line of Figure II.2, namely would meet the interface tangentially. However, when

there are adhesive forces, the profile corresponds to the full line of Figure II.2, which meets the interface perpendicularly.
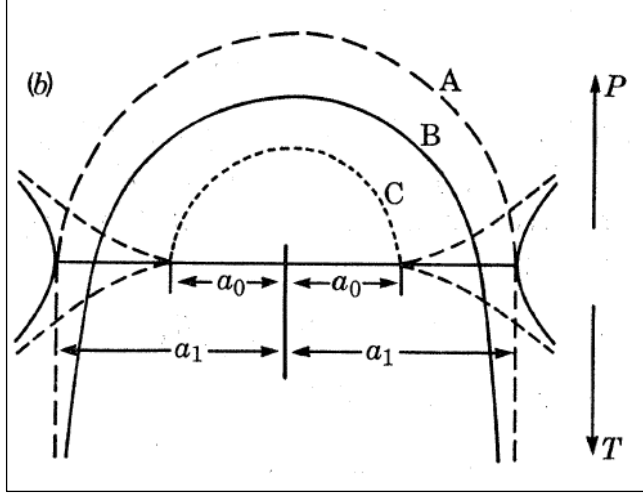
Figure II.1 *Distribution of stress in correspondence of the contacting spherical surfaces. Distribution A is the Hertz stress with $a = a_1$ and $P = P_1$; distribution B is the actual stress according the JKR model with $a = a_1$ and $P = P_0$; distribution C is the Hertz stress with $a = a_0$ and $P = P_0$. P is the compressive stress while T is the tensile stress* (Johnson, Kendall and Roberts, 1971).
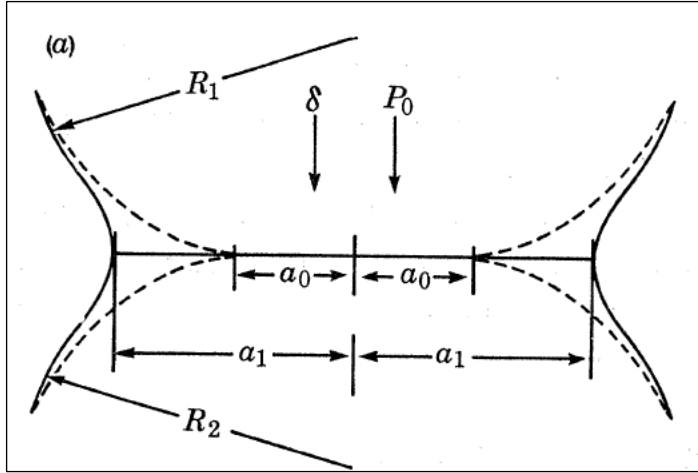
Figure II.2 *The contact between two elastic convex bodies of radii R_1 and R_2 under a normal load of P_0, both in presence (contact radius a_1) and*

absence (contact radius a_0) of surface forces; δ is the elastic displacement (Johnson, Kendall and Roberts, 1971).

According to the JKR theory (Johnson, Kendall and Roberts, 1971), the normal elastic contact force depends on the overlap α_O and the interaction parameter, i.e. the Interfacial Surface Energy (or work of adhesion) Γ in the following way:

$$F_{JKR} = -4\sqrt{\pi\Gamma E^*}\, a^{3/2} + \frac{4\,E^*}{3\,R^*}\, a^3 \tag{19}$$

where the overlap is defined as follows:

$$\alpha_O = \frac{a^2}{R^*} - \sqrt{\frac{4\pi\Gamma a}{E^*}} \tag{20}$$

where a is the contact radius and:

$$\Gamma = \gamma_1 + \gamma_2 - \gamma_{1,2} \tag{21}$$

where γ_1 and γ_2 are the surface free energies of the two spheres and $\gamma_{1,2}$ is the interface surface energy. For the special case where two spheres of the same material come into contact the interface surface energy is zero ($\gamma_{1,2} = 0$), thus the interfacial surface energy becomes $\Gamma = 2\,\gamma$ where $\gamma_1 = \gamma_2 = \gamma$. Work of adhesion is the work required to separate two surfaces of unit area from contact to infinity (Seville, Tüzün and Clift, 1997).

For $\Gamma = 0$, F_{JKR} turns into Hertz-Mindlin normal force.

The maximum tensile force required to break the contact between two particles is the pull-out force, which is given by:

$$F_{pullout} = -\frac{3}{2}\, \pi\Gamma R^* = F_{nc} \tag{22}$$

It depends on the radius of the particles and on Γ. Johnson et al. (Johnson, Kendall and Roberts, 1971) were able to confirm these results by experiment using optically-smooth rubber spheres.

Johnson (Thornton, 2015) provided the following relationship between the normal contact force F_n and the relative approach or overlap α_O, which is shown in Figure II.3:

$$\frac{\alpha_O}{\alpha_{O,f}} = \frac{3\left(\frac{F_n}{F_{nc}}\right) + 2 + 2\left(1 + \frac{F_n}{F_{nc}}\right)^{1/2}}{3^{2/3}\left[\frac{F_n}{F_{nc}} + 2 + 2\left(1 + \frac{F_n}{F_{nc}}\right)^{1/2}\right]^{2/3}} \tag{23}$$

where:

$$\alpha_{O,f} = \left(\frac{3\,F_{nc}^2}{16\,R^*E^{*2}}\right)^{1/3} \tag{24}$$

is the relative approach (negative) at which the contact breaks, point D in Figure II.3.

When the surfaces of the two spheres, which represent the particles, come into contact (Thornton, 2015) the normal force between the two spheres (F_n) decreases to a value of $F_n = \left(-\frac{8}{9}F_{nc}\right)$ (point A in Figure II.3) due to van der Waals attractive forces. When the two spheres are compressed, the contact force increases and reaches a maximum (point B in Figure II.3). When they are decompressed (unloading stage) until α_O is equal to 0, the work done during the loading stage is recovered in correspondence of the point A. At this point, the contact area is not zero, the spheres remain adhered together, and further work is required to break the contact and create "new" surface area. The point in which the situation becomes unstable and the contact breaks is point C (Figure II.3), when $F_n = -F_{nc}$, $\alpha_O = \alpha_{O,f}/3^{2/3}$. However, particle system simulations are always displacement driven, thereby separation occurs at point D (Figure II.3) when $\alpha_O = -\alpha_{O,f}$ and $F_n = \left(-\frac{5}{9}F_{nc}\right)$.
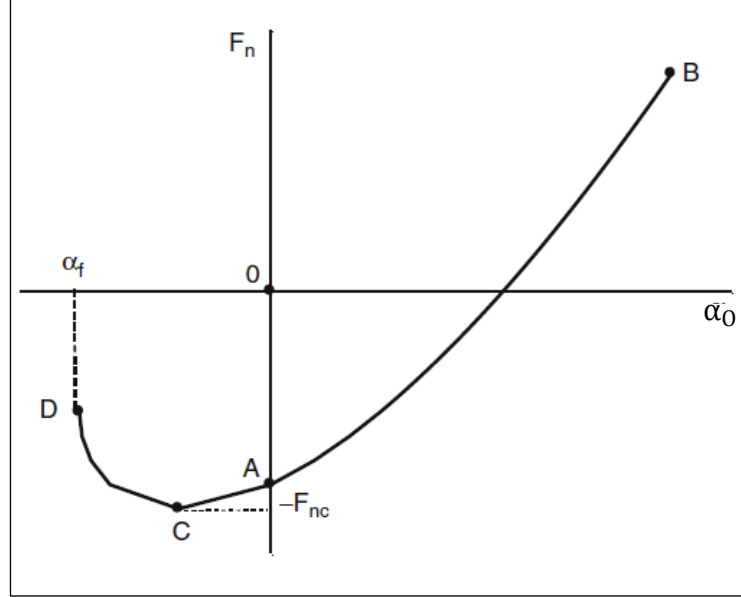
Figure II.3 *Normal force (F$_n$)-overlap curve (JKR theory)* (Thornton, 2015).

In the Hertz-Mindlin (no slip) with JKR (Johnson-Kendall-Roberts) cohesive model of the EDEM software, the normal elastic contact force is calculated according to eq. (19), while the normal dissipation force, tangential elastic force and the tangential dissipation force are calculated according to the Hertz-Mindlin (no slip) contact model.

II.3   Calibration of DEM parameters: state of the art

There are two approaches reported in the literature to calibrate the DEM input parameters: the Direct Measuring Approach and the Bulk Calibration Approach (Coetzee, 2017).

The *Direct Measuring Approach* consists of determining the property value by directly measuring it.

For example, Nan et al. (Nan *et al.*, 2018; Nan and Ghadiri, 2019) in order to simulate the powder flow during spreading in additive manufacturing used the interfacial adhesive surface energy of the JKR model, measured by the drop test method (Zafar *et al.*, 2014).

Surface energy can be calculated also from contact angle measurements using the Owens-Wendt-Rabel-Kaelble method or from the atomic force microscopy measurements (Üzüm, 2015).

Even if it is not always feasible, other DEM parameters can be calculated experimentally, such as: the coefficient of static friction (L. Wang *et al.*, 2018;

Nan *et al.*, 2018), the coefficient of rolling friction and the coefficient of restitution (Teffo and Naudé, 2013; Wang *et al.*, 2015; Nan *et al.*, 2018).

The direct measuring approach allows a deeper insight in the contact physics but requires complex experimental device able to operate at the particle level, therefore the *Bulk Calibration Approach* is often followed, which consists in the measurement of a material bulk property in experiments which are then numerically replicated. The most appropriate DEM parameter value is found by changing its value in replicated simulation, until the experimental bulk property matches the experimental value.

For example, Lupo et al. (Lupo *et al.*, 2019) used this approach to try and evaluate the interfacial adhesive surface energy between the particles and the cohesion energy density from the comparison between the experimental and the measured interparticle cohesive force by using the Hertz-Mindlin (no slip) with the JKR model or with the Linear cohesion model, respectively. In that case it was demonstrated that the choice of time step in the simulation can lead to very different values of the evaluated contact force.

Salehi et al. (Salehi *et al.*, 2018) used the Anton Paar powder cell to calibrate the coefficient of sliding friction between the particles by comparing the experimental torque, obtained with the two-blade impellers, and the DEM simulation. They also determined the coefficient of sliding friction between the particles and the geometry by matching experiments and simulation predictions in the case of a circular impeller.

Grima et al. (Grima and Wypych, 2011) calibrated the coefficients of static and rolling friction and the coefficient of restitution by measuring the angle of repose, comparing it with the one obtained with the simulation, and by validating the DEM models by comparison of the results of the simulations against experimental slump tests and hopper discharge experiments.

Alizadeh et al. (Alizadeh *et al.*, 2018) used the angle of repose as a way to tune the surface energy and they observed a good agreement between the experimental and DEM simulation results.

Roessler et al. (Roessler and Katterfeld, 2019) calibrated the coefficient of sliding friction, the coefficient of rolling friction, and cohesion energy density of a simplified JKR model by simulating the pull-up test of a hollow cylinder filled with bulk material.

Karkala et al. (Karkala *et al.*, 2019) simulated both the dynamic yield strength test and shear-cell experiment to calibrate the following DEM parameters: surface energy, coefficients of sliding and rolling friction.

Coetzee (Coetzee, 2020) calibrated the contact stiffness using a confined compression test, and the coefficients of sliding and rolling friction by using either the individual or combined results from a draw down, a rotating drum and an annular ring shear test.

Chen et al. (Chen *et al.*, 2017b) evaluated the coefficient of sliding friction and the interfacial adhesive surface energy between the particles by comparing

the macroscopic flow profile of the powder during layering between the numerical and experimental results.

Angus et al. (Angus *et al.*, 2020) combined sliding test experiments and DEM simulations of both homogeneous simple shear and the FT4 shear cell to evaluate the coefficients of rolling and sliding friction. They figured out that one single simulation type could not be sufficient to calibrate the DEM parameters. In fact, homogeneous simple shear simulations returned multiple pairs of both the coefficients. Simulations of the full FT4 shear cell with different pairs obtained with the previous simulation procedure were necessary to find the correct pair.

II.4   Methods of analysis of quality of simulated powder layer:

state of the art and knowledge gap

Discrete element model has become the main tool to computationally study the particle scale spreading process and understand the physics of powder behaviour, which is not fully understood merely on the basis of experiments. In literature, the effects of the spreading speed, spreader type or powder size distribution on the surface roughness and compaction of the powder bed have been analysed by using DEM.

For example, Parteli et al. (Parteli and Pöschel, 2016) used a DEM model to investigate the powder spreading using a roller as a coating system, which rotates counter clockwise. Two different scrolling velocities were used, namely 20 and 180 mm s^{-1}, at a rotational velocity of 165 rpm.

Results of simulations showed that the bed roughness increases monotonously with the scrolling speed. Moreover, they also found that a strong polydispersity may lead to larger surface roughness due to the tendency of very small particles to form large agglomerates due to the strong attractive particle interactions. Therefore, as the roller moves to spread the powder, the surface roughness of the formed layer is largely affected by the shape and size characteristics of the particle agglomerates, and thus by the particle size distribution. The other important result of the simulations is that the load, exerted by the roller on the sintered part below the layer, may vary an order of magnitude during the coating process owing to the strong inhomogeneity of interparticle forces in the powder below the roller during spreading. Force chains are formed in the powder and particles in the zones between these chains are shielded and thus are subjected to lower stress. Because of the dynamics of force chains in the powder, there are strong spatial and temporal fluctuations in the forces exerted by the powder on the coating system and the part below that is being built. Dynamics of force chains in granular materials may be influenced by the material properties, such as the Hamaker constant and friction coefficient in addition to the Young's modulus. This result may confirm the well-known result by which the lack of flowability and high

porosity of powder systems is not only influenced by particle shape but also and mainly by the interparticle cohesive forces (Liang Deng and Davé, 2013).

This work demonstrates that a correct DEM model can be used to assist and partially replace experimental investigations of the flowability and packing behaviour of different powders as a function of material and process parameters.

Chen et al. (Chen *et al.*, 2017b) proposed a numerical model, based on DEM, to investigate quantitatively at particle scale the spreadabilty of powder layered by a blade and to make understanding about the forming mechanism of the powder bed in SLM manufacturing. The simulated powder is composed of spherical particles to represent the 316L stainless steel powder, and the spreading tool is a blade. The DEM model was validated by comparing the profiles of the powder heap during layering at different positions along the spreading direction in both the experimental tests and the simulations, using image processing method.

Dynamic repose angle (DRA), that is the average repose angle during layering, and mass flow rate (MFR) of the powder, that is the mass of particles in the gap between the blade and the sintered part in unit time, were defined to characterize quantitatively the flowing behaviour of the powder, which affects the packing density and uniformity of the powder bed.

The effects of material properties of particles, interparticle cohesive forces, and processing parameters of layering apparatus on the powder spreadability were investigated.

Results showed that the powder flowability, represented by DRA, increases as the coefficients of sliding and rolling friction between the particles decrease, resulting in a denser and more uniform powder bed. In fact, MFR increases and the variation coefficient, which represents the stability of the particle flow below the blade, decreases as the coefficients decrease.

For particle radius (R) > 21.8 μm, if R decreases the flowability improves, as demonstrated by the increase of DRA, the decrease of MFR and the increase of the variation coefficient, while for R< 21.8 μm, flowability gets worse as R decreases, due to increase of Bond (Bo) number, i.e. the ratio between the interparticle cohesive force and the particle weight. As a consequence, the powder flowability and the quality of layered powder bed get worse.

The increase of blade velocity enhances the dilation of moving particles, and the decrease of layering height intensifies the local force-arches in particles. As a result, the continuity and stability of the powder flow are reduced. These conditions are unfavourable for improving the density or uniformity of the layered powder bed. Results about the effect of layering height on spreadability confirm what Nan et al. (Nan *et al.*, 2018) have demonstrated by means of numerical simulations.

Haeri et al. (Haeri *et al.*, 2017) simulated spreading of rod-shaped particles in typical AM configurations using DEM to investigate the effects of particle

shape and operating conditions on the bed quality, in terms of its surface roughness and solid volume fraction.

Results showed that larger particle aspect ratios (AR) or higher spreader translational velocities result in a lower bed quality, i.e. a larger surface roughness and a smaller volume fraction.

The surface roughness resulted to increase monotonically with AR.

However, the volume fraction has a maximum in case a roller is used at low translational velocities, while it always decreases in case of the blade, for all the analysed velocities. Haeri et al. also found that a roller outperforms a blade in terms of the quality of the prepared bed at the same operating conditions. This latter result confirms what was experimentally proved by Van der Schueren at al. (Schueren and Kruth, 1995) and reported in paragraph I.1.2.

Haeri et al. (Haeri, 2017) also used DEM simulations to study the effect of different blade profiles and of the spreader velocity on quality of the powder layer, quantified in terms of powder bed void fraction. The results have been explained in paragraph I.1.2.

Yee (Yee, 2018) created a discrete element model simulating the powder spreading of by using the software LIGHTSS to compare the model results with the experimental ones, reported in paragraph I.1.4.

When the experimental results were compared to the results from the simulation, they did not completely agree. In fact, different regions with the smoothest surface quality were obtained between the experiments and the simulations. However, also the simulation showed increasing roughness in the direction of spreading.

Looking at PSD, the experiments showed little difference in the distribution between the 9 regions and the dosage rates, but in the simulation, the distribution of finer particles was higher at the beginning of the spread and in the final part of the layer. Decreasing the speed and increasing the dosage rate increased the number of finer particles present on the build area.

Nan et al (Nan *et al.*, 2018) analysed transient jamming of gas-atomised metal powders during spreading. Jamming is due to mechanical arching and it is influenced by powder properties and process conditions. Numerical simulations of powder spreading by the Discrete Element Method was carried out to investigate jamming of frictional particles in narrow gaps.

D_{90} by number was used as the particle dimension accountable for jamming.

Jamming is shown through empty patches along the spread layer. Frequency and period of jamming have been analysed and reported as function of the gap height, that is the distance between the blade and the deposition plate. Gap heights have been fixed as a multiple of D_{90}.

Main conclusions emerged from this study were:

1) the probability of formation of empty patches and their mean length, which indicates jamming duration, increase with the decrease of the gap height;

2) the collapse of the arches leads to particle bursts after the blade, which contributes to the formation of empty patches;

3) as the survival time increases, the frequency of jamming for a given survival time decreases exponentially.

These predictions by numerical simulations are consistent with the experimental results obtained experimentally for the same gap heights and powder analysed in the work of Ahmed et al. (Ahmed *et al.*, 2020) and reported in paragraph I.1.4, but at higher blade velocity.

Ng (Ng, 2020) created a DEM model in Abaqus to simulate the spreading behaviour of particles through a single sweep of a spreader blade at a speed of 10 mm s^{-1}. Powder behaviour during spreading was investigated for three different build plate configurations, on which the artefact is built. These configurations differ for the geometry of the build plate, namely smooth or with protruding features, which simulate a part that has been improperly built in the previous layer and results in a raised defect encountered by the powders spread on top. For each configuration, the packing behaviour of the powder during the spreading process was analysed, looking at 2D images of the layer from above. The packing patterns observed in the simulated layer was analysed to determine particle packing density and to predict 3D packing behaviour. Packing density was used to quantify the quality of the spreading.

Results showed that the local packing fraction changes when particles interact with the build plate features.

He et al. (He *et al.*, 2020) proposed a digital-based approach for the characterisation of a spread powder layer. They evaluated both from a qualitative and quantitative point of view the quality of the powder layer. Qualitatively, contour maps were used. Quantitatively, packing density, surface profile and pore characteristics were measured by means of spatial discretisation of the working space. In particular, two different types of pores were used for the first time: the density pore*,* which can identify the less populated areas in the spread powder bed by thresholding the contour map of local packing density; the chamber pore, which is able to quantify the size of empty patches observed in the deposited powder bed. Applicability of this approach was demonstrated by analysing the powder layer obtained both from simulation and from experiment. This digital-based characterisation method is general and can be applied to both polydisperse and non-spherical particle systems.

Fouda et al. (Fouda and Bayly, 2020) used DEM simulations to study the spreading of spherical, mono-sized, non-cohesive titanium alloy particles with a blade to form a thin powder layer in AM applications. They investigated the reasons for which there is a reduction of packing density in the powder layer after deposition compared to the initial powder heap before the spreading. The

results showed that the deposited powder layer has a lower packing fraction due to three mechanisms: 1) shear-induced dilation, namely decrease of the packing fraction, of particles during the initiation of powder motion by the spreader; 2) dilation and rearrangement of particles due to powder motion through the gap between the blade and the deposition plate; 3) movement of particles at the back of the blade after they get detached from the main powder heap due to their inertia. It was shown that varying either the gap thickness or the spreader velocity can control the final packing fraction because one or more of these three mechanisms are suppressed or promoted. In particular, the final layer packing fraction increases with the gap thickness and decreases with the spreader velocity. The velocity profile, which is generated in the gap, affects the final layer packing fraction.

Lee et al. (Lee *et al.*, 2020) proposed a computationally efficient multi-layer powder spreading DEM simulation model. The model was calibrated experimentally using static angle of repose measurements. DEM simulations were used to analyse the effect of particle spreading dynamics on powder bed quality. The results of the simulations showed that the scrolling velocity of the blade has important effects on packing density, surface roughness, dynamic angle of repose and particle segregation.

Marchais at al. (Marchais *et al.*, 2021) studied the effect of powder properties, such as the friction coefficient and the surface energy, and of process parameters, such as the scrolling velocity of the blade, on the quality of the deposited layer, measured in terms of packing fraction, coordination number and average grain size. For this purpose, simulations based on DEM were carried out. The numerical model considered different interactions such as repulsion, dissipation, friction and adhesion that occur when two bodies come into contact. The surface roughness of the plate and of the spreader were considered in the simulations due to its significant impact on the powder bed spreading. The results showed that: 1) different friction values do not provide different results on the final properties of the powder bed; 2) adhesion has an important effect on the powder bed properties; 3) lower spreading speed determines better powder bed; 4) powder bed is denser with a higher surface roughness of the deposition plate and of the blade.

He at al. (He, Hassanpour and Bayly, 2021) used particle-scale simulations to study the combined effect of particle size and surface cohesiveness on the spreading of cohesive fine powders. The DEM model, which was validated against literature data on static angle of repose formed by discharging Ti-6Al-4V powders from a vibrating funnel, revealed two competing mechanisms due to geometrical constraint and interparticle cohesion. Some of the main conclusions are: 1) in case of small particles, layer homogeneity is largely maintained before deteriorating sharply; 2) in case of large particles, which form a mono-layered packing structure, an optimum homogeneity can be obtained at a moderate level of particle cohesion; 3) surface roughness of the deposited layer reduces with decreasing particle size and a larger degree of

reduction is observed for particles with a smaller surface cohesiveness; 4) layer quality depends on two competing effects: the geometrical effect, due to the constraint of blade clearance, and cohesive effect, due to the Bo number and hence to the interparticle cohesion. In particular, the cohesive effect becomes predominant over the geometrical effect in case the Bo number is greater than 100.

All these works demonstrate that numerical simulations can be very useful to understand what happens at the particle level and could help to properly design the spreading system as well as to engineer suitable powders to improve the quality of layered powder bed in additive manufacturing such as the SLS process.

Although considerable efforts have been made to understand the factors affecting the homogeneity of the deposited powder layer by means of models, such as those previously described (Chen *et al.*, 2017b; Haeri *et al.*, 2017; Nan *et al.*, 2018; Fouda and Bayly, 2020), and experiments, such as those reported in paragraph I.1.4 (Escano *et al.*, 2018; Ahmed *et al.*, 2020), few systematic approaches have been reported in literature with the purpose of assessing the quality of the deposited powder layer in the AM processes from a quantitative point of view. In particular, to the best of my knowledge, very few methods of quantitative analysis of powder layer quality, which can be applied to both experiments and DEM simulations, have been proposed.

Chapter III
Experimental materials, apparatuses and procedures

III.1 Material

The polymeric powder used in the experiments and simulated with the DEM is the Domo's Sinterline unfilled polyamide 6 3400 HT110 Natural (PA6), purposely designed for the SLS process. The material properties derived from the literature (Polyamide 6 - Nylon 6 - PA 6) or from the technical data sheet of the powder (Domo | Product Finder) and used in the DEM are reported in Table III.1.

Table III.1 *Material properties of PA6 powder used in the simulation: D_{10}, D_{50} and D_{90} are the particle diameters corresponding to the 10th, 50th and 90th percentile of the cumulative particle size, respectively; $d_{3,2}$ is the Sauter mean diameter, $d_{4,3}$ is the the volume mean diameter, ρ_s is the density of the solid; ρ_b is the bulk density of the powder. Value with reference was taken from the literature, the other values were taken from the technical data sheet of the powder or, in case of $d_{3,2}$ and $d_{4,3}$, were measured with the Morphologi G3 (Malvern Panalytical Ltd., Malvern, UK). * These diameters are average values of the range values provided in data sheet of the powder*

Material	D_{10} (μm)	D_{50} (μm)	D_{90} (μm)	$d_{3,2}$ (μm)	$d_{4,3}$ (μm)	ρ_s (kg m^{-3})	ρ_b (kg m^{-3})
PA6	25*	55*	95*	43	55	1140 (Polyamide 6 - Nylon 6 - PA 6)	525

To characterise the shape distributions of the particles in order to properly replicate the powder with the DEM, SEM images were taken by using the TM3030Plus Tabletop SEM (Hitachi, JP). The images are reported in Figure III.1. They show that the particles differ from each other and have irregular shapes.
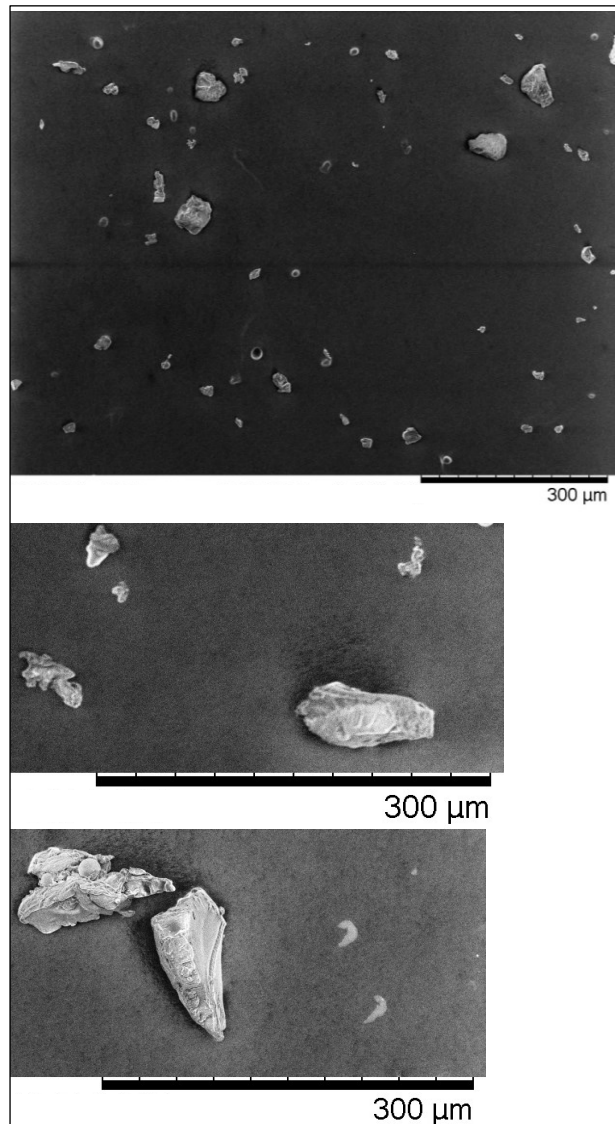
Figure III.1 *SEM images of Polyamide 6 (SINTERLINE®) particles.*

III.2 A new experimental setup

III.2.1 *From idea to implementation*

The analysis reported in Appendix A has shown that the compression of the powder layer could be a way to obtain denser powder layers even using powders which are not specifically engineered to be spread in the SLS process, such as those made of irregular shape or edged particles or without flowing enhancers. The analysis has highlighted that it is likely that compressible powders pass through the nip region alone, which may cause the powder dragging. Therefore, it is necessary to study the conditions, e.g. the rotational velocity of the roller as well as the roller geometry, by which the powder is compressed without being dragged away. Moreover, the smaller the angle of attack of the powder on the roller the smaller is the force of the roller on the layer. Since one should imagine that the roller exerts its pressure not only on the deposited layer but also on previously sintered layers, it should be important to reduce the roller force and consequently the shear stress of the roller on the layer which could cause the breakage of the object under construction. To study these issues and also to test new possible configurations of spreading, a new experimental setup was designed and built. The setup allows to use blades with different inclinations with respect to the deposition tray as well as different angles of the blade's tip. Different scrolling velocities of the blade can also be fixed. Moreover, the roller can be used as an alternative to the blade to compress the powder layer. Also in this case, different scrolling and rotational velocities of the roller can be tested as well as different diameters of the roller. To properly implement the Johanson's theory in the manner proposed in Appendix A.2 and to meet the needs come out from the analysis carried out on compressible powders, a new configuration is presented here. This configuration consists of a combination of the blade and the roller. In particular, the blade aims to deposit the powder and to set appropriate angle of attack of the powder on the roller. Once the layer is deposited, the powder comes into contact with the roller in correspondence of the angle set. Then the roller compresses the powder (Figure III.2).

A summary of the parameters that can be fixed to test the powders are reported in Table III.2.
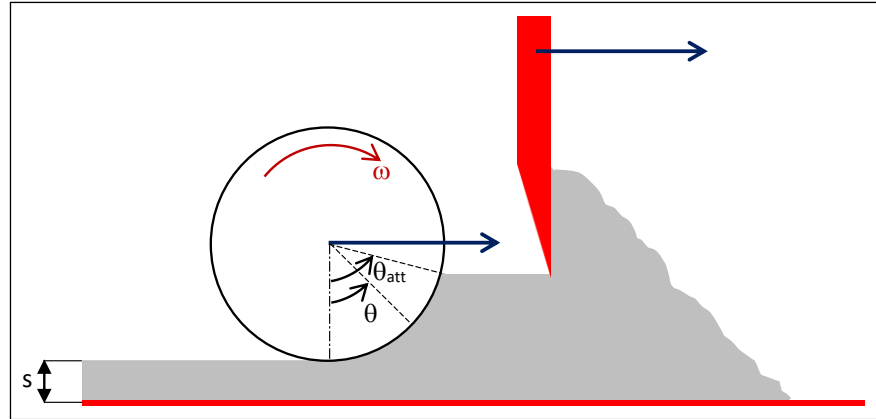
Figure III.2 *A new configuration for the spreading and compaction of the powder. The blade (red figure) is in front of the roller. The blue arrows indicate the advancement direction; s is the layer thickness and the roller rotates clockwise with a certain angular velocity (ω). θ is the angular position of the powder with respect to the roller and θ_{att} is the angle of attack of the powder on the roller.*

Table III.2 *Parameters of the setup that can be changed in the experimental tests. The tick indicates whether the corresponding parameter can be changed or not in case a blade and/or a roller is used.*

Parameter	Blade	Roller
Scrolling velocity	✓	✓
Rotational velocity		✓
Direction of rotation		✓
Inclination of the spreading tool	✓	
Angle of tip	✓	
Diameter		✓
Angle of attack of the powder on the roller	✓	
Depth of trays	✓	✓

III.2.1.1 Description of the setup

The supporting structure of the setup consists of a frame, made of 4 columns and 12 aluminium profiles (Figure III.3). Angles with dowels and hexagon socket head screws have been used to connect the profiles.
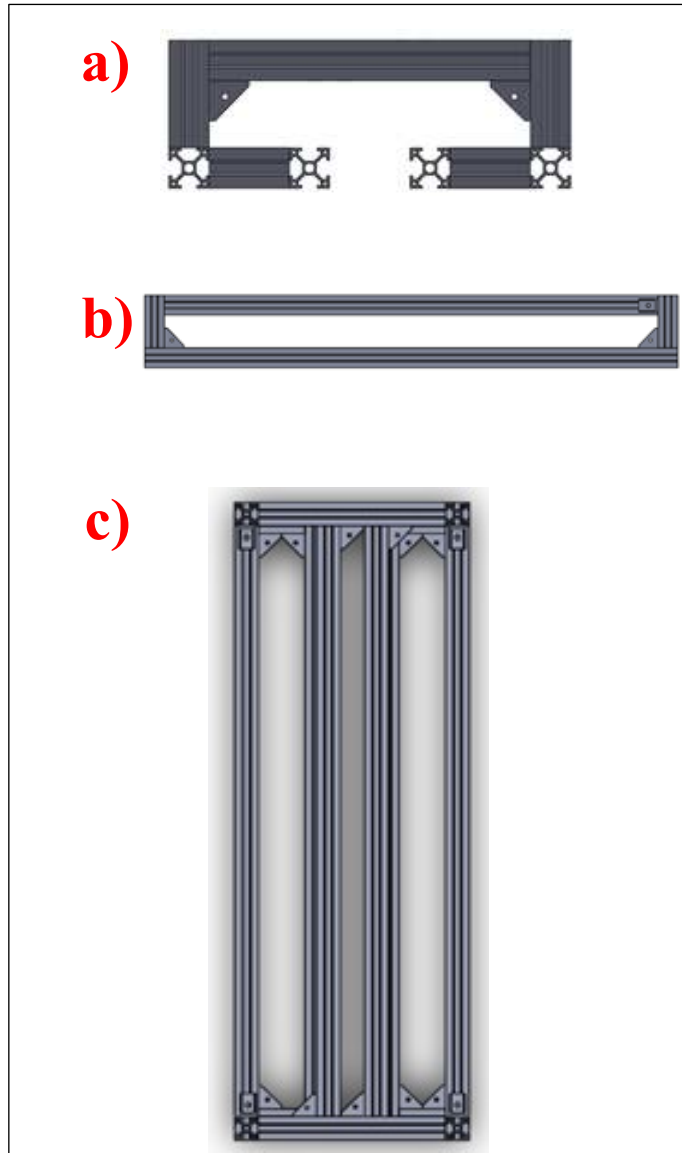
Figure III.3 *Supporting structure of the setup: a) front view; b) side view; c) top view.*

One plate (P1 in Figure III.4a) is screwed to the 4 columns of the frame and to the two horizontal profiles in the centre and in the upper part of the frame (Figure III.3b). These profiles are necessary to avoid bending of P1 in case too high normal stresses are exerted on P1, e.g. in case a roller is used to compact the powder layer. This plate is responsible to support the deposition plate (P2 in Figure III.4b). Three deposition plates can be used. Each of them presents two square trays of 10 cm by 10 cm with a fixed depth, namely 100,

200 and 300 μm, like those typical of the SLS process. The aim is to create powder layers with the same thickness as the depth of the trays.

As mentioned in paragraph I.1, layer thickness should be 2÷3 times the average particle diameter so as to guarantee sufficient direct contact between the laser and the particles. Moreover, the layer should not be too thin, i.e. one times the average particle diameter, because this would lead to segregation of particles during deposition (Goodridge, Tuck and Hague, 2012).

In case of PA6 powder the average particle diameter is 55 μm, if we consider D_{50} or $d_{4,3}$ as a reference diameter. Therefore, the layer thickness and hence the depth of the square trays of the deposition plates has to be between 110 and 165 μm. However, the setup has been built with the aim of testing many powders for SLS. Therefore, depths of 100, 200 and 300 μm, have been chosen considering possible average particle diameters, i.e. between 50 and 100 μm. In case powders with smaller particles will be tested, it will be possible to build and use new deposition plates with smaller depths of the trays.

Onto the first tray the powder is loaded. Therefore, this tray is called collection tray (CT). Then, the blade pushes the powder from the CT towards the second one, the deposition tray (DT). In particular, as will be explained in more detail in the paragraph III.3, it is possible to fix the quantity of powder which should pass at least over the whole DT. Then, the capacity of the powder to fill or not the DT depends on its capacity to be spread. Of course, to be sure that the powder will cover the DT, the quantity is chosen a little bit larger than the minimum one, which is necessary to fill the second tray. The DT is the critical part of the experimental setup because it has to guarantee the creation of layers with uniform and constant thickness. To this end, precise workmanship was requested to the manufacturer to obtain in the DT very low tolerances of form compared to the minimum depth of the tray, i.e. 100 μm. The uniformity or unevenness of the powder layer is thereby attributable only to the quality of the spreading and not to how uniform is the depth of the tray.

The powder spreading from one tray to the next one is possible by means of a "bridge". It consists of two columns, which are connected to two rods with uniform rectangular cross section by means of angles, screws and nuts. The bridge is highlighted in cobalt blue in Figure III.5.

The lower rod is connected to a ball screw (Figure III.6a) by means of a L-shaped perforated plate (Figure III.6b) and also to two linear guides (Figure III.7). The ball nut (Figure III.6b) coupled to the screw, can ensure a linear movement of the bridge because transforms the rotational movement of the screw in the translational one.
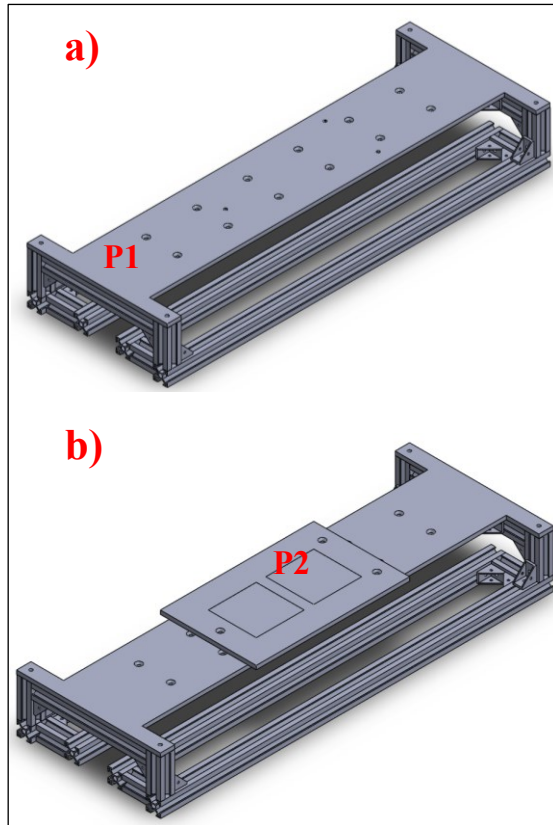
Figure III.4 *a) P1 is the plate which supports the deposition plate; b) P2 is the deposition plate.*
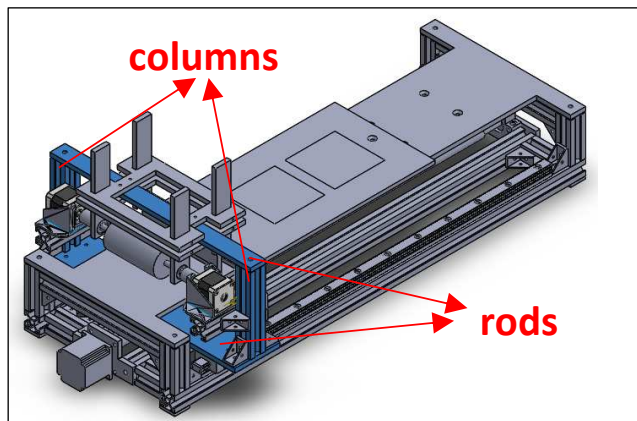
Figure III.5 *Bridge, highlighted in cobalt blue.*
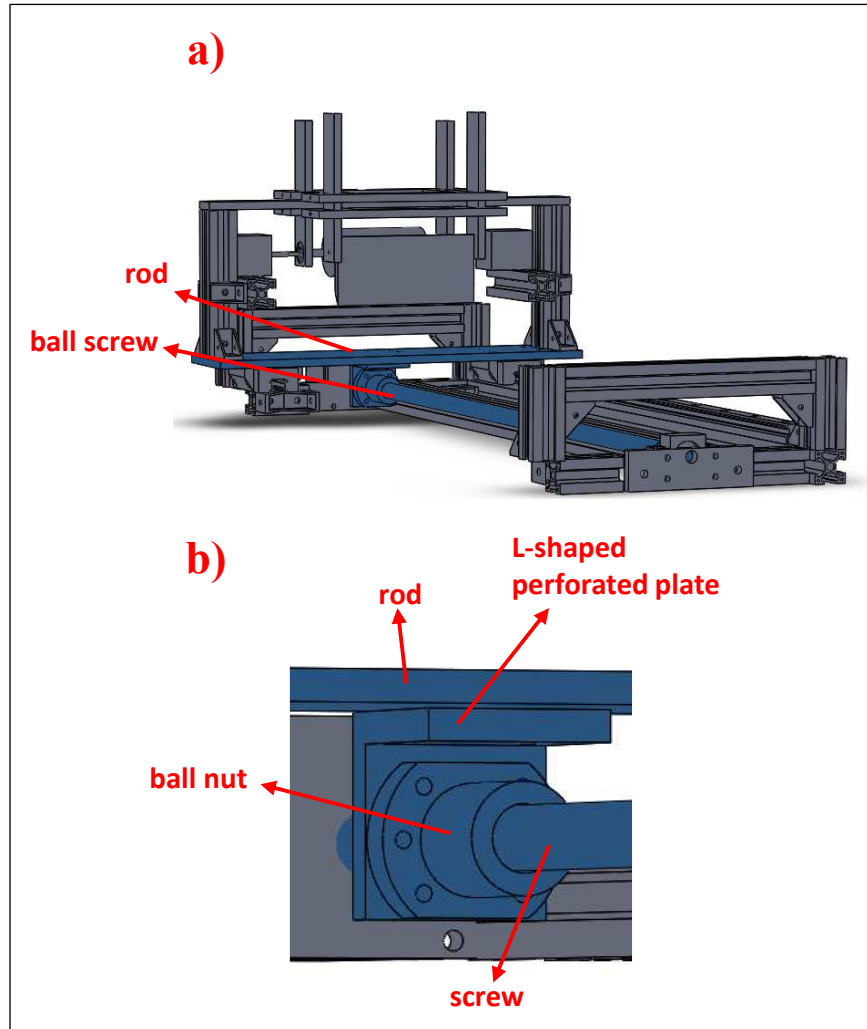
Figure III.6 *a) Coupling rod-ball screw; b) detail of the coupling.*

The ball screw is rotated by a stepper motor (Figure III.8). Two different motors have been used according to the scrolling velocity of the spreading system used in the tests, i.e. the StepSyn 103H7123-0440 of SANYO DENKI, for a velocity of 3 mm s^{-1} and the NEMA 23 Stepper Motor, for a velocity up to 3 cm s^{-1}. The ball screw is supported by a bearing support (Figure III.8), which is located opposite to the end of the screw entering the motor.
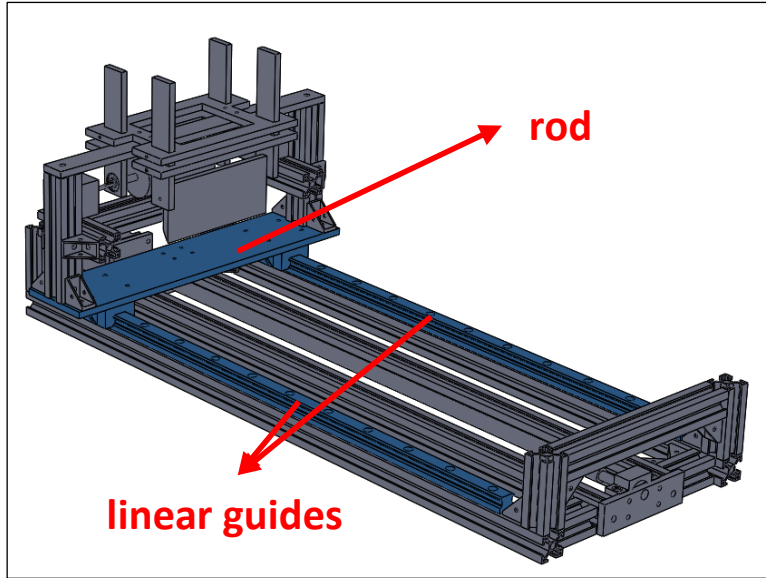
Figure III.7 *Coupling rod-linear guides.*
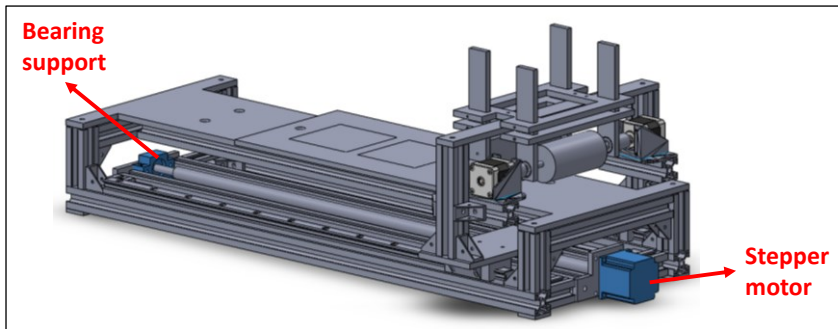
Figure III.8 *Coupling of the screw with the stepper motor and the bearing support.*

One perforated plate was used to connect the bearing to the supporting structure (Figure III.9a), and another perforated plate to connect the motor to the supporting structure (Figure III.9b).

The spreading system consists of two rectangular holders, four rods, the blade and the roller. The blade (Figure III.10) is 15 cm long, 7 cm high and 0.8 cm tick. The tip of the blade is cut so that one side of the blade has an inclination of 30° with respect to the opposite side, which is flat.

The roller is 99.98 mm long, just slightly shorter than the trays so that it can enter inside them. It has a diameter of 5 cm.
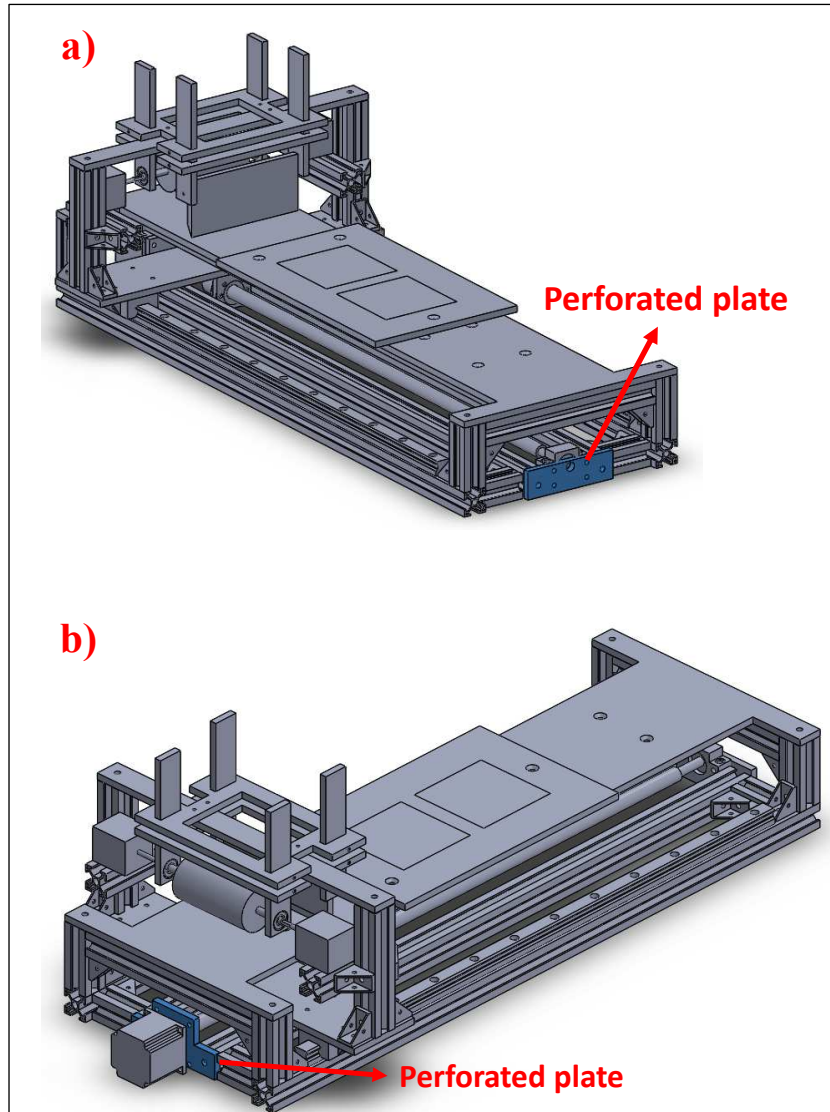
Figure III.9 *Perforated plates for the connection of: a) the bearing and b) the motor to the supporting structure.*

The holders are connected to the rod (Figure III.11a), which constitutes the upper part of the bridge (Figure III.5).

In each holder there are two rectangular holes in which the rods to keep the roller (Figure III.11a) and the blade (Figure III.11b) are inserted. The rods can be moved vertically and fixed to the holders by means of screws. By doing so, the position of the blade and of the roller can be fixed to the desired position.

Figure III.10 *a) Side and b) front view of the blade.*
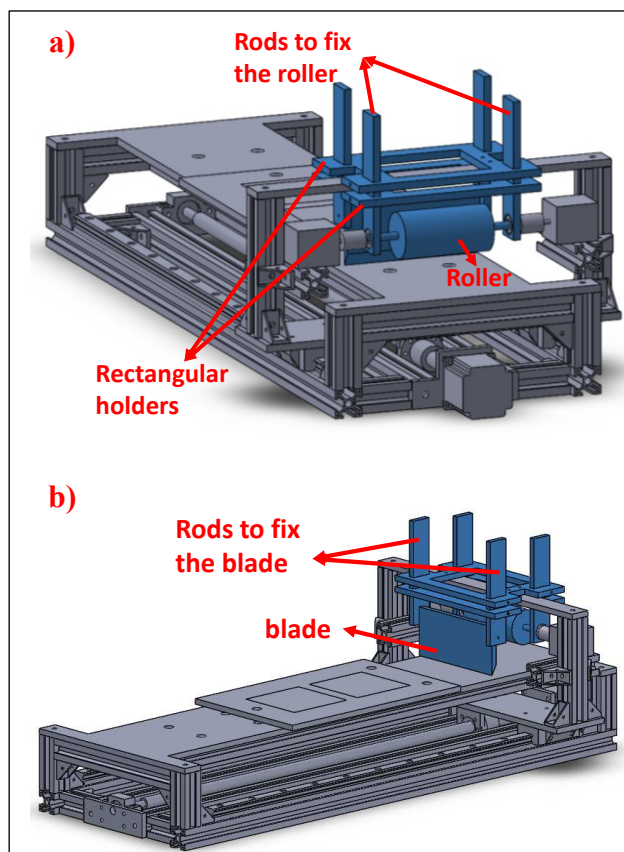
Figure III.11 *Connection of a) the roller and of b) the blade to the holders of the spreading system.*

The roller is rotated by two engines, each of which is located in a holder, connected to a profile (Figure III.12). The profile is connected to the column

49

of the bridge. A joint connects the engine to the roller shaft (Figure III.13a). Inside each rod, which keeps the roller, the ball bearing 608ZZ is inserted (Figure III.13b). The bearing allows the shaft of the roller to be sustained and to rotate.
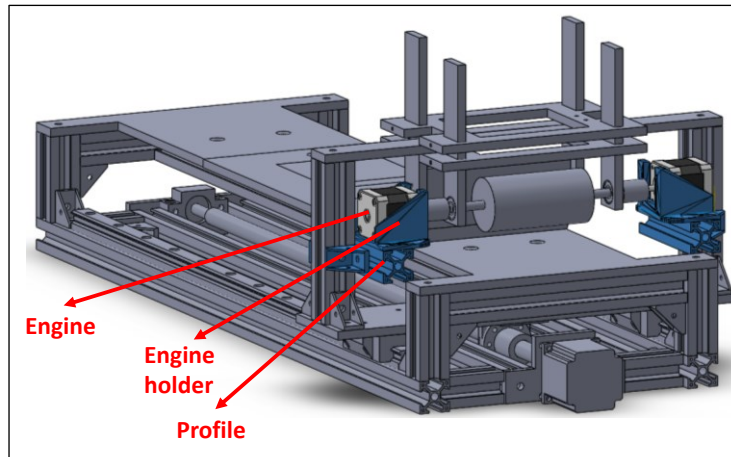
Figure III.12 *The engine support system.*
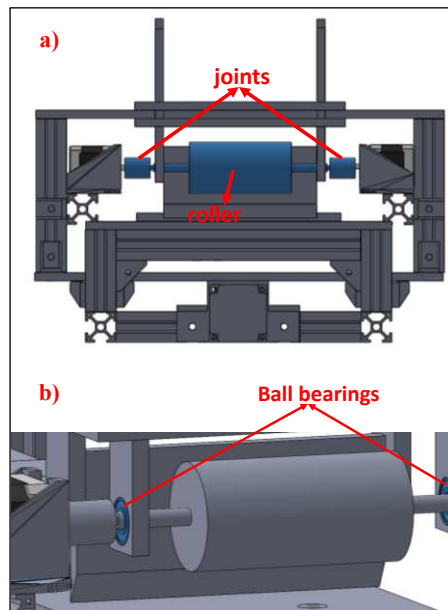
Figure III.13 *a) Connection of the engine to the roller; b) Connection of the roller to the rod.*

The main parts of the setup, namely plates P1 and P2, the blade and the roller are made of stainless steel 304L. The other parts are or in aluminium or

in stainless steel, except for the engine holders, which are made of polylactic acid and have been created by Fused Deposition Modelling.

The setup occupies an area of 88 by 40 cm and is approximately 34 cm high (Figure III.14)

Figure III.14 *Some views of the setup with the connection for the microscope and proper lightning for the image analysis of the powder layer.*

On the bridge a system for the image analysis of the powder layer through a microscope was designed and mounted. It consists of a microscope, a camera, profiles, screws, dowels, angles and connections. In particular, two long screws (Figure III.15a and b) allow the microscope to be moved in both the vertical direction (z) and the perpendicular direction (y) with respect to the spreading direction (x). The screws allow small displacements of the microscope in both the directions. Moreover, the microscope can be rotated around the y-axis (Figure III.15c) according to the θ_M angle. By rotating the screw connected to the stepper motor (Figure III.6a), it is possible to move the microscope also in the x-direction. All these movements allow to analyse the powder layer all over its surface. In particular, the displacement of the microscope in the z-direction and around the y axis allow to properly focus the surface of the powder layer to look the powder surface at the particle level. A camera was put on the microscope to take photos of the layer (Figure III.15a). The AmScope MU1603 16 MP USB3.0 connected to a computer was used. To connect the camera to the microscope and the screws to the profiles, special connections in polylactic acid (Figure III.15d) have been designed and built by means of the Fused Deposition Modelling.
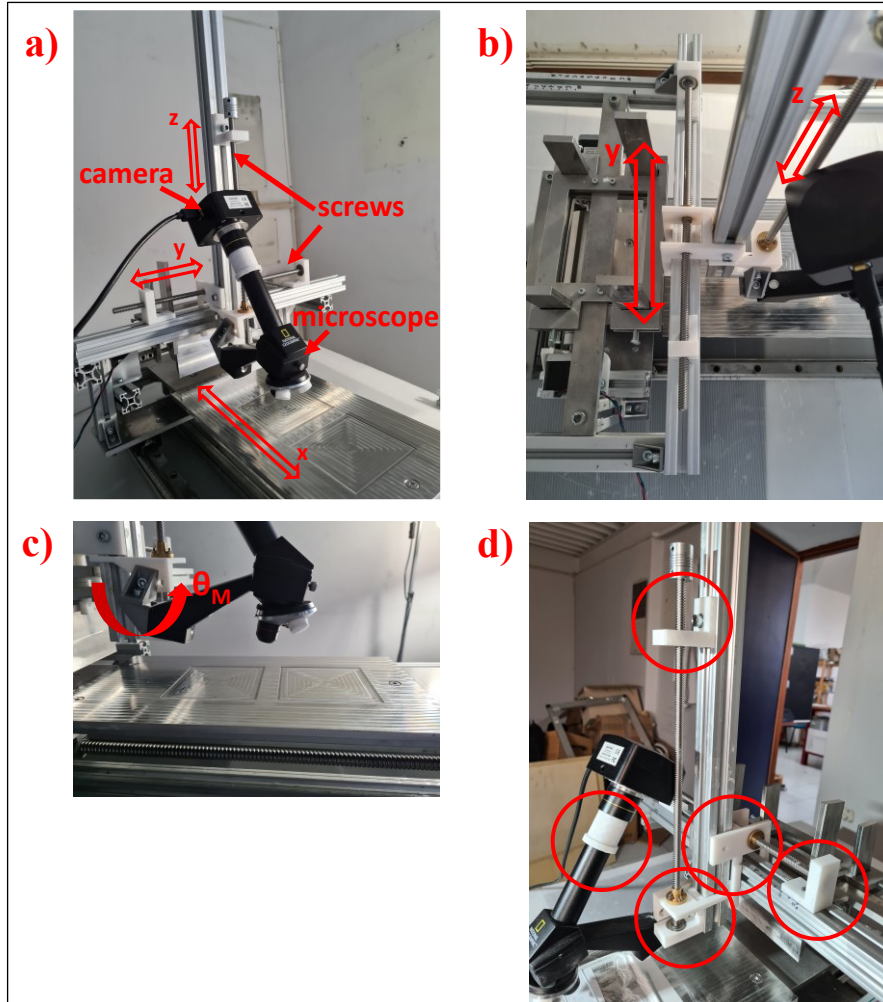
Figure III.15 *a) Movements of the microscope and the camera in x, y and z-direction; b) screws for the movements in the y and z-direction; c) rotation of the microscope and the camera around the y-direction; d) red circles that highlight the polylactic acid parts for the connection of the screws to the supporting structure and for the connection of the camera to the microscope.*

III.3 Procedure adopted to obtain a single powder layer

Before using the powder for the experiments, it was dried at 100°C for 2 hours.

The first issue encountered was to decide the appropriate amount of powder to be spread all over the CT. For this purpose, specific tests were carried out. In each test, the distance between the tip of the blade and the

deposition plate (P2) was fixed and changed from test to test. The deposition plate whose trays have a depth of 300 μm was used. The greater the distance, the greater the amount of the powder spread.

The procedure adopted in the tests consisted of the following steps:

1) The tip of the blade was fixed at a certain distance above the plate P2. Such a distance was obtained by positioning steel sheets of a feeler gauge with known thickness in the range 500 ÷ 1000 μm between the tip of the blade and P2 (Figure III.16a).

2) After having fixed the distance and removed the sheets, the powder was poured in front of the blade (Figure III.16b). Even if the powder was dried, some clusters of particles remained. Therefore, a sieve with a mesh size of 150 μm was used (Figure III.16c) to retain clusters with dimensions greater than the maximum particle diameter before pouring the powder.

3) The blade was then moved forward at a scrolling velocity of 3 mm s^{-1}. Since the distance between the CT and the DT is just 2 cm, the DT was covered with an aluminium foil to prevent powder from entering into it.

4) Once the CT was completely filled with powder, the blade was moved backward up to few centimetres before the CT (Figure III.16d).

5) The aluminium foil was removed. The powder, which was deposited outside the borders of the CT, in front and under the blade, was removed with a brush (Figure III.16e) and collected on other aluminium foils, located below P1, to avoid accumulation of powder in the linear guides, that would have compromised proper movement of the spreading system. As a result, a powder bed was obtained with length and width equal to those of the CT, namely 10 cm by 10 cm, and a height given by the distance which was fixed between the blade and P2 in step 1).

6) The blade was then dropped on P2 so that no distance remained between the blade and P2, and then moved forward. By doing so the blade displaced the powder bed from the CT to the DT (Figure III.16f).

The distance which guaranteed the total coating of the DT turned out to be 880 μm in case the scrolling velocity of the blade was 3 mm s^{-1}. The whole procedure was repeated in case the blade moved at 3 cm s^{-1}. Also in this case, a distance of 880 μm resulted to be adequate.

Therefore, the same procedure described above, with an initial distance of 880 μm between the blade and P2 and with the desired scrolling velocity of the blade, was followed to create powder layers to be analysed.

Once the blade crossed the whole DT, it was stopped, raised, fixed and moved backward up to few centimetres before the CT. At this point, all the powder outside the DT was removed by using a knife and brushes and collected in aluminium foils, located below P1. Then, the microscope was located above the powder layer inside the deposition tray for the surface analysis (Figure III.16g).
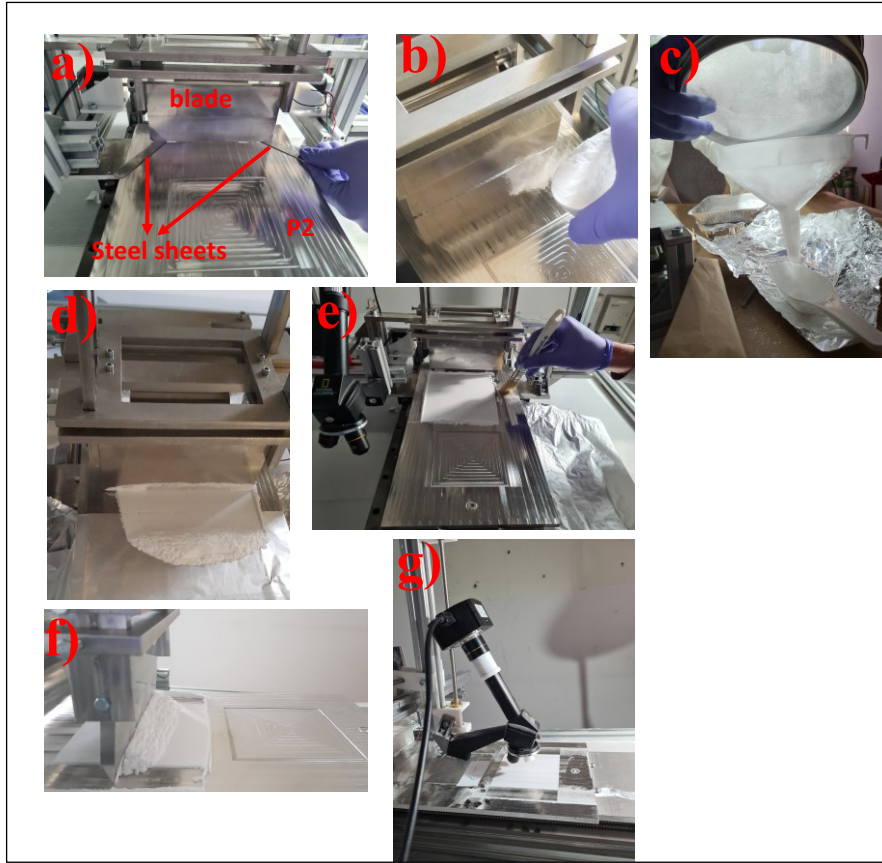
Figure III.16 *Main steps adopted for the powder layer formation in the experimental procedure: a) a gap between the blade and P1 is guaranteed; b) the powder is poured in front of the blade after being sieved (c); d) the deposition tray is covered with an aluminium foil; e) the powder outside the collection tray is removed; f) the blade spreads the powder from the collection tray to the deposition tray; g) pictures of the powder layer in different points have been taken by using a camera and a microscope.*

III.4 Method of analysis of the powder layer obtained with the

new experimental setup

The powder layer, obtained as described in paragraph III.3, was photographed by coupling the optical microscope with a 4× magnification and the camera AmScope MU1603 16 MP USB3.0.

The surface of the powder layer in the deposition tray was illuminated by a lamp with a 30 W LED with an inclination of 45° with respect to the layer.

55

By doing so the layer was invested by grazing light with the aim of highlighting unevenness on the surface, represented as brighter and darker regions on the powder surface layer. Dark regions correspond to shaded areas in the surface, while bright regions correspond to the lighted areas. Shadows appear on the side of the surface asperities and therefore provide an indication of the width of the surface roughness.

Both the microscope and the camera could be fixed in the desired position by using the supporting system described in paragraph III.2.1.1. The advantage of connecting the microscope and the camera to the bridge is that it was possible to look at the powder layer in different points in the same conditions of illumination and at the same distance from the microscope. As a consequence, from the photos it is possible to make a proper comparison both between different points of the same layer and between different powder layers, obtained in the same or different spreading conditions, in the same point.

The microscope images were taken following a specific methodology. The surface of the powder layer was ideally divided in a matrix composed of 10 rows and 10 columns, i.e. 100 cells with length and width of 1 cm (Figure III.17). In order to make a comparison between the photos and the simulated layers, the camera was fixed in correspondence of the fifth row, which is sufficiently far from the walls of the tray. In fact, as will be described in paragraph IV.4.1, in the simulations a portion of the powder layer was replicated with the assumption that the behaviour of the powder in the portion is representative of the powder behaviour far from the walls. Photos along $1.5 \cdot 10^{-2}$ m of the powder layer were taken for the comparison, namely along the cells number 5 and half the cell number 15 (Figure III.17). $1.5 \cdot 10^{-2}$ m of the powder layer corresponded to $80 \div 90$ pictures. In fact, the microscope, as it was used, was able to focus on the centre of the picture. Therefore, to have the whole portion of the powder layer in-focus, many pictures had to be taken. Each picture captured a layer height of 1250 μm.

I	1	11	21	31	41	51	61	71	81	91
II	2	12	22	32	42	52	62	72	82	92
III	3	13	23	33	43	53	63	73	83	93
IV	4	14	24	34	44	54	64	74	84	94
V	5	15	25	35	45	55	65	75	85	95
VI	6	16	26	36	46	56	66	76	86	96
VII	7	17	27	37	47	57	67	77	87	97
VIII	8	18	28	38	48	58	68	78	88	98
IX	9	19	29	39	49	59	69	79	89	99
X	10	20	30	40	50	60	70	80	90	100

Figure III.17 *Ideal representation of the powder layer as a matrix of 10 rows (I to X) and 10 columns to form 100 cells, 1 cm by 1 cm each. The spreading direction corresponds to a movement along different columns, e.g. from 1 to 91. The red hyphenated rectangle highlights the examined portion of the powder layer, that is cell number 5 and half the cell number 15. However, the actual width of the examined powder layer is less than 1 cm since it depends on the height of the pictures, i.e. 1250 µm*

Marks 1 cm apart were drawn along the horizontal profile to which the microscope was connected (Figure III.18.a) to fix its position in correspondence of the fifth row. Further marks on the profile to which one linear guide was connected were drawn (Figure III.18.b) to check the microscope position along the spreading direction, i.e. along cells of different columns for the same row. The microscope was displaced in the spreading direction by manually rotating the screw connected to the motor. By doing so, small advancements of the microscope could be carried out.
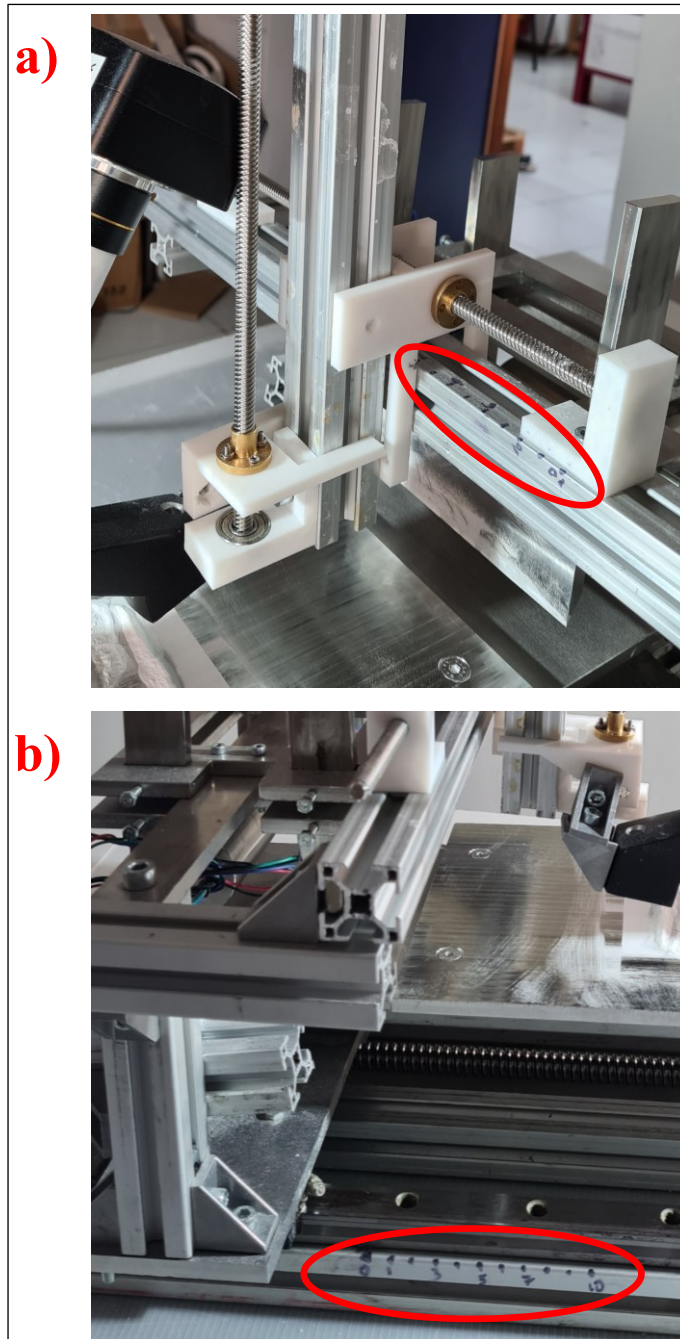
Figure III.18 *a) Marks drawn on the horizontal profile to regulate the position of the microscope and of the camera along different rows; b) marks drawn to regulate the position along different columns, i.e. along the spreading direction.*

Before taking photos of the powder surface, a calibration procedure was carried out to measure exactly the dimension of the objects detected by the camera. A microscope slide with a graduated scale drawn on it was placed inside the empty collection tray (Figure III.19). In this way the slide was at the same position of the powder within the deposition tray with respect to the microscope. The distance between two tick marks was 100 μm. Then, the microscope lens was approached to the slide in order to have good focus of the scale drawn on the slide and captured by the camera. By using the software of the camera, the distance between the marks was registered for the calibration. Calibration revealed that each picture taken from the camera had a height of 1250 μm and a width of 1650 μm.

Figure III.19 *Calibration procedure based on the measure of the distance between two tick marks on the microscope slide by using the microscope coupled with the camera.*

Pictures like those reported in Figure III.20 were taken. Since the pictures were not completely in-focus (Figure III.21a), they were overlapped (Figure III.21b) to have a clear and continuous representation of the portion of the powder layer, which was captured. For example, pictures of Figure III.21a presented some parts which were not in focus, i.e. the regions in the red hyphenated rectangles. Therefore, these regions were removed by overlapping the pictures and by cutting the remaining parts not in-focus (Figure III.21b). This procedure was followed for all pictures till obtaining a sequence of in-

focus images. The length of the final image obtained by combining single images was approximately 1.5·10⁻² m.
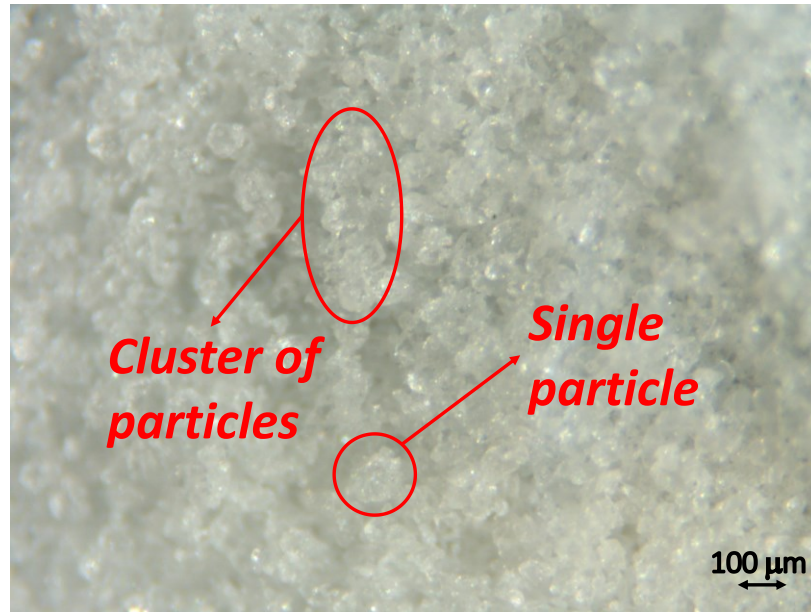
Figure III.20 *Image of the powder layer taken by the camera coupled with the microscope. Some particles are highlighted in the figure.*
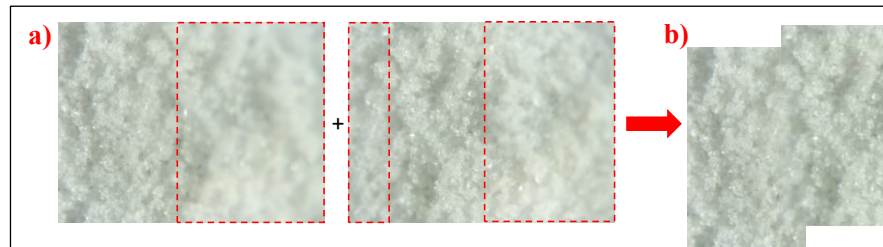
Figure III.21 *a) Regions not in-focus (within the red hyphenated rectangles) are identified and cut off; b) The images are overlapped to obtain a continuous in-focus picture.*

However, to obtain the image of a layer with a height of 950 μm and a length of 1.5·10⁻² m, the ImageJ software (NIH), was used. These dimensions were chosen with the purpose of making a comparison between the images of the layers obtained from the experiments and those obtained from the simulations.

Since the height of a single image taken from the microscope was recorded with the calibration procedure previously described, in ImageJ it was possible

to set the actual scale (Figure III.22a) and consequently to cut out a rectangle with the sides of the same desired dimensions of the layer, namely 950 μm and $1.5 \cdot 10^{-2}$ m (Figure III.22b). The final image obtained is like the one reported in Figure III.22c.
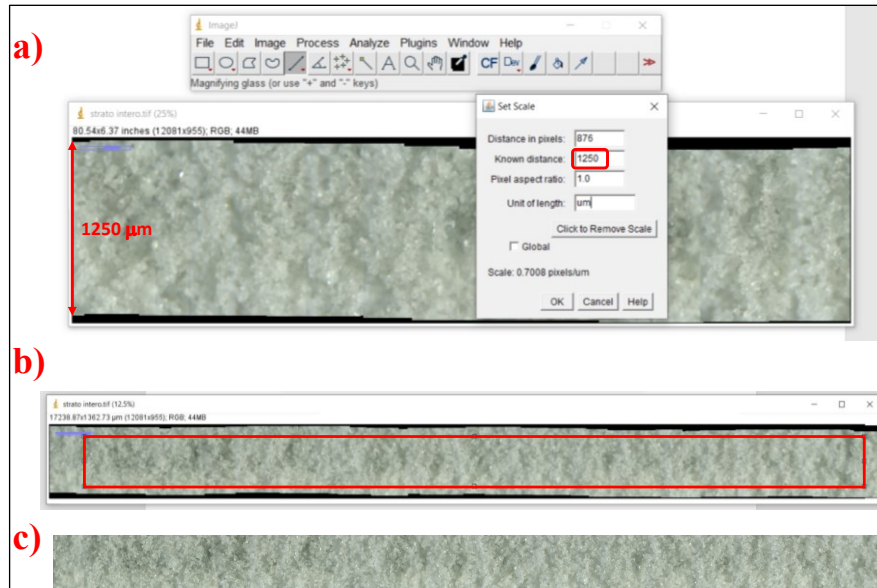
Figure III.22 *Steps with ImageJ to obtain the image of the powder layer: a) the actual scale is set; b) a rectangle with the desired dimensions is cut out from the aligned images; c) the cropped image is obtained*

Microsoft Paint was used to get the same pixels for the height of images of different tests. Such operation was necessary to analyse the images with the MATLAB by MathWorks.

III.4.1 *Wavelet power spectrum: Introduction*

Signal analysts can use many tools. Among these is Fourier analysis, which splits a signal into constituent sinusoids of different frequencies. Therefore, it transforms the signal from time based to frequency based. However, Fourier analysis has the disadvantage of losing time information when the signal is represented in the frequency domain. Therefore, the Fourier transform of a signal does not allow to understand when a particular event took place. In case the signal properties do not change much over time, that is if it is stationary, this drawback is not very important.

However, most interesting signals contain numerous non-stationary or transitory characteristics such as abrupt changes and beginnings and ends of

events. These characteristics are often the most important part of the signal, and Fourier analysis is not able to detect them.

A *wavelet* is a waveform of limited length that has an average value of zero. Sinusoids (Figure III.23a), which are the basis of Fourier analysis, do not have limited duration (they extend from minus to plus infinity) and are smooth and predictable. Instead, wavelets (Figure III.23b) can be irregular and asymmetric (Wavelet Toolbox^{TM} 4 User's Guide).

Wavelet analysis allows the use of long-time intervals where precise low-frequency information are required, and shorter regions where high-frequency information are required.

Fourier analysis consists of breaking up a signal into sine waves of various frequencies. Similarly, wavelet analysis consists of breaking up the signal into shifted and scaled versions of the original wavelet, called mother wavelet.

Looking at Figure III.23 it is intuitive to think that signals with sharp changes might be better analysed with an irregular wavelet than with a smooth sinusoid.
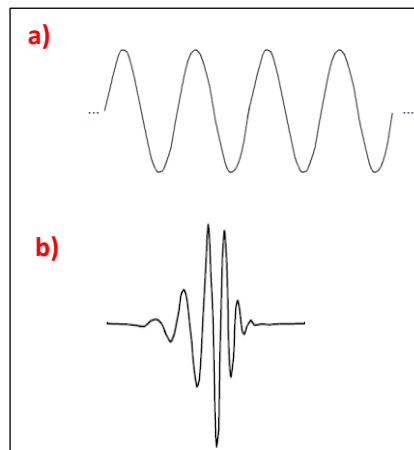
Figure III.23 *a) Sinusoid; b) Generic wavelet (* Wavelet Toolbox^{TM} 4 *User's Guide*)

Wavelets can develop in time or space and therefore have a number of applications. In fact, wavelet techniques are used in many fields such as biology (Pavlov *et al.*, 2006), geo-sciences and geophysics (Foufoula-Georgiou and Kumar, 1994; Kumar and Foufoula-Georgiou, 1997; Polanco-Martínez and Faria, 2018), remote sensing in vegetation analysis (Ben Abbes *et al.*, 2018), engineering (Kompella, Mannam and Rayapudi, 2016; Islam, Pears and Bacic, 2018), hydrology (D. Wang *et al.*, 2018), finance (Jia *et al.*, 2017), medicine (Alickovic, Kevric and Subasi, 2018), ecology (Cazelles *et al.*, 2008), renewable energy (Chiang *et al.*, 2017).

Wavelet Power Spectrum has been applied to get the complete size distribution of apparent grain axes in an image of sediment (Buscombe, 2013).

Wavelet analysis is also able to detect from road roughness data the occurrences and locations of localized surface irregularities caused by pavement distresses such as surface raveling, depressions, potholes, humps (Wei, Fwa and Zhe, 2005). Therefore, this wavelet analysis is able to provide useful information for network pavement management and pavement maintenance operations.

With reference to time dependent phenomena, wavelets can be used for the detection of ruptures and edges and to study short-time phenomena as transient processes. Wavelets transform can determine whether a quick signal exists and, in case, localize it.

There are many different mother wavelets that can be used in the continuous wavelet transform (CWT). Depending on what signal features one wants to detect, the wavelet that facilitates the detection of that feature will be selected (Continuous Wavelet Transform and Scale-Based Analysis - MATLAB & Simulink - MathWorks Italia).

Among the most common mother wavelets are: Morse (Morse Wavelets - MATLAB & Simulink - MathWorks Italia), Haar, Daubechies, Biorthogonal, Coiflets, Symlets, Morlet, Mexican Hat, Meyer (Wavelet Toolbox^{TM} 4 User's Guide).

Wavelet analysis can be applied to one-dimensional signals as well as two-dimensional data, i.e. images.

The CWT is defined as the sum over all time of the signal, $f(t)$, multiplied by scaled, shifted versions of the wavelet function (Ψ) as follows:

$$C_W\ (scale, position) = \int_{-\infty}^{+\infty} f(t) \cdot \Psi(scale, position, t)\ dt \tag{25}$$

The results of the CWT are many wavelet coefficients (C_W), which are a function of scale and position.

Multiplying each coefficient by the appropriately scaled and shifted wavelet yields the original signal (Figure III.24).
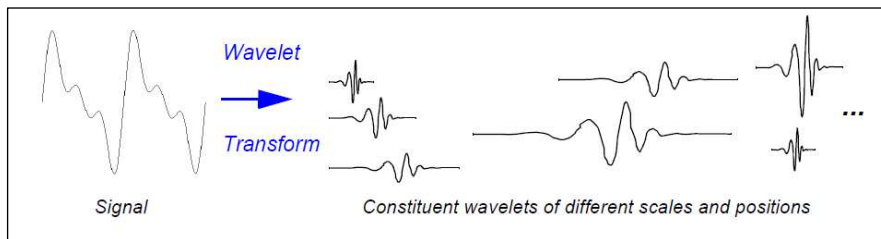
Figure III.24 *Transformation of the signal in wavelets by using the wavelet transform (Wavelet Toolbox^{TM} 4 User's Guide).*

If the signals are recorded in the space domain in place of the time domain the application of the wavelet theory is not affected. The theory here presented is still valid and applicable if the variable t in eq. (25) is taken to represent distance instead of time (Wei, Fwa and Zhe, 2005).

III.4.1.1 Scaling and shifting

Scaling a wavelet means stretching or compressing it. The parameter by which the wavelet is scaled is the scale factor, indicated by a_f. The smaller the scale factor, the more "compressed" the wavelet (Figure III.25). The scale is related to the frequency of the signal.

$$f(t) = \psi(t) \quad ; \quad a_f = 1$$

$$f(t) = \psi(2t) \quad ; \quad a_f = \frac{1}{2}$$

$$f(t) = \psi(4t) \quad ; \quad a_f = \frac{1}{4}$$
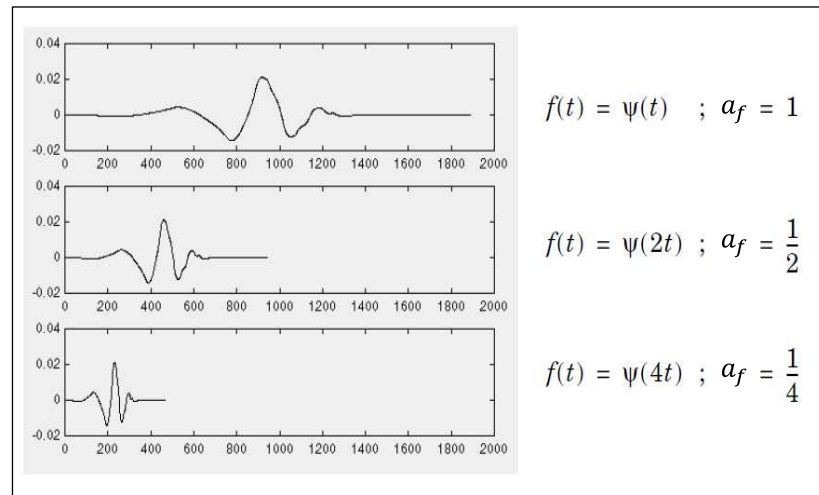
Figure III.25 *Examples of a signal with different scale factors (a_f) (Wavelet Toolbox^{TM} 4 User's Guide).*

Shifting a wavelet simply means delaying or anticipating its onset. An example of delay of a function by k is represented in Figure III.26.

Wavelet function
$\psi(t)$

Shifted wavelet function
$\psi(t-k)$
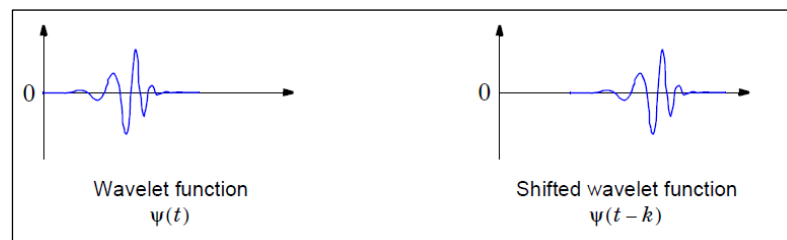
Figure III.26 *Example of a wavelet function (left) and its shifting by k (right) (Wavelet Toolbox^{TM} 4 User's Guide).*

64

III.4.1.2 Continuous Wavelet Transform and Wavelet Power Spectrum

CWT is considered continuous because of the set of scales and positions at which it operates. Unlike the discrete wavelet transform, the CWT can operate at every scale. The CWT is also continuous in terms of shifting. Indeed, during computation, the analysing wavelet is shifted smoothly over the full domain of the analysed function.

CWT produces wavelet coefficients that are a function of scale and position. The five steps for creating a CWT are:

1) A wavelet is taken and compared to a section at the beginning of the original signal (Figure III.27a);

2) The wavelet coefficient (C_W) which represents how the wavelet is closely correlated with this section of the signal, is calculated. The higher C_W is, the more the similarity. The results will depend on the shape of the wavelet one chooses;

3) The wavelet is shifted to the right and the steps 1 and 2 are repeated until the whole signal is covered (Figure III.27b);

4) The wavelet is scaled (stretched) (Figure III.27c) and steps 1 through 3 are repeated;

5) Steps 1 through 4 are repeated for all scales.

At the end of the procedure, the coefficients produced at different scales by different sections of the signal will be calculated. The coefficients constitute the results of a regression of the original signal performed on the wavelets.

Once the coefficients are calculated, a plot, called scalogram, can be represented where the *x*-axis represents position along the signal (time or distance), the *y*-axis represents scale, and the colour at each *x*-*y* point represents the magnitude of the wavelet coefficient. These coefficient plots resemble an irregular surface viewed from above (Figure III.28a). When the same surface is looked from the side, a plot like the one reported in Figure III.28b is obtained.
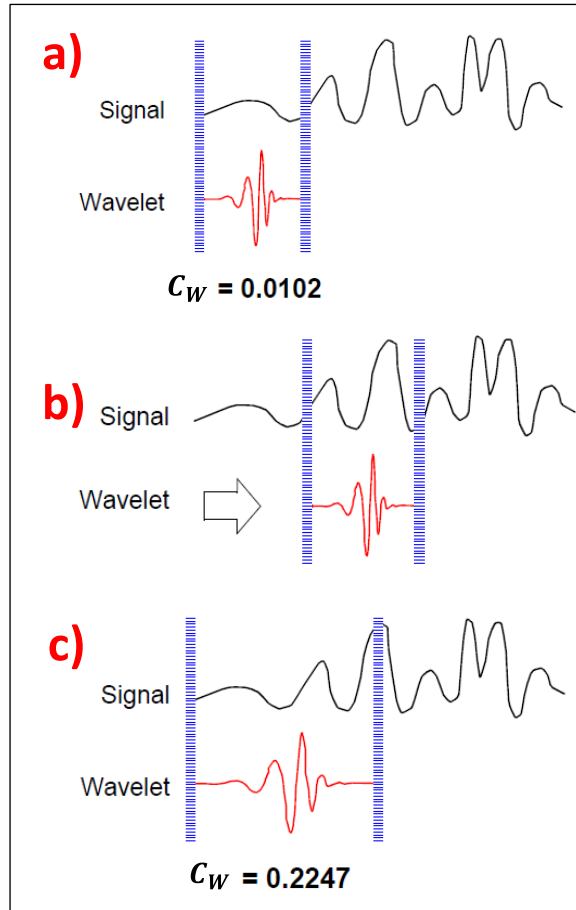
Figure III.27 *Main steps for creating a CWT: a) A wavelet is taken and compared to a section at the beginning of the signal and the wavelet coefficient (C_W) is calculated; b) The wavelet is shifted to the right and the corresponding C_W is calculated; c) The wavelet is scaled (stretched) and C_W is calculated (Figure III.27c) (Wavelet Toolbox^{TM} 4 User's Guide)*
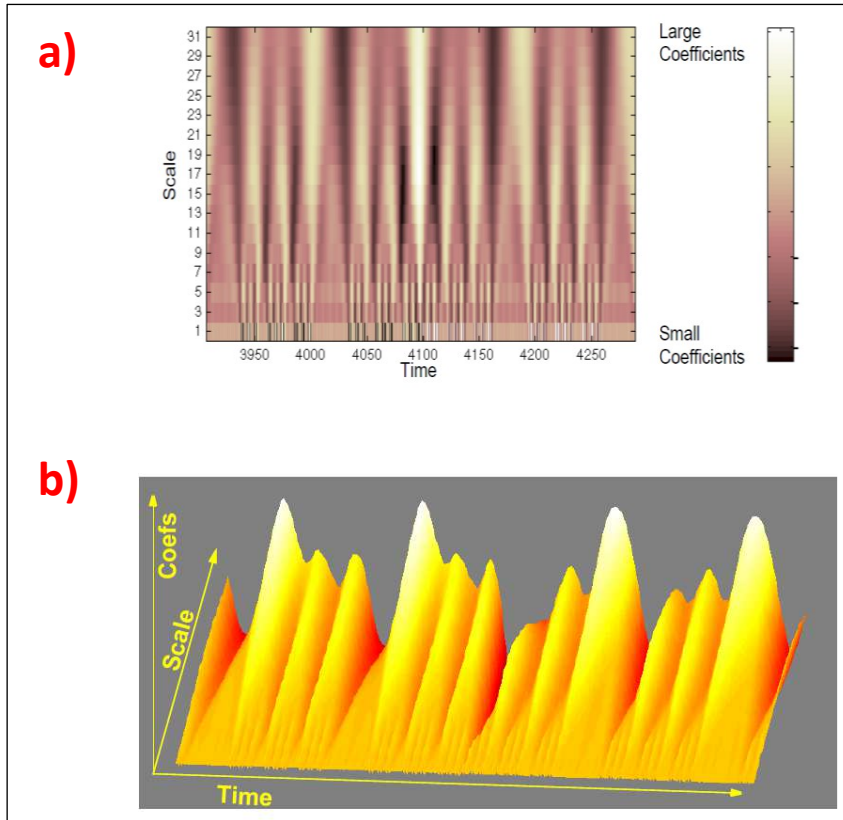
Figure III.28 *Scalogram: two (a) and three dimensional (b) representations (Wavelet Toolbox^{TM} 4 User's Guide).*

In paragraph III.4.1.1, it has been said that higher scales correspond to the most "stretched" wavelets. The more stretched the wavelet, the longer the portion of the signal with which it is being compared, and thus the coarser the signal features being measured by the wavelet coefficients.

Thus, there is a correspondence between wavelet scales and frequency as revealed by wavelet analysis:

1) Low scale (a_f) corresponds to compressed wavelet and hence rapidly changing details are captured. That means high frequency (ω_a).

2) High scale (a_f) corresponds to stretched wavelet and hence slowly changing, coarse features. That means low frequency (ω_a).
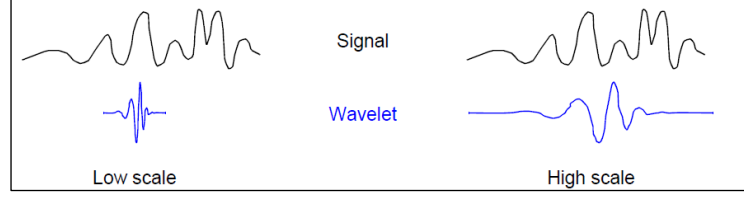
Figure III.29 *High frequency (left) and low frequency (right) wavelets.*

The equation which relates ω_a to a_f is the following one (Scale to frequency - MATLAB scal2frq - MathWorks Italia):

$$\omega_a = \frac{\omega_w}{a_f} \tag{26}$$

where ω_w is the center frequency of the wavelet, namely the frequency corresponding to its wider oscillation.

A useful approach to reduce all the information contained in the scalogram to a single two-dimensional spectrum and to easily compare information coming from different signals, is to make an average of all the wavelet coefficients, calculated as described previously, along the time (distance) axis. As a result, a plot of the average values of the wavelet coefficients for the whole signal as function of the corresponding frequency is obtained. Such a plot is the scale-averaged wavelet power spectrum of the signal (Scale-averaged wavelet spectrum - MATLAB scaleSpectrum - MathWorks Italia). The *wavelet power spectrum* is the obtained by time-averaging the magnitude-squared scalogram over all times, that is by time-averaging the squared-wavelet coefficients. This spectrum is also useful to compare different signals (Ferrari, M. (2014))

III.4.2 *Analysis of the powder layer quality: Wavelet Power Spectrum*

Once the images of the powder layer were obtained from the experimental tests, as explained in paragraph III.4, they were analysed in MATLAB by using its "Wavelet Toolbox". The aim was to derive the wavelet power spectrum for each image and consequently to infer information regarding the quality of the powder layer.

The procedure adopted in MATLAB consists of the following steps:

1) The image is opened in MATLAB;

2) It is converted from the RGB to the greyscale image. The resulting image is represented in MATLAB as a matrix of elements. Each element is a pixel with a specific brightness level and it is represented by a integer. Being the matrix in the uint8 format, namely the image can be represented by a number of 1-byte (8-bit) unsigned integers, then the matrix can store 256

distinct shades of grey between 0, which represents the black colour, and 255, which represents the white colour. The matrix is composed of *h* rows and *l* columns, where *h* is the height of image in pixels and *l* is the width of image in pixels (Figure III.30);

3) In each image strip three different one-dimensional grey level traces are obtained along the spreading direction in three different positions of the image along the y-direction (Figure III.31): middle (M), upper (U) and lower (L) part of the image. For each position (M, U and L), strips made of 15 different adjacent rows are taken. Such width corresponds approximately to twice the particle diameter D_{50}. Indeed, it was verified that this height guarantees almost the same signal obtained for larger strips, i.e. greater than twice D_{50}.

For each strip a grey level trace along the x-direction (Figure III.31) is obtained as the average value of the pixels belonging to the 15 rows at the same x position. For the L, M and U parts, the rows which were considered are: from the 23rd to the 37th, from the 53rd to the 67th and from the 83rd to the 97th row, respectively.
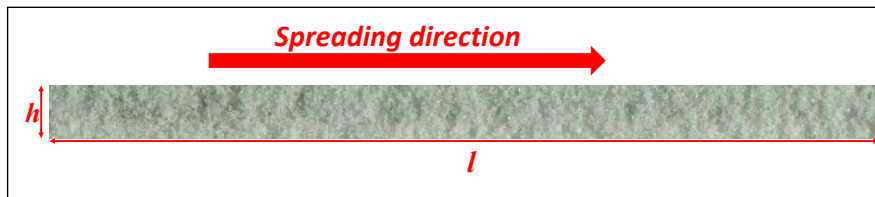
Figure III.30 *Image of a portion of the powder layer with a height (h) of 950 μm and a width (l) of $1.5 \cdot 10^{-2}$ m.*

4) CWT is applied to each of the final three averaged traces to obtain the power spectrum (PS) that is function of the wavenumber. The default Morse wavelet is used (Morse Wavelets - MATLAB & Simulink - MathWorks Italia);

5) Final PS is obtained as the average of the power spectra obtained from the three signals related to the M, U and L portions of the layer;

6) The peak of the PS and the range of values of the wavenumber are identified. The range is such that the values of the power in correspondence of the extremes of the range are the two thirds of the PS peak value (Figure III.32). By doing so, a range of wavenumbers is identified. Such a range of wavenumbers corresponds to a range of wavelengths, which are assumed to be representative of the characteristic dimension of the powder surface roughness. The objective was to derive useful information about the quality of the powder layer after its distribution with the spreading tool.

Details about the used code are reported in Appendix B.
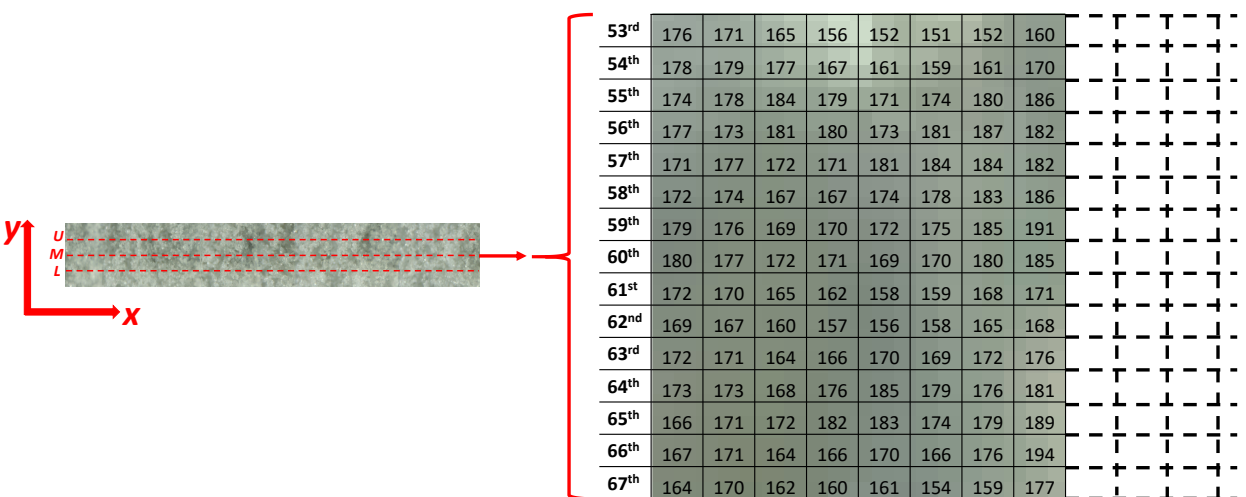
Figure III.31 *15 rows for each position (U, M and L) have been considered. For example, for the M position, the rows from the 53rd to the 67th of the matrix (representative of the image) have been extracted to obtain the signal of pixels in the central part of the layer.*
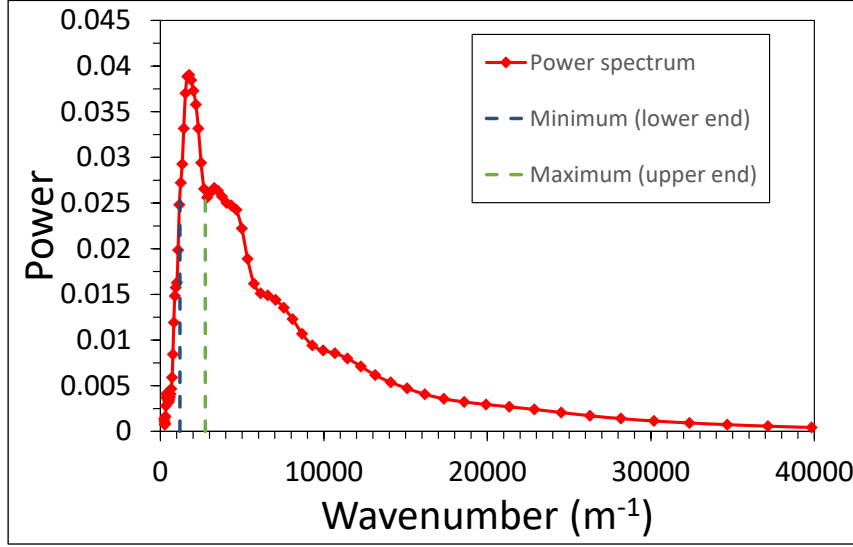
Figure III.32 *Example of power spectrum (red line). Blue and green hyphenated lines identify the lower and the upper end of the wavenumber range around the peak.*

III.5 Evaluation of the aggregate size from the Bo number

Bond number (Bo) is defined as follows:

$$Bo = \frac{F_{int}}{W_p} \tag{27}$$

where F_{int} is the interparticle force for the unconsolidated material and W_p is the particle weight. W_p is defined as follows:

$$W_p = \rho_p \frac{\pi d_{4,3}^3}{6} g \tag{28}$$

where ρ_p is the particle density, $d_{4,3}$ is the volume mean diameter and g is the acceleration due to the gravity.

The Rumpf equation (Rumpf, 1962), which was originally derived to relate the strength of particle clusters to the average value of interparticle forces, can be used conversely to estimate F_{int} from the isostatic tensile strength of the unconsolidated material σ_0, as follows:

$$F_{int} = \sigma_0 d_{3,2}^2 \frac{\varepsilon_0}{1 - \varepsilon_0} \tag{29}$$

71

where $d_{3,2}$ is the Sauter mean diameter and ε_0 is the powder voidage calculated from the powder bulk density, estimated for the unconsolidated material by linearly extrapolating the bulk density to zero consolidation, i.e. $\sigma_1 = 0$.

Therefore:

$$Bo = \frac{\sigma_0 \, d_{3,2}^2 \, \frac{\varepsilon_0}{1 - \varepsilon_0}}{\rho_p \frac{\pi d_{4,3}^3}{6} g} \tag{30}$$

The hypothesis of the Rumpf (Rumpf, 1958) and Molerus (Molerus, 1975) model are:

- Spherical particles with monodispersed distribution;
- Random packing of particles;
- The contact surfaces between the particles are small enough compared to the particle diameter to be regarded as contact points;
- Isotropic packing;
- Uniform distribution of the contact points between the particles;
- Isostatic state of stress.

Two different approaches could be used to evaluate σ_0, as also proposed by Ruggi et al. (Ruggi, Lupo, *et al.*, 2020).
According to Medhe et al. (Medhe, B Pitchumani and Tomas, 2005), σ_0 is coincident with the intersection with the normal stress axis of the Dynamic Yield Locus (DYL), that is the yield locus tangent to the Mohr circles representing the stress state under stationary deformation. Therefore, it is also called Stationary Yield Locus. The DYL can be often linearized with a good degree of approximation as follows:

$$\tau = (\sigma + \sigma_0) \tan \phi_{st} \tag{31}$$

where ϕ_{st} is the slope angle of the linearized DYL.
Figure III.33 reports the linearized Static Yield Locus and the linearized DYL.
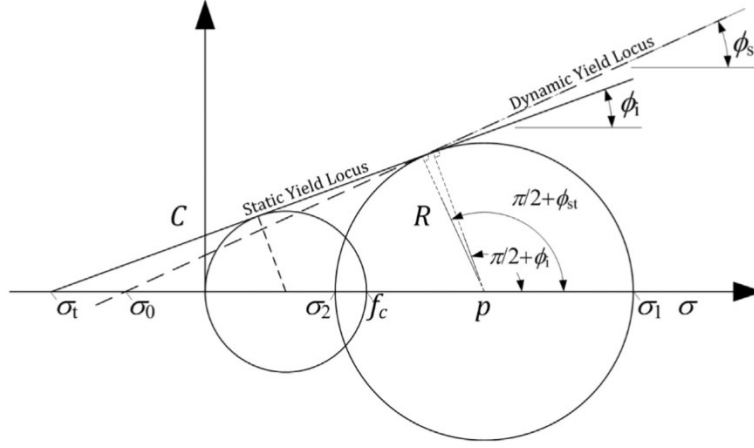
Figure III.33 *The static and the stationary (dynamic) yield locus plotted together* (Ruggi, Lupo, *et al.*, 2020).

Based on the graph of Figure III.33, Medhe et al. (Medhe, B. Pitchumani and Tomas, 2005), found the following relationship:

$$f_c = \frac{2(\sin\phi_{st} - \sin\phi_i)}{(1+\sin\phi_{st})(1-\sin\phi_i)}\,\sigma_1 + \frac{2\sin\phi_{st}\,(1+\sin\phi_i)}{(1+\sin\phi_{st})(1-\sin\phi_i)}\,\sigma_0 \qquad (32)$$

where: f_c is the unconfined yield strength, ϕ_i is the static angle of internal friction and σ_1 is the major principal stress.

Eq. (32) indirectly implies that the flow function, that is f_c as function of σ_1, can be approximated by a line, if the static angle of internal friction is independent of the powder consolidation. Therefore, eq. (32) can be used to estimate ϕ_{st} and σ_0 by applying a linear regression on the powder flow function (f_c vs σ_1). The slope of the regression line can be used to calculate ϕ_{st} from the coefficient of σ_1 in eq. (32). Given the value of ϕ_{st} the value of σ_0 can be calculated from the intercept of the same linear regression.

An alternative procedure could be applied to estimate σ_0. It follows the procedure reported in some works to estimate the agglomerate size of cohesive powders in aerated discharge (Barletta, Donsi, *et al.*, 2007a), vibrated fluidization (Barletta and Poletto, 2012) and SLS (Ruggi, Barrès, *et al.*, 2020), respectively. These applications have in common the fact that the powders are used at very low consolidation condition. Therefore, the results obtained with a shear cell have to be extrapolated. In particular, values of the static angle of internal friction as well as the cohesion (C) have to be extrapolated in correspondence of $\sigma_1 = 0$ (zero consolidation) in order to calculate the values ϕ_{i0} and C_0 for each of the tested powder. From these values the corresponding σ_0 can be obtained following the geometry of the Static Yield Locus (Figure III.33):

73

$$\sigma_0 = \frac{C_0}{\tan \phi_{i0}} \tag{33}$$

Eq. (27) reveals that the ability of a single particle to flow depends on the relative importance of the interparticle forces and of the particle weight.

From the Bo number it is possible to know at least the order of magnitude of the particle aggregate dimension. Since the Bo number increases with the interparticle force, it seems to be reasonable to think that it is proportional to the number of the particles in the aggregate. In fact, the more cohesive the powder, the larger the number of particles which constitute the aggregate.

Therefore, if it is assumed that:

$$Bo \approx n \tag{34}$$

where n is the number of particles of the aggregate, then:

$$V_a = n \times V_p = n \times \left(\frac{\pi D_{50}^3}{6}\right) \approx Bo \times \left(\frac{\pi D_{50}^3}{6}\right) \tag{35}$$

where V_a is the volume of the particle aggregate, V_p is the volume of a single particle and D_{50} is the particle diameter corresponding to the 50th percentile of the cumulative particle size. Therefore:

$$V_a = \frac{\pi D_a^3}{6} \approx Bo \times \left(\frac{\pi D_{50}^3}{6}\right) \Leftrightarrow D_a \approx Bo^{1/3} \times D_{50} \tag{36}$$

Eq. (36) shows how it is possible to roughly estimate the order of magnitude of the aggregate diameter (D_a) from the Bo number and the particle diameter.

III.6 Evaluation of the Interfacial surface energy between the particles from the Rumpf equation

In the previous paragraph, the relationship between the interparticle force and the isostatic tensile strength has been reported (eq. (29)). If we assume that the interparticle force so evaluated equals the maximum tensile force required to break the contact between two particles namely the pull-out force of the JKR model, as defined in eq. (22), then it is easy to calculate the interfacial surface energy between the particles (Γ_{P-P}). Indeed:

$$F_{int} = \sigma_0\, d_{3,2}^2\, \frac{\varepsilon_0}{1-\varepsilon_0} = \frac{3}{2}\, \pi\, \Gamma_{P-P}\, R^* = F_{pullout} \tag{37}$$

If we assume $d_{3,2} = 2R$ as reference for the particle diameter, then:

$$\frac{1}{R^*} = \frac{1}{R} + \frac{1}{R} = \frac{4}{d_{3,2}} \tag{38}$$

By combining eqs. (37) and (38), then:

$$\Gamma_{P-P} = \frac{\sigma_0\, d_{3,2}^2\, \dfrac{\varepsilon_0}{1-\varepsilon_0}}{\dfrac{3}{2}\, \pi\, \dfrac{d_{3,2}}{4}} = \frac{8}{3}\, \frac{\sigma_0\, d_{3,2}\, \dfrac{\varepsilon_0}{1-\varepsilon_0}}{\pi} \tag{39}$$

III.7 Direct measurement of particle properties to be used in

DEM

Some properties, which must be known to properly simulate the powder with DEM, were taken from the technical data sheet of the powder (Domo | Product Finder) such as the Young's modulus, or were found in the literature such as the Poisson's ratio (Weon, 2009) and the coefficient of restitution between the particles (Haeri, 2017), and are reported in Table III.3 and Table III.4. In these tables, also properties of the geometry have been reported. In particular, values of the Young's modulus and of the Poisson's ratio were taken from the literature (Lakes, 1987).

It has been assumed that coefficients of restitution between the particles and between the particles and the geometry are the same for both the normal and tangential direction.

A procedure similar to that described by Nan et al. (Nan *et al.*, 2018) was followed to evaluate the coefficient of sliding friction between the particles. A cube of the powder was obtained by cutting out a compressed disk of powder, formed with the mechanical tester Instron 5566. Then, the cube (Figure III.34a) was laid down over a different disk of compressed polyamide, which had been glued on a microscope slide. The slide was placed in such a way that one half was on a horizontal base and the other half was on a horizontal support which could be raised vertically. Therefore, by raising the support, the slide gradually inclined and the angle at which the cube started to slide was registered. The value of this angle, θ_S, corresponds to the angle of sliding friction. It is related to the coefficient of sliding friction, μ_S, (Teffo and Naudé, 2013) by the following relationship:

$$\mu_S = tan\,\theta_S \tag{40}$$
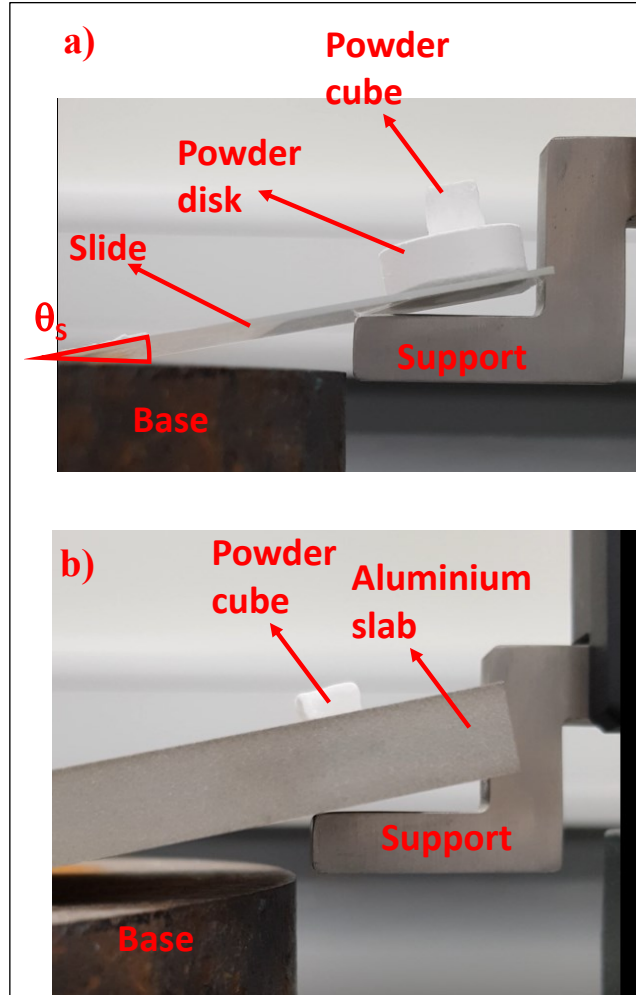
Figure III.34 *Measurement procedure of the coefficient of sliding friction: a) between the particles and b) between the particles and the geometry.*

In case of coefficient of sliding friction between the particles and the geometry, a similar procedure was adopted.

The cube was put on an aluminium slab (Figure III.34b), which was inclined to the angle at which the cube started to slide down. From the angle, the coefficient of sliding friction was calculated, according to eq. (40). The

slab is in aluminium because this material was used to simulate the geometries of the experimental setup for modelling of SLS spreading.

However, the powder spreading experiments were carried out with the final version of the setup, which has parts in stainless steel such as the blade and the deposition plate. This material differs from aluminium, which was the material of the parts of an initial version of the setup. But, with a view to future applications of the setup, such as tests at high temperatures and with higher compression pressures on the powder layer, it was necessary to design a new version with stainless steel parts. However, the properties of the geometries were measured by considering the aluminium as material and consequently this material was used to simulate the geometries well before the new setup was built. Except for the coefficient of sliding and rolling friction between the particles and the geometries, the other properties, which are related to the elastic properties of the geometries, do not affect the simulation results, given the low stresses involved on the deposition tray and on the blade.
Both the coefficients of sliding friction measured are reported in Table III.3.

The coefficient of sliding friction obtained with this procedure, are those that apply between the powder in bulk and the surface of the geometry or inside the powder over a shearing plane. Therefore, these coefficients may not coincide with the sliding friction over the surface between single particles or between single particles and geometry surfaces. Nevertheless, given the practical difficulty to determine the friction using small particles singularly on a surface to slide, the procedure was adopted as such.

Table III.3 *Properties inserted in the EDEM ™ model for the interaction between the particles and between the particles and the geometries made of aluminium: e_{P-P} and e_{P-G} are the coefficients of restitution between the particles and between the particles and the geometry, respectively; $\mu_{S,P-P}$ and $\mu_{S,P-G}$ are the coefficient of sliding friction between the particles and between the particles and the geometry, respectively. Regarding $\mu_{S,P-G}$ there are two columns: the first one reports the values of $\mu_{S,P-G}$ used in the unconfined yield strength (UYS) calibration; the second one reports the value of $\mu_{S,P-G}$ used in the static angle of repose (AOR) calibration, and which was measured as described in the text.*

Material	e_{P-P} (-)	e_{P-G} (-)	$\mu_{S,P-P}$ (-)	$\mu_{S,P-G}$ (UYS)	$\mu_{S,P-G}$ (AOR)
PA6	0.5 (Haeri, 2017)	0.5 (Haeri, 2017)	0.57	$1\cdot10^{-4}\div1$	0.33
Aluminium	-	0.5 (Haeri, 2017)	-	$1\cdot10^{-4}\div1$	0.33

Table III.4 *Properties inserted in the EDEM ™ model for the interaction between the particles and between the particles and the geometries made of aluminium: $\mu_{R,P-P}$ and $\mu_{R,P-G}$ are the coefficient of rolling friction between the particles and between the particles and the geometry, respectively; ν is the Poisson's ratio; E is the Young's Modulus. Values with references were taken from the literature, the other were taken from the technical data sheet of the powder or directly measured as described in the text.*

Material	$\mu_{R,P-P}$ (-)	$\mu_{R,P-G}$ (-)	ν (-)	E (GPa)
PA6	$1\cdot10^{-5} \div 1$	$1\cdot10^{-4} \div 1$	0.35	3.4
			(Weon, 2009)	
Aluminium	-	$1\cdot10^{-4} \div 1$	0.33	69
			(Lakes, 1987)	(Lakes, 1987)

Chapter IV
Modelling approach and validation

IV.1 Model tuning for the calibration procedures and the SLS
process

DEM modelling of the powder spreading in the SLS can be useful to gain an insight of the process, namely to investigate about the process conditions as well as the powder properties which are responsible for good or bad powder layer quality. For this purpose, the EDEM software was used.

By using the Hertz-Mindlin (no slip) with JKR cohesive model, which can be selected in the EDEM software, elastic deformation and adhesion between the contacting particles are taken into account. Therefore, it was assumed that no plastic deformation between the particles in the contact point is involved for the powder considered and that the considered energy dissipation at contacts takes place due to adhesion and viscoelastic deformation.

A model that does not account for the plastic deformation at contact points would be not adequate to completely describe the effects of powder consolidation. In fact, consolidation is mainly affected by two contributions. One is the increased number of contacts between the particles, the other is the increased strength of the binary forces between particles due to local plasticization of the contact point and the consequent increase of the surface of contact between particles. Several experimental results on the powder flow properties measured at increasing temperature have proven that the effect of temperature in the change of powder flow properties can be explained by introducing the plastic deformation of the contact that is affected by temperature which changes the particle material yield strength (Chirone *et al.*, 2016; Macrì *et al.*, 2017). A viscoelastic model can only rely on the first mechanism to describe powder consolidation and, in general, may not be

adequate for real powders. Nevertheless, in SLS application powder consolidation stresses are very low. Therefore, in the simulations of spreading of the powder at ambient temperature and without significant consolidation of the powder, e.g. when the vertical blade is used, as well as in the DEM calibrations the interparticle forces might be adequately accounted by a purely elastic model. This also means that in the simulations the value of compression force is only relevant to realize the correct number of interparticle contacts. The relatively independent value of the measured unconfined yield strength of the material with the consolidation stress (Figure IV.3) supports the hypothesis of purely elastic deformation of the particles at the contact points.

Since the number of these contacts are directly related to bed porosity, in the DEM calibration using the unconfined yield strength, which will be described in paragraph IV.5.2, the compression step was carried out at values of the compression stress that are able to provide values of the bed porosity similar to those experimentally found in SLS processes. In order to compare simulation results with experimental results, obtained with the shear tester on the powder, the experimental result obtained with this test was extrapolated to zero consolidation which is more relevant to the SLS process.

In the static angle of repose and in the unconfined yield strength calibration simulations, both described in paragraph IV.5, the Hertz Mindlin (no slip) model was used for the interaction between particles and the geometries. It means that no adhesive forces between the contacting bodies were considered.

In case of simulations of spreading of powder, the Hertz-Mindlin (no slip) with JKR cohesive model was used for the interaction between the particles and the geometries.
Value of the interfacial adhesive surface energy between the particles and the geometry (Γ_{P-G}) was inferred on the basis of data provided in a thesis found in the literature (Üzüm, 2015). Üzüm studied the multiscale adhesion behaviour and the service life expectancy of different metal/polymer hybrids, such as the aluminium/polyamide 6 hybrid. Üzüm measured Γ_{P-G}. Its value is 87.1 ± 7.4 mN/m. By using the data of Üzüm, the interfacial adhesive surface energy between the particles (Γ_{P-P}) was calculated. Its value is 85 mN/m. Therefore:

$$\frac{\Gamma_{P-G}}{\Gamma_{P-P}} = \frac{87.1}{85} = 1.025 \Rightarrow \Gamma_{P-G} = 1.025 \cdot \Gamma_{P-P} \tag{41}$$

Therefore, Γ_{P-G} was easily inferred once Γ_{P-P} was evaluated.

Moreover, due to the lack of data, the same value of $\mu_{R,P-P}$ was used for the coefficient of rolling friction between the particles and the geometry.

In all the simulations, spherical particles were used to simulate the powder rather than more complicated shapes in order to reduce the simulation time. From the SEM images (Figure III.1) it appears evident that the polymeric powder is constituted by particles with different and irregular shapes.

Initially, in the simulations for the DEM calibration, in order to replicate the actual shape of the particles, it was tried to model them as clumped spheres (Favier *et al.*, 1999a; Pasha *et al.*, 2016) i.e. each particle can be approximated by a number of overlapping spheres of different sizes (see Appendix C). But, by using this approach, the simulations were excessively long, even if the particles were modelled as two or three clumped spheres. This is due to two different reasons. One is the increase of the particles involved to simulate the powder. The second reason is that particles already in itself small were modelled with particles even smaller and, consequently, the simulation time greatly increased. In fact, the simulation time step is chosen as a fraction of the Rayleigh time step, that is the natural oscillation period of the mass-spring system made by the particle and the elastic contact (Marigo and Stitt, 2015). The Rayleigh time (Δt_R) depends on the particle diameter according to the following relationship:

$$\Delta t_R = \frac{\pi R \sqrt{\rho_p / G}}{0.1631\, \nu + 0.8766} \tag{42}$$

where R is the particle radius, ρ_p is the particle density, G is the shear modulus and ν is the Poisson's ratio of the particle.

Therefore, the smaller the spheres used to model the particles, the slower the simulation.

For this reasons, and given the shape of the particle size distribution (PSD) of the powder (Figure IV.2a), the experimental PSD was approximated to a purely Gaussian distribution (Figure IV.2b), centered in $D_{50} = 55$ μm, with a width $3\, \sigma_D$, such that:

$$3\, \sigma_D = D_{50} - D_{10} \tag{43}$$

By doing so, it is assumed that 99.97 % ($\approx$100 %) of the particles have a diameter between D_{10} and D_{90}. Therefore, particles smaller than D_{10} and bigger than D_{90} were cut out.

In Figure IV.2a, it is reported the experimental frequency PSD, based on the equivalent circle particle diameter (CE), as obtained with the Morphologi G3 (Malvern Panalytical Ltd., Malvern, UK). CE is the diameter of a circle with the same area as the 2D image of the particle.

From the graph of Figure IV.2a, 92.8 % of the particles have a diameter between D_{10} and D_{90}. In particular 1.75 % by volume of the particles have a diameter $< D_{10}$, while 5.4 % by volume of the particles have a diameter $> D_{90}$.

However, $D_{90} = 95$ μm is an average value between a range of values (80 ÷ 110 μm) provided in the data sheet of the polymeric powder. Therefore, if the upper limit of this range is considered, only 1.79 % of particles have diameter $> D_{90}$.
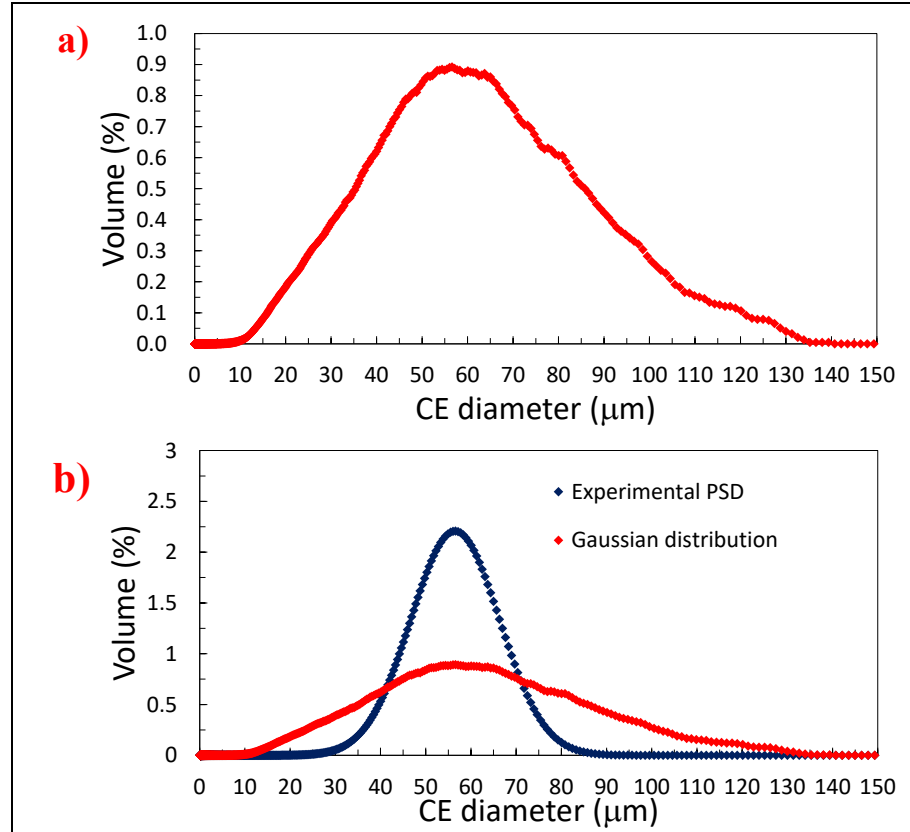
Figure IV.2 *a) Experimental frequency PSD; b) comparison between the experimental PSD (red rhombuses) and the Gaussian distribution (blue rhombuses)*

Hence, by using the Gaussian distribution almost all the particles of the powder are considered. However, even if both the Gaussian and the experimental particle size distributions are centered at D_{50}, the Gaussian distribution is narrower and more elongated than the actual particle size distribution (Figure IV.2b), due to the small value of the standard deviation. Therefore, by using the Gaussian distribution, a greater number of particles in the range $40 \div 72$ μm is considered, and a reduced number of particles is considered for diameters < 34 μm and >74 μm, thus committing some errors in the approximation. In table are reported the volumes, expressed as percentage of the total volume of particles having the diameter reported in the column on the far left. The errors, committed by using the Gaussian distribution, are expressed as percent errors, defined as follows:

$$Error\ (\%) = \frac{V_{Exp} - V_{Gauss}}{V_{Exp}} \times 100 \qquad (44)$$

Where V_{Exp} and V_{Gauss} are the total volume of particles with a diameter within a specific range of values by using the experimental PSD and the Gaussian distribution, respectively.

Table IV.1 *Total volume of particles with a diameter within a range of values, reported in the column on the far left, by considering the experimental PSD or the Gaussian distribution (Figure IV.2b). In the column on the far right it is reported the percent error, defined by eq. (44).*

Diameter (CE) (μm)	V_{Exp} (%)	V_{Gauss} (%)	Error (%)
< 34 μm	21.5	1.7	92
34 μm ≤ CE ≤ 74 μm	57.9	95.4	64.9
> 74 μm	20.6	2.9	85.8

Even if the approximation does not allow to reproduce accurately the particle size distribution, as demonstrated in Table IV.1, it allows not to slow down too much the simulations. Indeed, if particles smaller than D_{10} were considered, the time step would have been too small and the simulation time, would have been too long. Moreover, this representation of the PSD has allowed to properly reproduce the behavior of the PA6 powder in the powder spreading simulations, as it will be discussed in paragraph V.2.1.

IV.2 DEM calibration methods: introduction

The Bulk Calibration Approach was used to evaluate the coefficient of rolling friction between the particles and between the particles and the geometry.

The method which revealed to be the most appropriate consists of evaluating the coefficient of rolling friction by comparing the bulk density and the porosity of the powder layer both from the experiment and from the simulation. In particular, spreading of powder in the same conditions of the experiment was simulated. Then, different simulations were carried out in which the interfacial surface energy between the particles was set at the value evaluated as described in paragraph III.6 and the coefficient of rolling friction was changed in each simulation until a match between the bulk density and the porosity of the powder layer measured both from the experiment and from the simulation was found.

IV.3 Preliminary experimental tests for the calibration procedures

A Schulze ring shear tester RST-01.01, equipped with a S-cell (internal volume of the cell of 203.58 cm^3; external and internal annulus diameter of the lid of 118 and 62 mm, respectively) was used to shear test the powder and to derive:

- the flow function;
- the unconfined yield strength in condition of absence of consolidation, i.e. the major principal stress, σ_1, equal to zero. This value was used in the calibration procedure based on the simulation of the unconfined compression test, as will be described in the paragraph IV.5.2;
- the isostatic tensile strength of the unconsolidated material;
- the static angle of internal friction as function of σ_1;
- the angle (ϕ_{st}) described by the linearized dynamic yield locus;
- cohesion as function of σ_1.

Both the standard procedure recommended for the ring shear tester RST-01.01 and the ASTM-standard (ASTM D6773, 2002) were followed. Before the shear tests, the powder was placed in the oven for 1 hour at 100 °C to remove the humidity. Tests at consolidation stresses between 0.4 and 0.7 kg were carried out and 4-5 shear points were registered to obtain the corresponding yield locus. A software application, developed in the LabVIEW environment (National Instruments), was used to acquire, visualize, and record the main data, which were measured during the shear experiments. Moreover, the RSV 95 software version 2.1.0.1 for the RST-01.01 Schulze shear tester was used to derive all the previously listed properties.

Four different tests at different maximum loads (0.4; 0.5; 0.6 and 0.7 kg) were carried out with the shear tester. To verify the reproducibility of the measurements, each test was repeated 3 times. A value of f_c was measured for each value of σ_1. The average values of f_c, obtained from the repetition, have been reported in Figure IV.3, where the flow factors (FF= σ_1/f_c), which limit the Jenike flowability classes (Jenike, 1964), are reported as hyphenated lines. Data show that at ambient temperature and for $\sigma_1 > 1600$ Pa the powder is free flowing (FF > 10), while for $975 < \sigma_1 < 1600$ Pa, the polyamide 6 is easy flowing (4< FF <10). The good flowability of this polyamide is not surprising, being the powder specifically engineered for the SLS process. Significantly the variation of the unconfined yield strength is not very much affected by the compression stress. The unconfined yield strength was extrapolated at $\sigma_1 = 0$ Pa from the regression line (red hyphenated line in Figure IV.3). Its value is about 141 Pa.
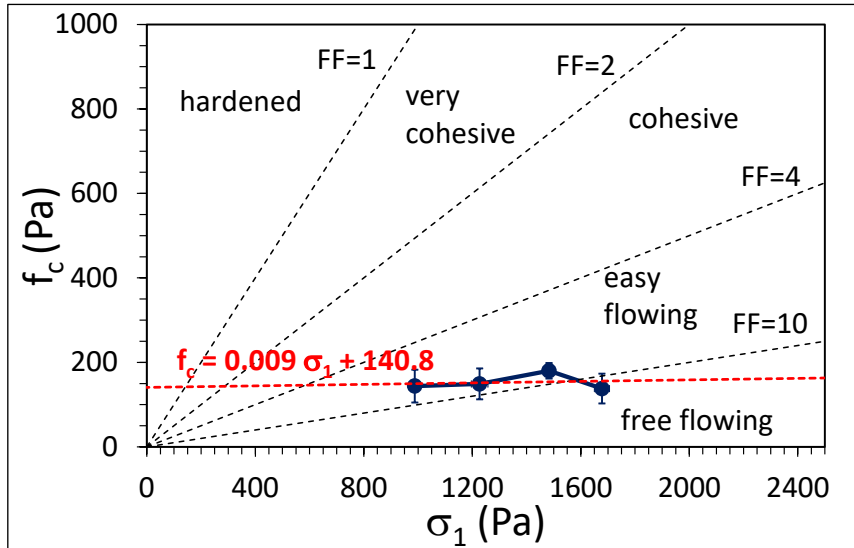
Figure IV.3 *Flow function for polyamide 6 and the corresponding regression line (red hyphenated line). FF (black hyphenated lines) is the flow factor.*

For the tested powder, the static angle of internal friction resulted to be almost independent of the powder consolidation (Figure IV.4a) and its average value was used in eq. (32) to get the isostatic tensile strength of the unconsolidated material (Table IV.2) and the angle described by the linearized dynamic yield locus (ϕ_{st}). In case of the alternative procedure, which has been explained in the paragraph III.5 for the calculation of σ_0 by following the geometry of the Static Yield Locus, values of the static angle of internal friction and of the cohesion at zero consolidation (C_0) were extrapolated from the intersection of the regression lines on the y-axis (Figure IV.4a and b).

The corresponding interparticle forces, calculated by adopting the Rumpf equation where $d_{3,2}$ (Table III.1) was measured by means of the Morphology G3 (Malvern Panalytical), are reported in Table IV.2. From these values of the force, a value of the interfacial surface energy between the particles (Table IV.2) was calculated by using the eq. (39). Therefore, a range for the interfacial energy was found. The actual value of the energy should be within this range. Consequently, two different values of the Bo number were obtained and from them a corresponding agglomerate diameter (Table IV.3) was calculated according to eq. (36).
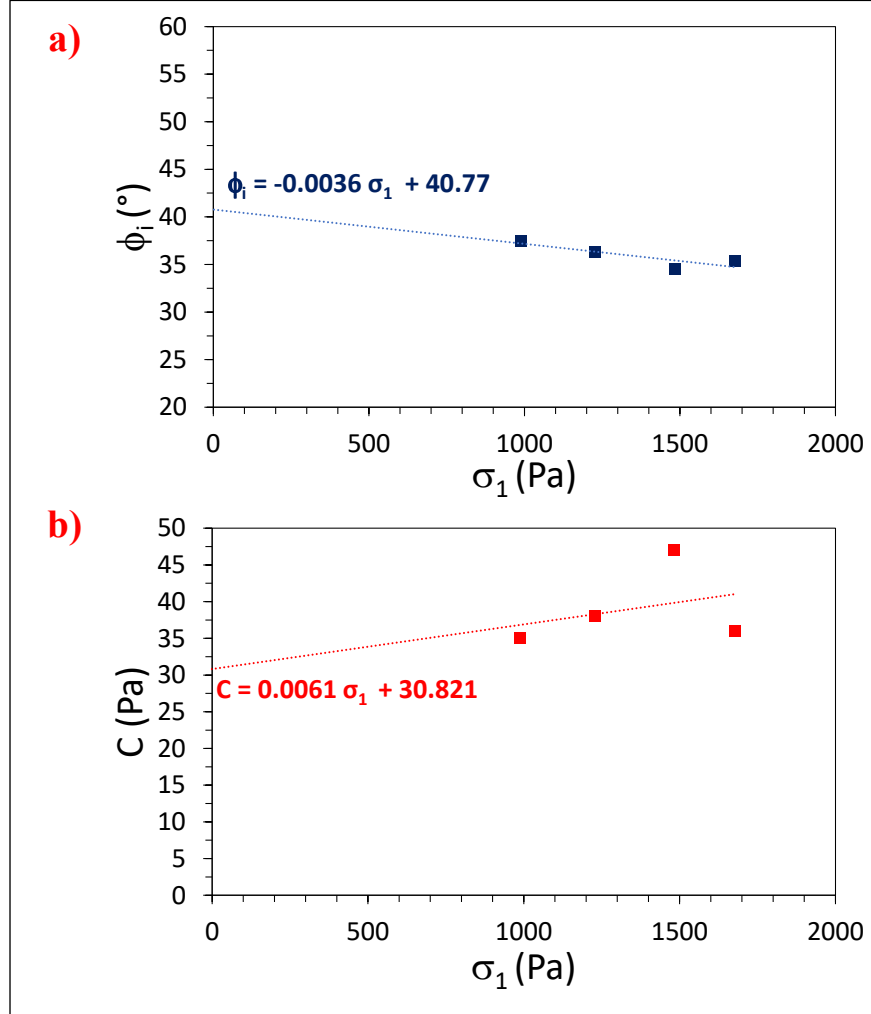
Figure IV.4 *Static angle of internal friction (ϕ_i) and cohesion (C) of PA6 as function of the major principal stress (σ_1).*

Table IV.2 *Evaluation of the interfacial surface energy between the particles from eq. (39). ϕ_{st} is the angle described by the linearized dynamic yield locus, $\sigma_{0,1}$ and $\sigma_{0,2}$ are the isostatic tensile strength of the unconsolidated material, evaluated according the eqs. (32) and (33), respectively; ε_0 is the powder voidage calculated from the powder bulk density, estimated for the unconsolidated material, ϕ_{i0} is the static angle of internal friction at zero consolidation; C_0 is the powder cohesion at zero consolidation; $F_{int,1}$ and $F_{int,2}$ are the interparticle forces calculated from the Rumpf equation by using $\sigma_{0,1}$ and $\sigma_{0,2}$, respectively; $\Gamma_{P-P,1}$ and $\Gamma_{P-P,2}$*

are the interfacial surface energy between the particles obtained from eq. (39) and $F_{int,1}$ and from $F_{int,2}$, respectively

ϕ_{st} (°)	$\sigma_{0,1}$ (Pa)	ε_0 (-)	$F_{int,1}$ (nN)	ϕ_{i0} (°)	C_0 (Pa)	$\sigma_{0,2}$ (Pa)	$F_{int,2}$ (nN)	$\Gamma_{P-P,1}$ (mJ m^{-2})	$\Gamma_{P-P,2}$ (mJ m^{-2})
36	49	0.54	107	41	31	36	77	2.2	1.5

Table IV.3 *Values of the Bo number and the corresponding agglomerate diameters obtained by using the two values of the interparticle forces of Table IV.2.*

Bo_1 (-)	$D_{a,1}$ (μm)	Bo_2 (-)	$D_{a,2}$ (μm)
110	263	79.1	236

IV.4 Determination of coefficient of rolling friction

IV.4.1 Method

Altair EDEM was used to simulate spreading of powders in the same conditions of the experimental setup. In the simulation, two different trays are replicated (Figure IV.5a). The deposition tray (T2), is located lower with respect to the other one (T1) so as to have a gap which is identical to the depth of the deposition tray of the experimental setup, that is 300 μm. A blade, with the same geometry like the one used for the experimental tests, is positioned just after the gap between T1 and T2. In doing so, the period of blade advancement above T1 until reaching T2 is saved and the simulation time is consequently reduced. As in the experiments, the blade is positioned with the flat side of the tip facing the powder heap (Figure IV.5a).

The simulation domain (Figure IV.5b) has a width (y direction) of 10 times D_{90}, while the height (z direction) and the length (x direction) of the domain are changed during the simulation in order to include all the particles, minimise the number of grid cells and consequently the simulation time, as suggested in the user guide of EDEM. Width of the powder layer and consequently of the domain have been chosen as a compromise between a distance which should be sufficiently large as not to affect the particle dynamics and not too large as not to slow down the simulation time. Indeed, the larger the simulated layer, the more the particles to be generated and consequently the longer the computational time.

The domain is divided in grid cells, where contact detection between particles takes place. The cell size has been set at 4 R_{min}, where R_{min} is the minimum particle radius in the simulation.
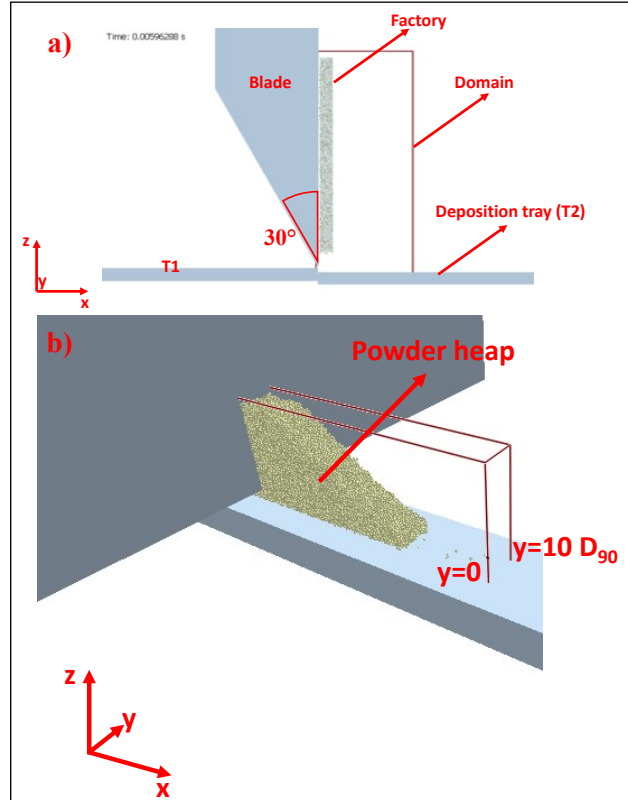
Figure IV.5 *a) Powder creation from a dynamic factory. T2 is the deposition plate; b) Simulation domain.*

The front and rear boundaries of the domain (i.e. $y = 0$ and $y = 10 \cdot D_{90}$ planes) are treated as Linear Periodic Boundaries for particle flow. This means that any particle leaving the domain in correspondence of the boundaries instantly re-enters it on the opposite side. For example, a particle which leaves the domain in correspondence of $y = 0$, enters again the domain at $y = 10 \cdot D_{90}$.

Moreover, each particle on the border of the domain interacts with material on the other side of the boundary. Periodic boundaries have been used because it is assumed that the behaviour of powder inside the domain is approximately the same one that the powder experiences in reality away from the walls of the deposition tray. In this way the wall effects are neglected.

The material properties of PA6 powder used in the simulation are those reported in Table III.1. Values of coefficients of restitution between the particles and between the particles and the geometries, coefficient of sliding friction between the particles, the Poisson's ratio and the Young's Modulus of

both the powder and the geometries, which were used in the simulations, are those reported in Table III.3 and Table III.4. The coefficient of sliding friction between the particles and the geometries, which was used, is equal to 0.33. This value was obtained according to the procedure described in the paragraph III.7.

The powder bed is generated within a dynamic factory (Figure IV.5a), where particles with the particle size distribution and shape such as those described in paragraph IV.1, are generated at random. Once created, the particles fall on T2 where they accumulate to form the powder heap (Figure IV.5b).

The factory is a box with a length of 10^{-3} m, a width of $9.5 \cdot 10^{-4}$ m and a height of $1.5 \cdot 10^{-2}$ m. The total mass of powder generated is $1.45 \cdot 10^{-6}$ kg. This quantity has been chosen in order to complete a powder layer with a length of $1.5 \cdot 10^{-2}$ m, a width of $9.5 \cdot 10^{-4}$ m (that is $10 \cdot D_{90}$) and a height of $300 \cdot 10^{-6}$ m, that is the layer thickness.

To calculate the total mass, a different simulation was run. In particular, a static factory with the same dimensions of the powder layer has been created on a plate (Figure IV.6). Static means that the factory creates the particles instantaneously. To minimize the void fraction within the static factory and consequently to calculate the mass (to be created within the dynamic factory) which would guarantee the completion of the powder layer in case of perfect deposition of the powder during the spreading, only particles with a diameter equal to D_{10} have been created in the static factory. In fact, in principle, the smaller the particle diameter the lower the void fraction within the factory. i.e. the denser the powder bed.
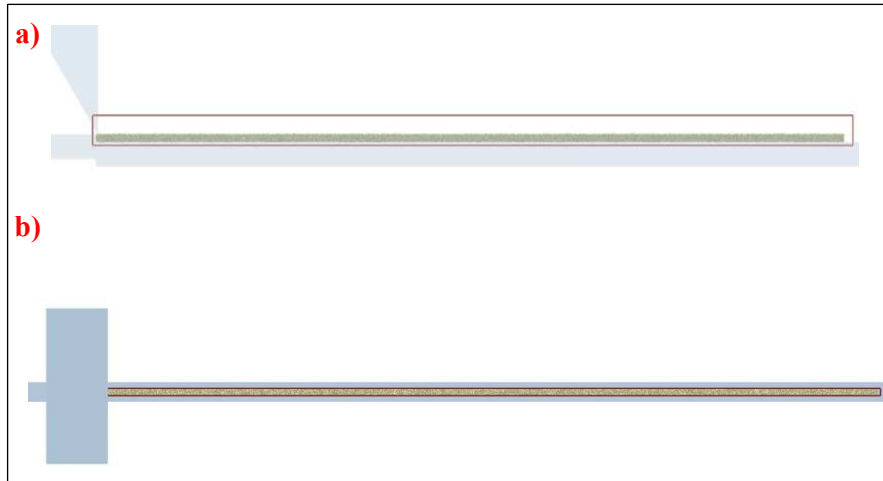
Figure IV.6 *a) Front and b) top view of the static factory for the calculation of the total mass of the powder to be created in the dynamic factory.*

Once the powder heap, created by the dynamic factory, is stabilised, that is all the particles are stopped, the blade is moved forward, i.e. along the x-direction, at a fixed scrolling velocity (Figure IV.7).
The spreading process continues until the particle layer is obtained.
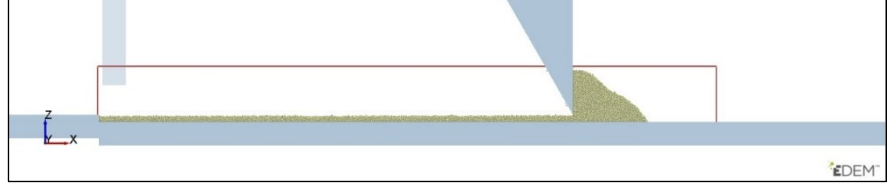
Figure IV.7 *Spreading of the powder with EDEM.*

Three different simulations were carried out. They differ for the coefficient of rolling friction between the particles. The values which were tried are: 0.1, 0.19 and 0.3.
The interfacial surface energy between the particles was set to 1.9 mJ m^{-2}, that is the average value between the extremes of the range $1.5 < \Gamma_{P-P} < 2.2$ mJ m^{-2} (Table IV.2).
Therefore, by applying eq. (41) the interfacial surface energy between the particles and the geometries was set to 1.95 mJ m^{-2}.
To find the correct value of coefficient of rolling friction, two properties were measured and compared with the ones obtained with the experiments: bulk density and porosity of the powder layer (Figure IV.8). Simulation and experiments were carried out at the same scrolling velocity of the blade, i.e. 3 cm s^{-1}.
6 different experiments were carried out by using the deposition plate with trays 300 μm deep. Powder deposited in the deposition tray was removed and collected in a vial. Weight of the collected powder was measured. Since the tray has a length and a width of $10 \cdot 10^{-2}$ m and a height of 300 μm, it was possible to calculate the bulk density ($\rho_{b,exp}$) as the mass of the collected powder in the tray divided by the tray volume.
Experimental bulk density resulted to be 261 ± 18 kg m^{-3}. Porosity (ε_{exp}) was calculated as follows:

$$\varepsilon_{exp} = \frac{V_{total} - V_{ps}}{V_{total}} \tag{45}$$

where V_{total} is the sum of the volume of particles (V_{ps}) and the volume of voids within the powder layer. V_{ps} is given by the ratio between the mass of the collected powder divided by the particle density. ε_{exp} resulted to be 0.77 ± 0.016. Variation in the measurements was calculated as the standard deviation.
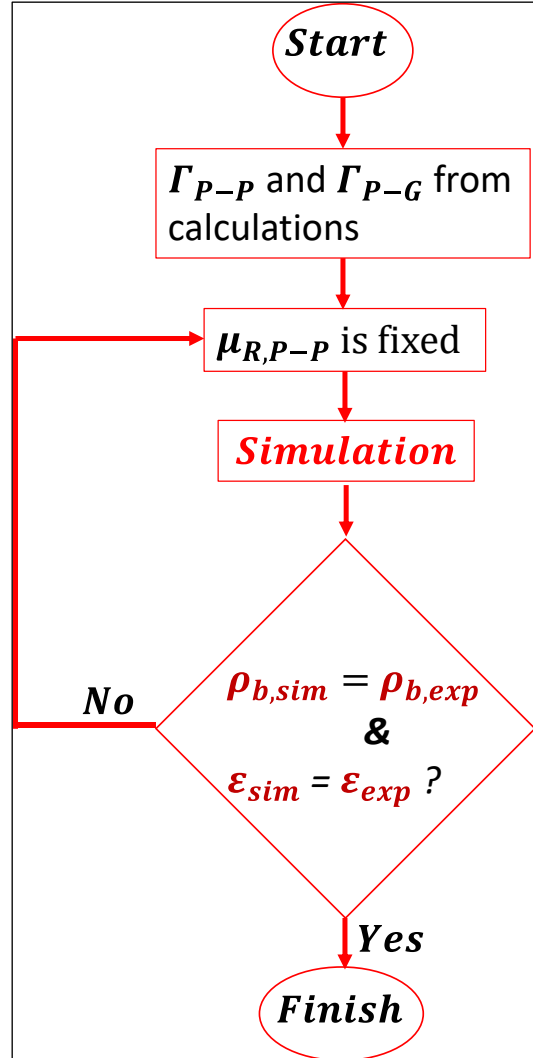
Figure IV.8 *Schematic of the coefficient of rolling friction calibration methodology in a flow chart.*

In case of simulation, the bulk density ($\rho_{b,sim}$) and the porosity (ε_{sim}) were measured in 6 different geometry bins, namely virtual boxes with a length of $2.5 \cdot 10^{-3}$ m, a width and a thickness like those of the powder layer, namely $95 \cdot 10^{-5}$ m and $300 \cdot 10^{-6}$ m, respectively. The bins were set in sequence (Figure IV.9) so as to include the whole powder layer. By doing so it was possible to measure powder properties in different positions of the powder layer. Average values of $\rho_{b,sim}$ and ε_{sim} between those measured in the 6 bins were

considered. Variation in the measurements was calculated as the standard deviation.
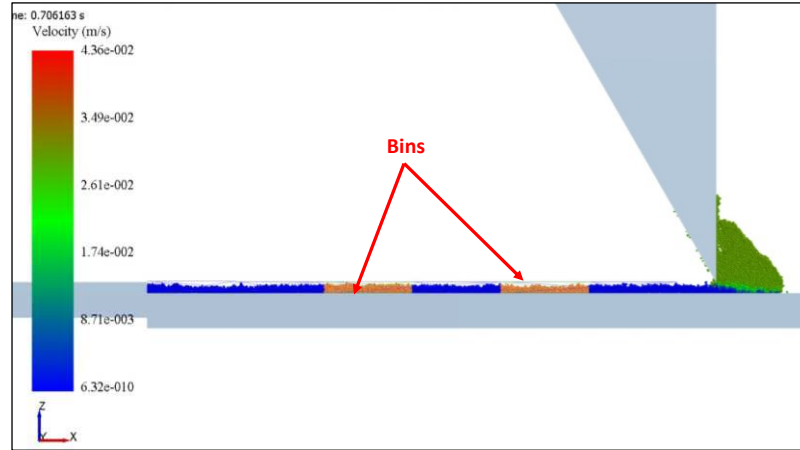
Figure IV.9 *Geometry bins used to measure the bulk density and the porosity in different points of the powder layer.*

Bulk density and porosity of powder depend on the particle shape, which has not been considered in the simulation. Therefore, it could be argued that the measured values of density and porosity are valid only in case the actual shape of the particle is spherical. In fact, usually the more irregular the shape of particles, the less the bulk density. Therefore, spherical particles would provide higher bulk densities (and less porosity) than irregular shape particles, like those of the PA6 powder, for the same size of particles (Riley and Mann, 1972; Abdullah and Geldart, 1999).

There are two common approaches to consider the effect of shape on the powder behaviour in DEM simulations. One approach consists of calibrating the coefficient of rolling friction between the particles, which are all spherical, by comparing an experimental data with the one obtained from the simulation, e.g. the angle of repose (Wensrich and Katterfeld, 2012; Alizadeh *et al.*, 2017; Behjani *et al.*, 2017). The other approach, which has been mentioned in paragraph IV.1, consists of simulating the particle shape, for example by clumping spheres together (clumped sphere approach) (Favier *et al.*, 1999b). In each simulation, a different number of clumped spheres are used while the coefficient of rolling friction between the particles is maintained very low so as to minimise the effect of rolling friction between the particles. The optimal number of spheres is found once the experimental data is equal to the one obtained from the simulation. Even if this second method is more rigorous, has the limit to be computationally expensive and turns out to be unsuitable, unless very powerful computers are used.

However, this latter approach was originally tried in the simulations for calibration of the DEM model parameters (see Appendix C) but the simulation time dramatically increased because of the size of the smallest spheres, which

92

has an effect on the time step (for the resolution of the translational and rotational motion equations), and because of the increase of the number of particles in the simulation. For example, 5 particles, represented as clumped spheres, corresponded to a total number of spheres in the simulation between 15 and 60. Even if only two spheres were used to simulate the particles, thus reducing the accuracy in the representation of particles, simulations were still too slow. Therefore, the clumped sphere approach, for the case of the polyamide 6 powder, seems to be not suitable due to the too small dimension of particles with D_{50} of 55 μm, unless very powerful computers are used. For this reason, spherical particles have been considered and the approach, based on the calibration of the coefficient of rolling friction, has been used.

IV.4.2 Results

A time step of 40 % of critical Rayleigh time was used for each simulation, whose duration resulted to be 1 week.
Comparison (Table IV.4) between the results obtained from the simulations and from the experiments shows a good match in case of $\mu_{R,P-P} = \mu_{R,P-G} = 0.19$. Therefore, this value was used in the simulations of spreading of powder with the purpose of validating the DEM model, as will be described in paragraph IV.6.

Table IV.4 Comparison between experiments (exp) and simulations (sim) in terms of bulk density (ρ_b) and porosity (ε) of the powder layer in order to find the proper coefficient of rolling friction between the particles ($\mu_{R,P-P}$) for the same interfacial adhesive surface energy between the particles (Γ_{P-P}) and between the particles and the geometries (Γ_{P-G}).

Γ_{P-P} (J m^{-2})	Γ_{P-G} (J m^{-2})	$\mu_{R,P-P}$ (-)	$\rho_{b,sim}$ (kg m^{-3})	$\rho_{b,exp}$ (kg m^{-3})	ε_{sim} (-)	ε_{exp} (-)
0.0019	0.00195	0.1	368 ± 10	261 ± 18	0.67	0.77 ± 0.016
0.0019	0.00195	0.19	263 ± 22	261 ± 18	0.77	0.77 ± 0.016
0.0019	0.00195	0.3	167 ± 47	261 ± 18	0.85	0.77 ± 0.016

IV.5 Other attempts of calibration procedures

The main objective of the other two calibration procedures was to find a value of the interfacial adhesive surface energy and of the coefficient of rolling friction between the particles. One is based on the match of the static angle of repose estimated with the formation of a powder heap as obtained on both

experiments and model simulations. The other relies on the comparison between the unconfined yield strength experimentally measured with a shear testing procedure and the unconfined yield strength calculated from an idealized uniaxial testing model simulation. Each of the two calibration methods provided an independent set of couples of values of the model interfacial adhesive surface energy and of the coefficient of rolling friction between the particles able to satisfactorily describe the experiments with the model. The scope was to verify whether it was possible to use these two independent sets to find at least a single couple of values of the model surface energy and of the coefficient of rolling friction between the particles to be used in both model simulation procedures to satisfactorily describe all the experimental results.

IV.5.1 DEM calibration using the static angle of repose

IV.5.1.1 *Preliminary experimental test for the static angle of repose*

calibration method

The static angle of repose (α) of the powder was measured by letting the powder flow out from a hopper and then by collecting it over a circular lid (Figure IV.10) until a stable heap is obtained. The value of the angle was measured by using the ImageJ software. Before measuring the static angle of repose, the powder was placed in the oven for 1 hour at 100 °C to remove the humidity.
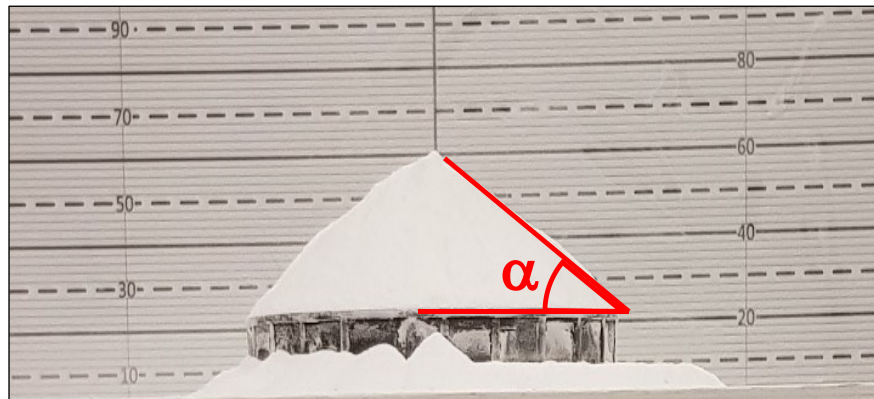
Figure IV.10 *Experimental measurement of the static angle of repose.*

IV.5.1.2 *Method*

Simulation of the static angle of repose resembles the experimental procedure, presented in paragraph IV.5.1.1. A dynamic factory, whose

geometry is a circular plane, is inserted in a hopper (Figure IV.11) with the aim of creating particles in a random way. The particles fall through the hole of the hopper and then on a layer of particles of the same powder. When a clearly visible heap is obtained, the creation of the particles is interrupted within the factory. The angle of repose is measured once the particles are all steady. The hopper is a truncated cone. The radii of the bases are 100 and 400 μm while the height of the cone is 1 mm. The properties of the powder and of the geometries, which were used, are those reported in Table III.1, Table III.3 and Table III.4.
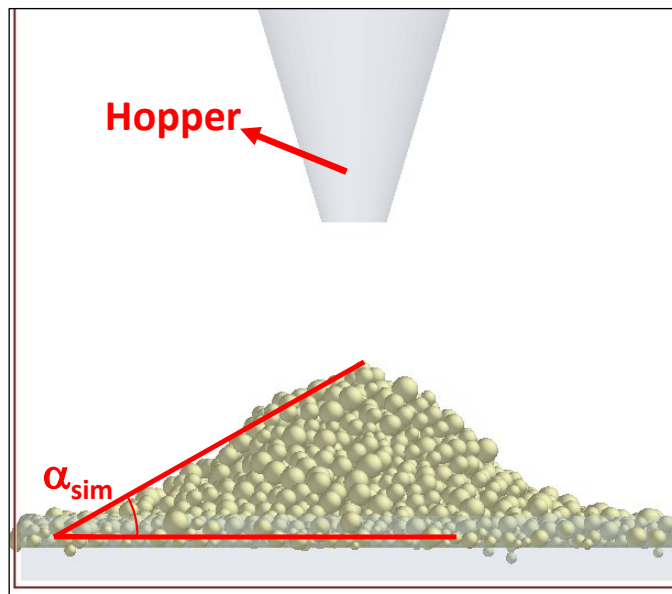
Figure IV.11 *Formation of the powder heap in the simulation for the calibration of the interfacial adhesive surface energy and of the coefficient of rolling friction between the particles. α_{sim} is the static angle of repose from the simulation.*

In the case of the simulation of the angle of repose, the simulation time was of about 8 hours with a time step of 40 %.

IV.5.1.3 *Results*

The static angle of repose was measured with the setup and by following the procedure described in paragraph IV.5.1.1 using 6 repetitions was 36.96° ± 2.5°, where the deviation reported is the standard deviation of results. Different simulations were carried out to reproduce the formation of the heap and to evaluate the corresponding static angle of repose (α_{sim}) by choosing a

time step of 40 % of critical Rayleigh time step. Indeed, this time step guarantees the same value of the angle, which can be obtained with a lower percentage value, e.g. 20 %. Five different values of Γ_{P-P} were chosen in the range between 10^{-5} and 10^{-2} J m^{-2}. For each value of Γ_{P-P}, different values of the coefficient of rolling friction between the particles were used ranging between 10^{-5} and 0.8. The aim was to find the pairs of the parameters for which the experimental static angle of repose is matched by the one obtained by the simulations (Figure IV.12).
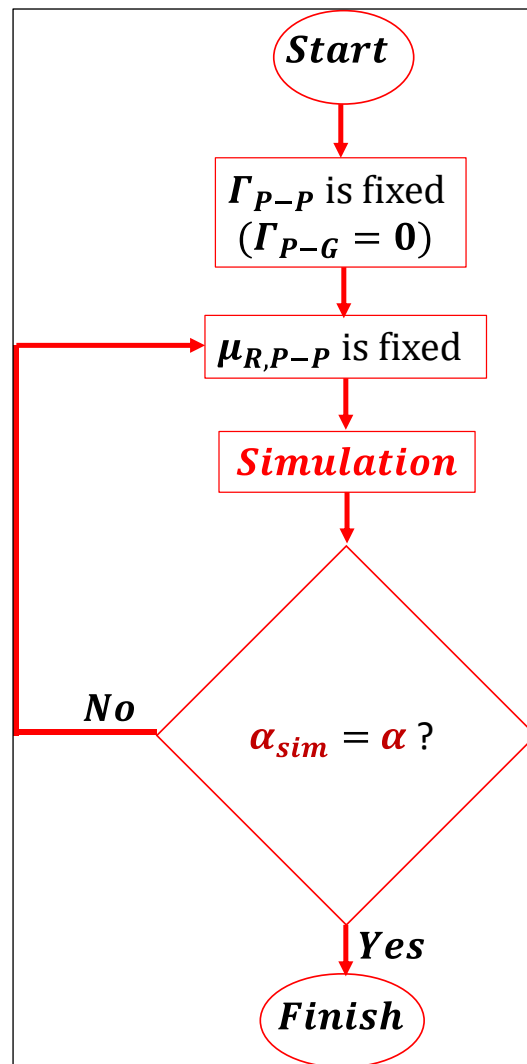
Figure IV.12 *Schematic of the static angle of repose calibration methodology in a flow chart.*

Results are reported in Figure IV.13 where the value of angle of repose resulting from simulation is plotted as a function of the interfacial adhesive surface energy and the coefficient of rolling friction between the particles. Since the value of α_{sim} is estimated with a visual procedure the simulation result is subject to a certain variation represented by error bars. Points corresponding to the same Γ_{P-P} are plotted using the same symbol. In the figure, the experimental value of the angle of repose is reported as a continuous red horizontal line. The two parallel red hyphenated lines represent the standard deviation of the measured value obtained by experiment repetitions. Figure IV.13 also reports interpolating polynomial for each set of data at similar Γ_{P-P}. Intersections of these polynomials with the horizontal line representing the experimental α help to find couples ($\mu_{R,P-P}$, Γ_{P-P}) able to predict the correct value of the angle of repose. To verify the reliability of the results, new simulations were carried out by setting the parameters for the four couples ($\mu_{R,P-P}$, Γ_{P-P}) found with the procedure above. Resulting values of α are reported in Table IV.5 which shows that the procedure is fairly adequate.
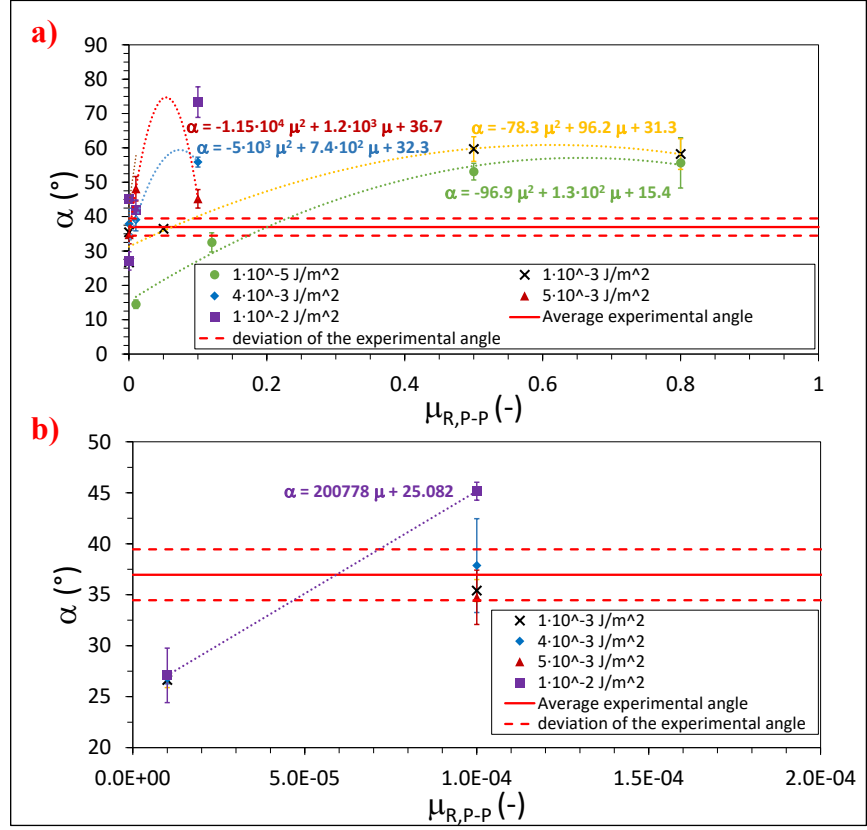
Figure IV.13 *a) Static angle of repose (α) as function of the coefficient of rolling friction between the particles ($\mu_{R,P-P}$) for different values of the interfacial adhesive surface energy between the particles (Γ_{P-P}): •, $1\cdot10^{-5}$ J m^{-2}; ×, $1\cdot10^{-3}$ J m^{-2}; ◆, $4\cdot10^{-3}$ J m^{-2}; ▲, $5\cdot10^{-3}$ J m^{-2}; ■, $1\cdot10^{-2}$ J m^{-2}. Dotted lines using the same colours of simulation results are the interpolating polynomials for resulting α at constant Γ. The continuous red line and red hyphenated lines correspond to the experimental average value of α and its standard deviation range, respectively; b) zoom of data in the range 0 ÷ $1\cdot10^{-4}$ with the regression line in case of $\Gamma_{P-P}=1\cdot10^{-2}$ J m^{-2}.*

Table IV.5 *Comparison between the predicted α (α from the polynomial) and the one obtained from the simulations (α_{sim}) for the reported pairs of the parameters (Γ_{P-P} and $\mu_{R,P-P}$) to verify the reliability of the prediction. $\sigma_{\alpha,sim}$ is the standard deviation of α_{sim}.*

Γ_{P-P}	$\mu_{R,P-P}$	α from the polynomial	α_{sim}	$\sigma_{\alpha,sim}$
(J m^{-2})	(-)	(°)	(°)	(°)
$1 \cdot 10^{-5}$	$2 \cdot 10^{-1}$	36.96	39.36	5.90
$1 \cdot 10^{-3}$	$6.2 \cdot 10^{-2}$	36.96	36.09	2.16
$4 \cdot 10^{-3}$	$6.7 \cdot 10^{-3}$	36.96	35.75	0.30
$5 \cdot 10^{-3}$	$2.2 \cdot 10^{-4}$	36.96	41.02	0.10

Figure IV.14 reports the couple of the parameters ($\mu_{R,P-P}$, Γ_{P-P}) represented as red circles on a plane. The best interpolating function for points in this plot is a logarithmic function:

$$\mu_{R,P-P} = -0.032 * ln\,\Gamma_{P-P} - 0.167 \tag{46}$$
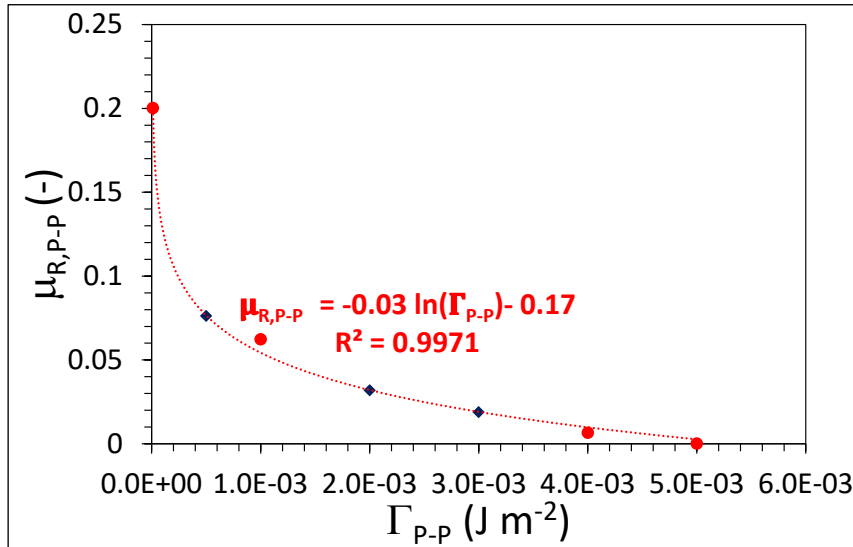
Figure IV.14 *Logarithmic curve representing all the possible pairs of the parameters ($\mu_{R,P-P}$ and Γ_{P-P}) for which α from the simulation (α_{sim}) is matched by the experimental one.*

To verify the reliability of the equation, three other pairs of the parameters from the curve in the same range of Γ_{P-P} and $\mu_{R,P-P}$, reported as blue diamonds in Figure IV.14, were chosen. By using these pairs, the value obtained of α from the simulation is very close to the experimental one (Table IV.6). This proves that all the pairs of the logarithmic curve are all possible candidates.

Table IV.6 *Pairs of parameters (Γ_{P-P} and $\mu_{R,P-P}$) from the logarithmic curve for which the experimental α and that obtained from the simulation (α_{sim}) are matched. $\sigma_{\alpha,sim}$ is the standard deviation of α from the simulation.*

Γ_{P-P}	$\mu_{R,P-P}$	Experimental α	α_{sim}	$\sigma_{\alpha,sim}$
(J m^{-2})	(-)	(°)	(°)	(°)
$2 \cdot 10^{-3}$	$3.2 \cdot 10^{-2}$	36.96	38.63	0.05
$3 \cdot 10^{-3}$	$1.9 \cdot 10^{-2}$	36.96	39.18	2.33
$5 \cdot 10^{-4}$	$7.6 \cdot 10^{-2}$	36.96	39.39	0.78

In case of $\Gamma_{P-P} = 1 \cdot 10^{-2}$ J m^{-2}, represented in Figure IV.13b, a regression line between the points representing α at $\mu_{R,P-P} = 10^{-4}$ and at $\mu_{R,P-P} = 10^{-5}$ was considered to have a best estimation of the coefficient of rolling friction. From the line, a value of $\mu_{R,P-P} = 5.92 \cdot 10^{-5}$ was obtained. Repeating the simulation with this value of $\mu_{R,P-P}$, the resulting static angle of repose is 42.6 ± 1.6, which is somewhat higher than the experimental angle, compared to the other values of α obtained from the simulations with the other pairs of parameters of Table IV.5 and Table IV.6. Therefore, it is better to consider values of Γ_{P-P} between $1 \cdot 10^{-5}$ and $5 \cdot 10^{-3}$ J m^{-2} as possible candidates.

IV.5.2 DEM calibration using the unconfined yield strength

IV.5.2.1 Method

There are two methods to measure the unconfined yield strength of a cohesive powder subject to compression (Barletta, Poletto and Santomaso, 2019). The simplest is to use a uniaxial tester in which the powder is inserted in a cylindrical mold. The powder is compressed with a piston lid to a defined consolidation stress, then the compression force is released, the mold is open in order to free the agglomerated powder sample. If the compression force is sufficiently high the compressed powder sample is compacted and is able to keep the shape of the cylindrical mold. Then the piston lid is lowered again and the force necessary to break the cylindrical sample is measured. The ratio

between this force and the agglomerate cross section is the unconfined yield strength of the material, which is a function of the normal stress in the compression step. Unfortunately in this procedure it is very difficult to avoid the effect of the wall shear stress on the sample, reducing the effective compression force at the bottom of the sample (Parrella *et al.*, 2008), unless complex devices are used. For this reason, a second method is more often followed and the unconfined yield strength is indirectly measured from shear testing experiments (Ruggi, Lupo, *et al.*, 2020). It is assumed that the major principal stress obtained from the Mohr circle describing the stress state during shear testing consolidation coincides with the consolidation stress in the uniaxial test and that the yield condition in the uniaxial tester is represented by the Mohr circle passing through the origin of the $\tau - \sigma$ plane and tangent to the static yield locus obtained with the shear tester at the same consolidation condition. This latter procedure was used to calculate the flow function of the material, that is the unconfined yield strength as a function of the major principal stress at consolidation.

Previous studies in literature indicate that the powder flow properties evaluated with a shear cell are not directly comparable with those obtained with a uniaxial compaction tester due to different stress state conditions achieved in the two testers, unless specific procedures are used (Parrella *et al.*, 2008). However, the model used by Parrella et al. has demonstrated that the results obtained with the two testers in terms of unconfined yield strength can be comparable, especially at low consolidation stresses. In fact, the differences of the measured values are strongly reduced if the state stress of the powder sample in the uniaxial compression test experiments is recalculated, taking into account the mould wall friction and the powder weight. A similar procedure has been carried out to calibrate the DEM parameters using the unconfined yield strength (UYS).

Simulation of the shear testing procedure is quite cumbersome with the DEM procedure, due to the length of the test, the number of particles to be used and complexity of the shear tester geometry. On the other hand, by using a virtual experiment in DEM it is possible to very easily get rid of wall friction and therefore an idealized uniaxial testing procedure was used to calibrate unknown DEM parameters and compare the obtained unconfined yield strength (UYS) so calculated with the value indirectly measured in shear testing experiments (Figure IV.15).

In particular, the measured UYS has been extrapolated at a consolidation stress equal to 0 from the shear cell experiments. By doing so, the UYS has been evaluated in stress state conditions as close as possible to the spreading process where consolidation is very low. The UYS has been also calculated with a simulation reproducing the unconfined compression test but with some important differences: the wall friction and the weight of the powder have been eliminated. If these effects are eliminated, the two procedures (shear tester and unconfined compaction tester) should provide the same results for

the same consolidation stress. In the case of PA6, the UYS is almost constant with the consolidation stress (Figure IV.3), even for low values of the major principal stresses. Therefore, the assumption of extrapolating UYS at a consolidation equal to 0 Pa (not far from the minimum consolidation stress for which a value of UYS has been measured with the shear cell, i.e. 988 Pa) seems to be reasonable. A consolidation stress equal to zero should be almost the same experienced by the powder in the spreading process, at least when a vertical blade is used.
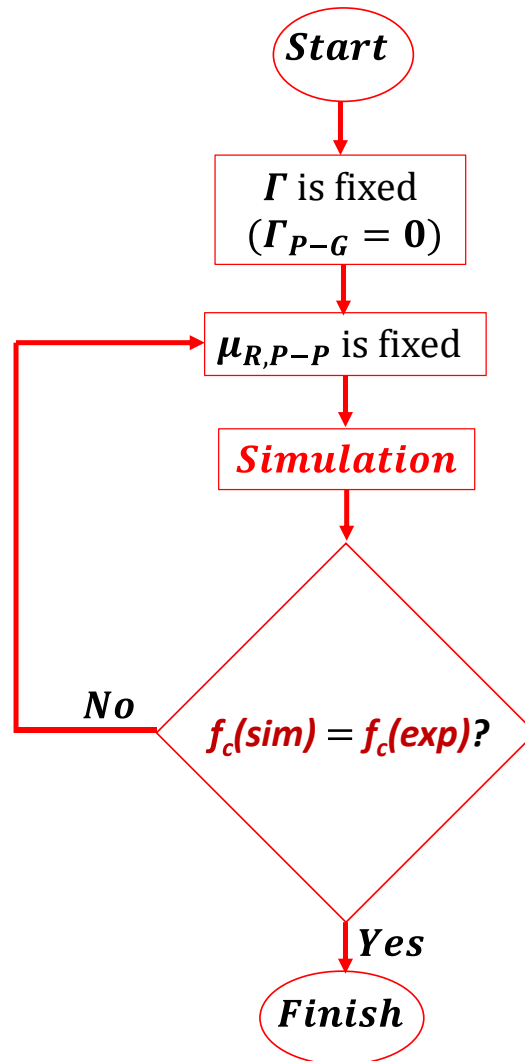
Figure IV.15 *Schematic of the unconfined yield strength calibration methodology in a flow chart.*

In the simulation, the geometry is the one represented in Figure IV.16a. The mold is made by a flat base and two hemicylindrical walls that are kept

102

fixed on the base during the compression step and removed during the yield step. In order to eliminate wall shear stress the coefficient of sliding friction and the coefficient of rolling friction between the particles and the wall are put to a very low value (10^{-4}) in the compression step. This idealized approach makes the size of the sample less significant. So, in order to minimize the number of particles used in the experiment the diameter of the mold is set to 0.5 mm and the mold height to around 1.5 mm, that is three times the mold diameter. The simulation consists of 4 steps (Figure IV.16): a) generation of the powder bed inside the mold; b) compaction of the bed with a circular piston lid to achieve the desired consolidation stress c) raising of the lid to zero out the force exerted by the lid on the powder bed; d) unconfined compression of the powder bed by means of the lid.

The powder bed is created by a static factory within the mold (Figure IV.16a). This factory allows to create particles with a random arrangement instantly. The total mass of the powder bed used is $1.4 \cdot 10^{-7}$ kg. Properties of the powder or regarding the interaction between the particles and the geometries, which have been used in the simulation, are reported in Table III.1, Table III.3 and Table III.4.
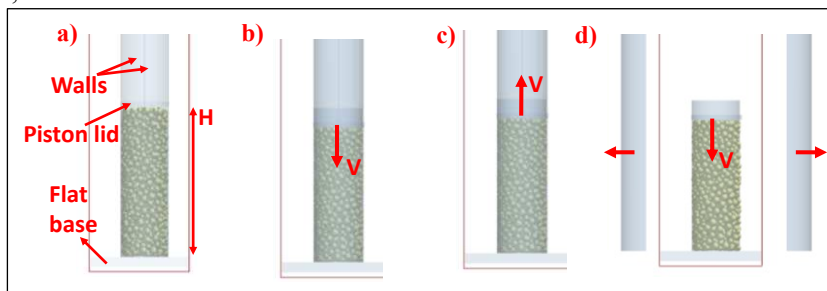
Figure IV.16 *Steps of the simulation: a) generation of the powder bed; b) compaction of the bed with the lid; c) relaxation of the bed; d) unconfined compression with the lid. H is the initial height of the powder bed; V is the scrolling velocity of the circular piston lid. The red arrows indicate the direction of movement of the geometrical elements*

In order to avoid the effect of powder weight on the stress acting at the bottom of the sample, simulations have been carried out by setting the acceleration due to the gravity equal to 0 m s^{-2}.

The general rule for the implementation of the model is that the time step should be between 10 and 40 % of critical Rayleigh time step (Marigo and Stitt, 2015), as suggested in the EDEM ™ 2019.2 documentation. For these simulations, time steps of 20 and 40 % of the critical time step have been used to verify the reliability of the measured unconfined yield strength. Once the bed is created in the cylindrical factory, a piston lid (Figure IV.16b) with the same diameter of the powder bed compacts the bed going down at a scrolling

velocity, V, of 0.005 m s^{-1}. To guarantee roughly the same initial void fraction of the polymeric powder in all the simulations and to evaluate the unconfined yield strength in correspondence of a major principal stress close to 0 Pa, the lid is stopped when the consolidation stress obtained during the compaction is almost the lowest major principal stress that the powder experienced during the shear tests, that is 988 Pa. At this point the lid is moved up to its initial position at the same velocity of the compaction step (Figure IV.16c). During this stage, the bed relaxes because of the elastic behaviour of the particles. Then, the lid is moved down again at V= 0.001 m s^{-1} (Figure IV.16d) and the hemicylindrical walls of the cylinder are removed sideways in opposite directions at V=0.05 m s^{-1}. The absence of adhesive forces between the particle and the wall ensures that this movement of the mold does not produce any traction stress on the powder that would affect its state of consolidation. During this step, the coefficient of rolling friction and of sliding friction between the particles and the lid and between the particles and the base is increased from $1 \cdot 10^{-4}$ to 1 to avoid particles from sliding on the wall of the geometries during the compression step. The simulation time was about 2 days with a time step of 20 % of the critical time step.

The unconfined compression stage is carried out by imposing a downward movement to the lid and by registering, step by step, the total force exerted by the lid on the powder bed. In a real uniaxial experiment, the maximum of this force divided by the cross section of the bed should correspond to the unconfined yield strength. In fact, it corresponds with the fracture of the bed and the loss of its strength. However, in the numerical calculations the force measured on the lid follows the general trend reported in Figure IV.17. The figure reports the force relative to the whole simulation in two panes. Figure IV.17a reports the force as a function of time. Figure IV.17b reports the force as a function of the lid position. The first peak (point A) corresponds to the initial compaction of the bed before the unconsolidated compression. It appears that during the unconfined compression the force does not reach a maximum value but the lid continues to move for a long lid displacement without significant change. The kinds of bed deformation observed are reported in Figure IV.18. It appears clearly that in the simulations the bed starts shearing without breaking (Figure IV.18b). Only after long times and at very large bed deformations the force starts increasing again and raises above the plateau value, due to the limited space remaining available for the bed compression. In the simulation particles cannot fall due to the lack of gravity but particles might in principle detach. This happens only at very low values of Γ_{P-P} (Figure IV.18a). In order to compare simulation results with the experiment the yield of the powder is assumed to happen at the attainment of the plateau value of the compression force, that was used to calculate the unconfined yield strength.

Figure IV.19 reports the values of the unconfined yield strength (f_c) as function of the coefficient of rolling friction ($\mu_{R,P-P}$) provided a fixed value

of Γ_{P-P}. Fitting these values of f_c with a regression line, the couple of the parameters ($\mu_{R,P-P}$, Γ_{P-P}) which gives the experimental f_c is the desired one.
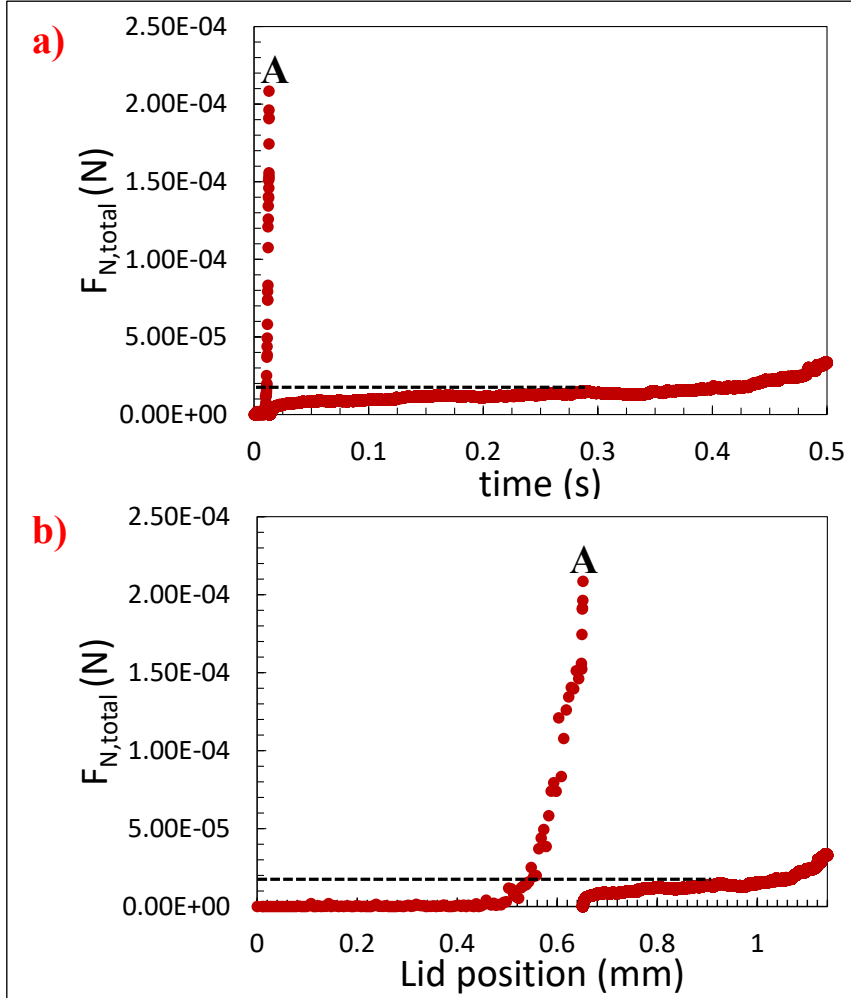
Figure IV.17 *Total normal force exerted by the lid on the powder bed as function of a) time and b) lid position. These graphs have been obtained for $\Gamma_{P-P} = 1 \cdot 10^{-3} \, J \, m^{-2}$ and $\mu_{R,P-P} = 0.8$ with a time step of 20 % of the critical time step. The first peak (point A) corresponds to the initial compaction of the bed in the consolidation step, the black hyphenated line corresponds to the plateau value of the force assumed valid for the calculation of the unconfined yield strength.*
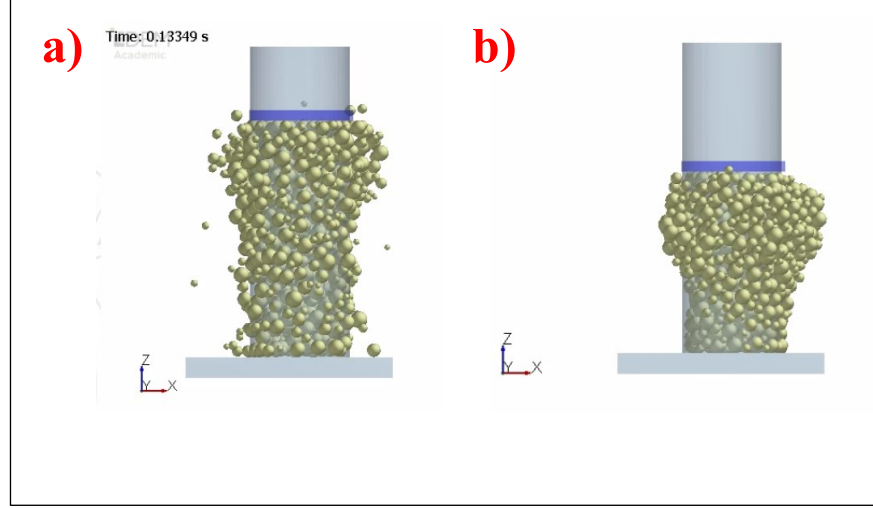
Figure IV.18 *Behaviour of powder for: a) $\Gamma_{P-P} < 1\cdot10^{-5}\ J\ m^{-2}$ and b) $\Gamma_{P-P} > 1\cdot10^{-5}\ J\ m^{-2}$.*

IV.5.2.2 Results

With the aim of finding new pairs, values of Γ_{P-P} and of the coefficient of rolling friction were sought comparing the experimental value of the unconfined yield strength and the model results of uniaxial idealized test. Time steps of 20 and 40 % of Rayleigh time step were adopted. In these simulations, Γ_{P-P} was set between 10^{-5} and 10^{-2} J m^{-2} and $\mu_{R,P-P}$ was changed between 0.1 and 1. Results are reported in Figure IV.19 . The error bars correspond to different values obtained by measuring f_c with a time step of 20 % and 40 %. The bars are quite short and it proves that the measured value does not change much if the time step is varied in the aforementioned range. In the tested range it was possible to find out only a single couple $(\mu_{R,P-P}, \Gamma_{P-P})$ for which the experimental f_c is matched by f_c from the simulation and is provided by the intersection of the regression line of simulation results corresponding to $\Gamma_{P-P}=1\cdot10^{-2}$ J m^{-2} with the red line corresponding to the experimental value of f_c. The intersection occurs at $\mu_{R,P-P}=0.326$ and correspondingly the f_c obtained from the simulations is 141 $\pm$ 7 Pa.

In the case of 10^{-5} J m^{-2}, for $\mu_{R,P-P} < 0.8$ it was not possible to find any simulation value for f_c because the particles separated before the unconfined compression due to the very low values of resulting forces keeping them together. This case is the one reported in Figure IV.18a. From Figure IV.19 it appears that the higher the Γ_{P-P}, the higher is the resulting f_c, fixed the value

of $\mu_{R,P-P}$. In fact, the higher is the Γ_{P-P} , the higher are the van der Waals attractive force between the particles and, correspondingly, the higher is f_c.
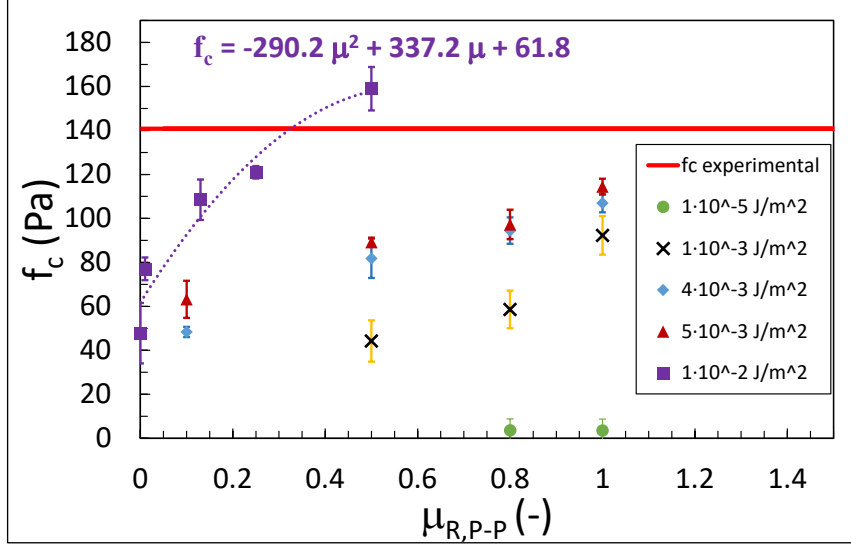
Figure IV.19 *Unconfined yield strength, f_c, as function of $\mu_{R,P-P}$ for different values of Γ_{P-P}:* ●, $1 \cdot 10^{-5}$ *J m^{-2}*; ×, $1 \cdot 10^{-3}$ *J m^{-2}*; ♦, $4 \cdot 10^{-3}$ *J m^{-2}*; ▲, $5 \cdot 10^{-3}$ *J m^{-2}*; ■, 10^{-2} *J m^{-2}. The continuous horizontal line corresponds to the experimental f_c. The violet dotted line corresponds to the interpolating polynomial in case of $\Gamma_{P-P} = 1 \cdot 10^{-2}$ J m^{-2}.*

IV.5.3 Comparison between the two calibration procedures

The comparison between Figure IV.13 and Figure IV.19 shows that the only value of the interfacial adhesive surface energy for which both the experimental α and f_c are matched by the ones from the simulations is $\Gamma_{P-P}=1 \cdot 10^{-2}$ J m^{-2}. However, this happens with different coefficients of the rolling friction namely with a value of $\mu_{R,P-P}$ close to $5 \cdot 10^{-5}$, calibrating results using the angle of repose simulation, and with a value of $\mu_{R,P-P} = 0.326$, in case of the unconfined compression test simulation. Therefore, it would seem that using DEM as it has been done, adopting the Hertz-Mindlin (no slip) contact model with the JKR model for cohesion, it is not possible to calibrate the model so that it can contemporarily produce correct values of the unconfined yield strength and of the static angle of repose. This disappointing result may be related with the other circumstance that has been observed above, regarding the lack of an apparent yield with a maximum of the compression force in the uniaxial unconfined compression test suggesting that

the model used is not able to properly describe the powder shear mechanisms during the unconfined yield.

Moreover, if the couples identified with both the procedures (Table IV.5, Table IV.6 and the couple identified using the unconfined yield strength) are tried in the same simulation of spreading of powder as the one described in paragraph IV.4.1, none of them is able to provide the same bulk density and the same porosity obtained from the experiments, as demonstrated in Table IV.7.

Table IV.7 *Parameters (Γ_{P-P}, Γ_{P-G}, $\mu_{R,P-P}$) found with DEM calibration using the angle of repose and the unconfined yeld strength and used in simulations of spreading of the powder with the corresponding measured properties ($\rho_{b,sim}$, ε_{sim}) and comparison with the experimental properties ($\rho_{b,exp}$, ε_{exp}).*

Γ_{P-P} (J m^{-2})	Γ_{P-G} (J m^{-2})	$\mu_{R,P-P}$ (-)	$\rho_{b,sim}$ (kg m^{-3})	$\rho_{b,exp}$ (kg m^{-3})	ε_{sim} (-)	ε_{exp} (-)
$1\cdot10^{-3}$	$1.03\cdot10^{-3}$	$6.2\cdot10^{-2}$	474 ± 5	261 ± 18	0.58 ± 0.005	0.77 ± 0.016
$1\cdot10^{-5}$	$1.03\cdot10^{-5}$	$2\cdot10^{-1}$	414 ± 7	261 ± 18	0.64 ± 0.006	0.77 ± 0.016
$4\cdot10^{-3}$	$4.1\cdot10^{-3}$	$6.7\cdot10^{-3}$	476 ± 11	261 ± 18	0.58 ± 0.01	0.77 ± 0.016
$5\cdot10^{-3}$	$5.13\cdot10^{-3}$	$2.2\cdot10^{-4}$	496 ± 18	261 ± 18	0.57 ± 0.02	0.77 ± 0.016
$2\cdot10^{-3}$	$2.05\cdot10^{-3}$	$3.2\cdot10^{-2}$	459 ± 7	261 ± 18	0.6 ± 0.006	0.77 ± 0.016
$3\cdot10^{-3}$	$3.08\cdot10^{-3}$	$1.9\cdot10^{-2}$	465 ± 8	261 ± 18	0.6 ± 0.007	0.77 ± 0.016
$5\cdot10^{-4}$	$5.13\cdot10^{-4}$	$7.6\cdot10^{-2}$	459 ± 10	261 ± 18	0.6 ± 0.008	0.77 ± 0.016
$1\cdot10^{-2}$	$1.03\cdot10^{-2}$	$3.26\cdot10^{-1}$	2.72 ± 2	261 ± 18	0.98 ± 0.03	0.77 ± 0.016

Therefore, all these couples of parameters were not used with the purpose of validating the DEM model of spreading of powder, which will be explained in the next paragraph.

Perhaps some alternative contact models or the use of different particle shapes should be tried in the future to verify whether the DEM model is able to describe with the same calibration parameters the unconfined yield and the correct static angle of repose and to check whether these parameters are able

to provide the same powder layer properties (bulk density and porosity) as the experiment.

IV.6 DEM simulation of spreading of the powder

Simulations of spreading of the powder layer were carried out with the purpose of validating the DEM model.
For this purpose, the same procedure of powder layering as the one described in paragraph IV.4.1 was adopted. In particular, a scrolling velocity of the blade (V_S) of $3 \cdot 10^{-2}$ m s^{-1} was set.

Powder layers with a length of $1.5 \cdot 10^{-2}$ m, a height of $300 \cdot 10^{-6}$ m and a width of $950 \cdot 10^{-6}$ m were obtained.

Values of interfacial surface energies and of coefficient of rolling friction (Table IV.8) which were used for the validation of the model are the correct ones found in the paragraph IV.4.2 through the calibration procedure.

However, to demonstrate the appropriateness of these parameters, other simulations of powder spreading, in which the parameters found with the other two calibration procedures have been set, were carried out and the resulting powder surfaces have been analysed as described in the next paragraph.

Table IV.8 *Simulation of spreading of PA6 powder. V_S is the scrolling velocity of the blade, Γ_{P-P}, Γ_{P-G} are the interfacial surface energy between the particles and between the particles and the geometries, respectively; $\mu_{R,P-P}$ and $\mu_{R,P-G}$ are the coefficient of rolling friction between the particles and between the particles and the geometries, respectively.*

V_S (m s^{-1})	Γ_{P-P} (J m^{-2})	Γ_{P-G} (J m^{-2})	$\mu_{R,P-P}$, $\mu_{R,P-G}$ (-)
$3 \cdot 10^{-2}$	0.0019	0.00195	0.19

A time step of 40 % of critical Rayleigh time step was used. Simulation lasted one week.

IV.6.1 Representation of the simulated powder layer for the surface analysis

Once the simulation finished, particles of the powder layer were coloured according to the position along the vertical direction (z) with the purpose of reproducing proper lighting conditions of the powder layer like in the experiments. Different shades of grey were used from top to bottom: white, light grey, grey, dark grey and black (Figure IV.20).

The black colour (Figure IV.20) was assigned to the deposition tray to simulate the absence of light below the layer.

Then, a picture of the powder layer from the top was captured with a reference length (Figure IV.20a) for setting the actual scale with ImageJ.

In ImageJ, the same procedure as the one described in the paragraph III.4 was adopted to cut out a rectangle with the sides of the same desired dimensions of the layer, namely a length of $1.5 \cdot 10^{-2}$ m and a height of $95 \cdot 10^{-5}$ m.

The final image was opened in Microsoft Paint to get the same height in pixels of the images obtained from the experiment.

In the end, the image (Figure IV.21) was analysed by means of MATLAB, as described in paragraph III.4.2.
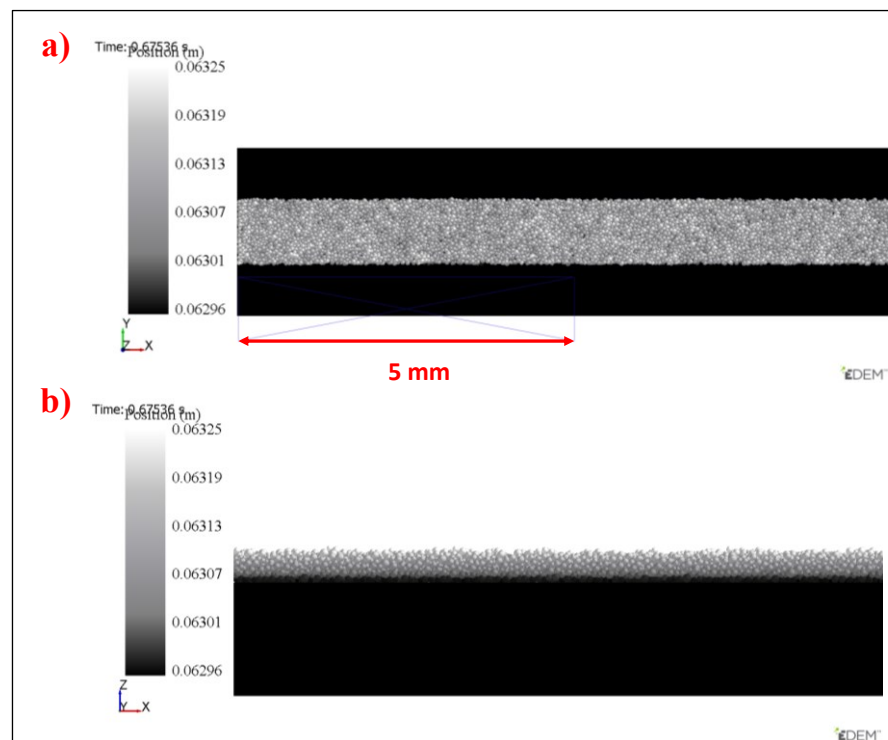
Figure IV.20 *Powder layer whose particles have different colour according to the z-position: a) top view of the powder layer with a length reference of 5 mm; b) side view.*
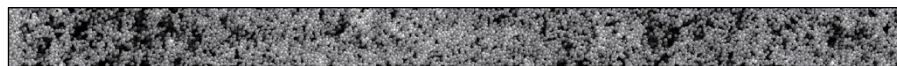
Figure IV.21 *a) Image of the powder layer with a black deposition tray analysed with MATLAB.*

Chapter V
Results and discussion

V.1   Experimental results

V.1.1   Analysis of the powder layer obtained with the new setup

Two different types of experimental tests were carried out. They differ for the scrolling velocity of the blade (V_S), namely $3 \cdot 10^{-3}$ and $3 \cdot 10^{-2}$ m s^{-1} (Table V.1). Each test was repeated twice to verify reproducibility of the results. For each test fresh powder was used, that is powder which was never been used before and which was dried and sieved as described in paragraph III.3.

Table V.1 *Summary of the spreading tool used and of the corresponding parameters set in the experimental tests. The only parameter, which has been changed between different tests, is the scrolling velocity of the blade (V_S).*

Spreading tool	Inclination of the spreading tool (with respect to the spreading direction)	Angle of tip	Depth of trays (μm)	V_S (m s^{-1})
Blade	Vertical	30°	300	$3 \cdot 10^{-3}$
				$3 \cdot 10^{-2}$

Macroscopic and microscopic results of the tests are reported in Figure V.1 and in Figure V.2, respectively. The former were obtained by using a 108 MP camera. Apparently, it seems that quality of the deposited powder layer gets worse when the scrolling velocity increases (Figure V.1b) compared to the case in which $V_S = 3 \cdot 10^{-3}$ m s^{-1} (Figure V.1a). In fact, in Figure V.1b some dark stripes are evident along the spreading direction while they lack in Figure V.1a.

However, analysis based on the wavelet power spectrum applied to the microscopic images was carried out to provide more punctual information on the tests results.
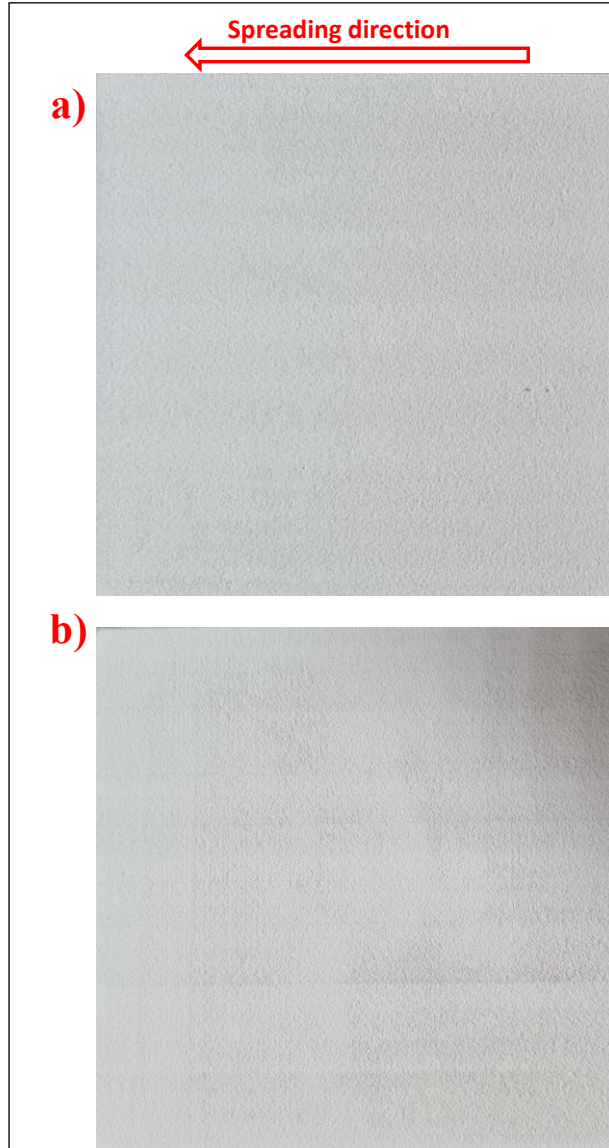
Figure V.1 *Macroscopic images of the powder layers after spreading representative of the tests at V_S of $3 \cdot 10^{-3}$ (a) and $3 \cdot 10^{-2}$ m s^{-1} (b).*
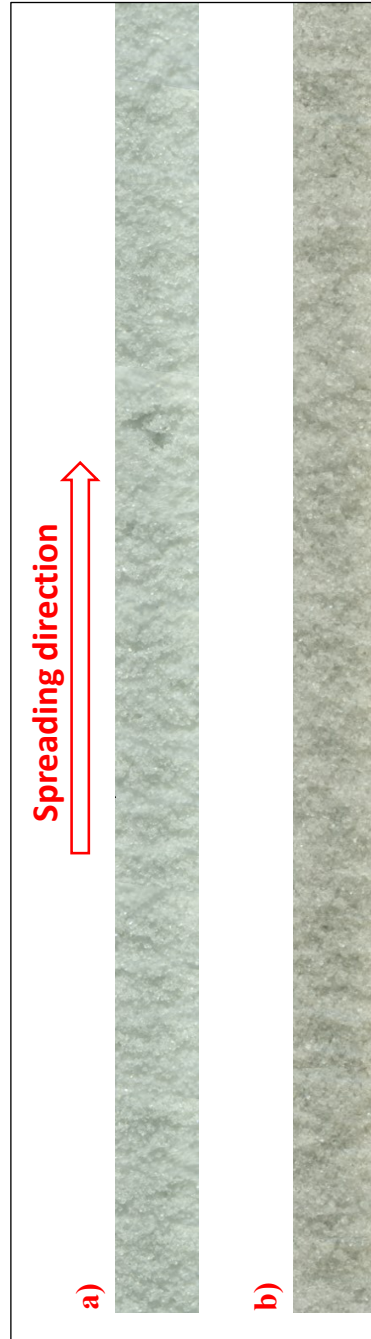
Figure V.2 *Microscopic images of the portions of the powder layers after spreading representative of the tests at V_S of $3 \cdot 10^{-3}$ (a) and $3 \cdot 10^{-2}$ $m\ s^{-1}$ (b).*

113

In Figure V.3, the characteristic lengths (c.l.) of the powder surface roughness are compared between the two tests.

Minimum and maximum correspond to the extremes of range of lengths calculated from the maximum and minimum wavenumber values, respectively, identified with the power spectra, as described in paragraph III.4.2. Average characteristic length of the powder surface roughness has been calculated from the wavenumber values in correspondence of the peak values of the power spectra. Minimum, average and maximum characteristic lengths are average values of characteristic lengths obtained from power spectra of different tests. The black bars correspond to the standard deviation between different tests.

From Figure V.3, it emerges that asperities are a bit smaller in case of a lower scrolling velocity of the blade, as demonstrated by the lower minimum and average values of the characteristic lengths. In case of the maximum c.l., difference of the values between the two spreading conditions are less evident, if the error bars are considered. In case of the maximum c.l. of roughness, the reason by which the error bar is larger with respect to those in correspondence of the minimum and the average c.l. is due to some differences in the shapes of the wavelet power spectra between different tests at the same scrolling velocity. In fact, looking at Figure V.4, which represents the power spectra obtained with two different tests (test 1 and test 2) for the same scrolling velocity ($3 \cdot 10^{-3}$ m s^{-1}), the difference between the minimum values of wavenumbers is greater compared to the difference of the maxima values, due to local differences in the shapes of the two spectra. Minimum wavenumbers correspond to maxima wavelengths, i.e. maxima characteristic lengths of roughness.

However, the peaks of the power spectra, which are the most important because represent the most frequent c.l. of roughness, are almost identical between the two spectra.

The slight increase of the scrolling velocity has some effect on the quality of the spread powder layer, thus confirming the macroscopic analysis.

More precisely, the c.l. of roughness resulted to be $200 \div 500$ μm, that around $3.6 \div 9$ times the average particle diameter (D_{50}), in case of the blade at $3 \cdot 10^{-3}$ m s^{-1}. Instead, in case of the blade at $3 \cdot 10^{-2}$ m s^{-1}, c.l. of roughness resulted to be $5.5 \div 11$ times D_{50} (Figure V.3).

The c.l. of the powder surface roughness has been compared with the dimension of the aggregates, evaluated from the Bo number, as described in paragraph III.5. Two different values of the Bo number have been calculated from the interparticle forces, evaluated by using different values of the isostatic tensile strength (Table IV.2). Therefore, a range of possible values for the Bo number has been identified (Table IV.3).

Because of the definition of the Bo number, it does not depend on the spreading velocity. For the tested powder, the dimension of aggregates is between 236 and 263 μm (black hyphenated lines in Figure V.3), depending

114

on the isostatic tensile strength used and hence on the evaluated interparticle force (Table IV.3).

Even if dimension of aggregates depends on the Bo number, according to eq. (36), however, the spreading process is not merely related to the gravity forces acting on the powder particles, but it is forced by a spreading tool. Therefore, it would seem that there is not a direct relationship between the characteristic length of roughness and the dimension of aggregates, evaluated from the Bo number.
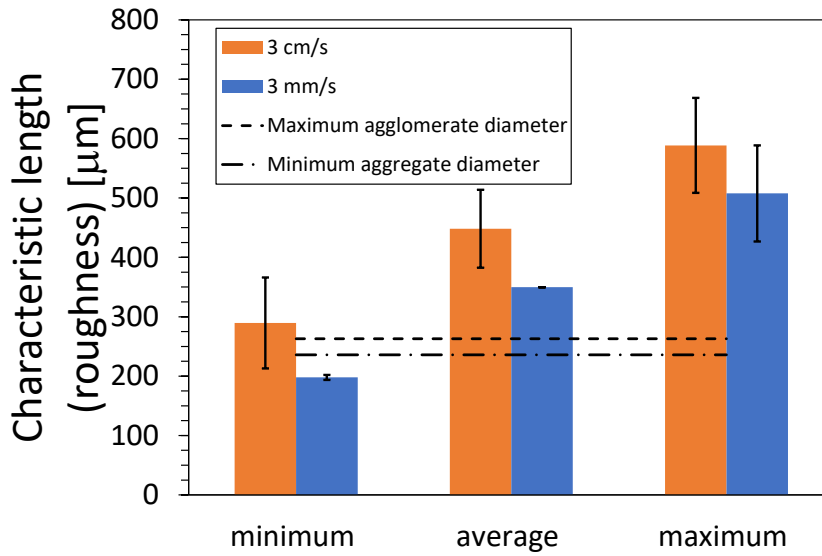
Figure V.3 Values of minimum, average and maximum characteristic length of the powder surface roughness for V_S equal to $3 \cdot 10^{-3}$ m s^{-1} (blue bars) and to $3 \cdot 10^{-2}$ m s^{-1} (orange bars). Black hyphenated lines correspond to minimum (lower line) and maximum (upper line) values of the particle aggregate dimensions, obtained according to eq. (36) with $Bo_2 = 79.1$ and $Bo_1 = 110$, respectively.

When two different tests at $V_S = 3 \cdot 10^{-2}$ m s^{-1} are compared but in the second one re-used powder is employed, there is slight deterioration of the powder layer surface quality as demonstrated by Figure V.5 for average and maximum values of the c.l. of the powder surface roughness. Re-used powder means that the same powder has been used again, after being dried in oven for at least 1 hour at 100 °C and sieved as described in paragraph III.3.

In case of fresh powder, the c.l. of roughness resulted to be $300 \div 600$ μm, that around $5.5 \div 11$ times the average particle diameter (D_{50}). Instead, in case of the re-used powder sample, c.l. of roughness resulted to be $8.2 \div 14.2$ times D_{50}.

Looking at the macroscopic image (Figure V.6) it is evident that the layer obtained with re-used powder is worse compared to the one obtained with fresh powder (Figure V.1b). Indeed, in the image, darker regions can be seen, which demonstrate worse distribution of the powder. These regions correspond to shadows of the local powder hills projected onto the local valleys due to grazing light. The larger the shadows, the bigger the roughness of the layer and hence less uniform the distribution of the powder. Hills are representative of internal cohesion of the powder and thus of higher interparticle forces compared to the weight of the particles, that is to a higher Bo number.
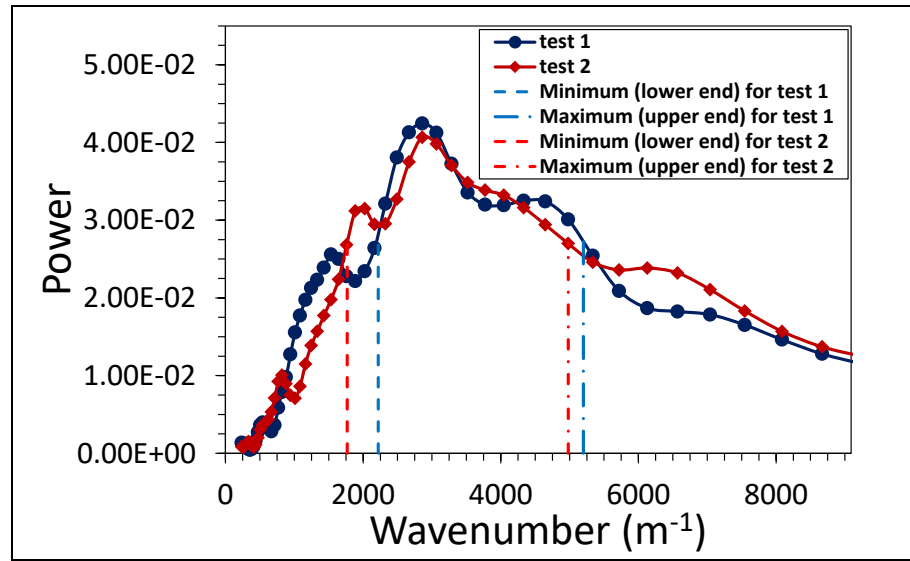
Figure V.4 *Comparison between the wavelet power spectra obtained with test 1 (blue line) and test 2 (red line), both at $V_S = 3 \cdot 10^{-3}$ m s^{-1}. Red and blue hyphenated lines correspond to the minimum wavenumber (maximum values of the c.l. of roughness) for test 1 and 2, respectively. Red and blue dash-dot lines correspond to the maximum wavenumber values (minimum values of the c.l. of roughness) for test 1 and 2, respectively.*

The more cohesive behaviour of the powder could be explained by capillary forces between particles of a re-used powder.

Capillary forces are affected by humidity and temperature. In case of PA6, temperature has an important effect. In fact, at 100 °C there is an improvement of the flowability compared to the ambient temperature, as demonstrated by Ruggi et al. (Ruggi, Lupo, *et al.*, 2020). At 100 °C, air humidity cannot produce significant capillary forces. Moreover, at this temperature, the hardness of the polymeric material of the particles is likely to be still scarcely affected by temperature. Therefore, it is necessary to properly dry the powder

in the oven before using it again. Based on the performed tests, it is likely that drying was not sufficient to guarantee a good quality of the powder sample for a new test. Two other possible causes of bad quality of the re-used powder are: improper sieving before the test and combined effect of bad environmental conditions and of exposure time of powder sample to the environment during the tests.
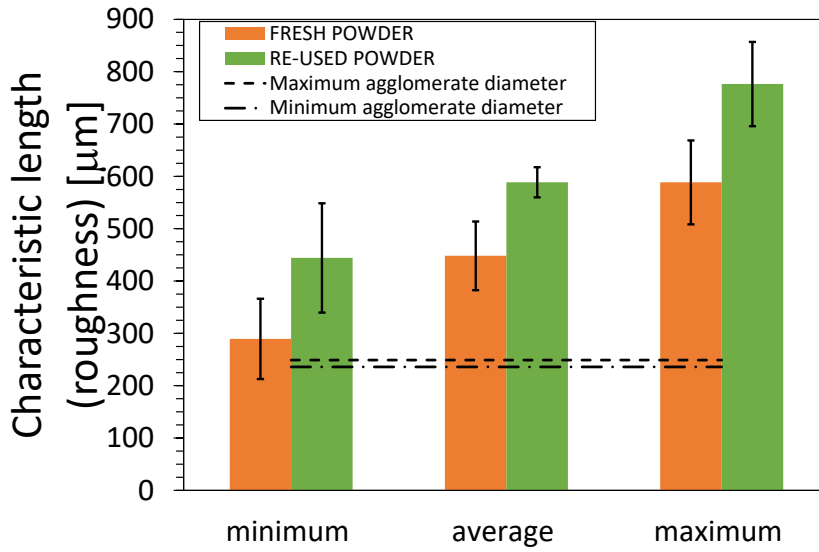
Figure V.5 *Values of minimum, average and maximum characteristic length of the powder surface roughness for V_S equal to $3 \cdot 10^{-2}$ m s^{-1} in case of fresh (orange bars) and re-used powder (green bars). Black hyphenated lines correspond to minimum (lower line) and maximum (upper line) values of the particle aggregate dimensions, obtained according to eq. (36) with $Bo_2 = 79.1$ and $Bo_1 = 110$, respectively.*

Based on the maximum particle diameter of fresh powder, it is necessary to use sieves whose meshes have proper sizes, i.e. not larger than the maximum particle diameter to retain possible particle aggregates.

In the performed tests, sieves with 150 μm meshes, that is around 1.24 times D_{90}, were used. Therefore, meshes with lower sizes of the sieve should be used to retain the aggregates.

Tests have been performed at ambient humidity and temperature. In case of powders with high hygroscopicity like polyamides (Ruggi, Barrès, *et al.*, 2020), it is better to test them in temperature and humidity-controlled environment. Moreover, the longer the exposure to ambient humidity the more the adsorption of water molecules onto the grain surface until the powder saturation.

Therefore, to start from the same quality of the powder to spread and to guarantee reproducible results it is better to test powders in controlled environmental conditions. By doing so, proper drying in the oven and proper sieving of the powder should be sufficient to guarantee reproducible results with the same powder sample.

In the future, a system to test powders in a controlled environment will be implemented. Tests will be performed to verify the effect of proper preparation of powders, before being re-used, on the quality of the spread powder.

Figure V.6 *Macroscopic image of the deposited powder layer for V_S equal to $3 \cdot 10^{-2}$ m s^{-1} when the powder has been re-used.*

V.2 DEM simulation of spreading of the powder: results

V.2.1 Analysis of the simulated powder layer: validation

Simulation of the powder layering in the same conditions of the experiments have been carried out by adopting the procedure described in paragraph IV.6. The purpose has been to validate the DEM model.

Image of the powder layer obtained with the simulation, in which the parameters used are those reported in Table IV.8, is presented in Figure V.7.

The wavelet power spectrum has been applied to the image of Figure V.7 and the results in terms of the characteristic length, representative of the surface roughness, are reported in Table V.2.

Table V.2 *Average characteristic lengths (c.l.) of powder surface roughness in correspondence of the peak value of the power spectrum and of the two-thirds of the peak value (Min and Max) for the experimental (Tests) and the characteristic lengths for the simulated powder layer at a blade velocity (V_S) of $3 \cdot 10^{-2}$ m s^{-1}.*

V_S (m s^{-1})		*c.l. of roughness*		
		Min (µm)	Peak (µm)	Max (µm)
$3 \cdot 10^{-2}$	*Tests*	289.5 ± 76.6	448.2 ± 65.7	588.5 ± 80.1
	Simulation	277.8	430.6	512.8

Comparison (Table V.2) between the characteristic lengths of powder surface roughness in correspondence of the peak values of power spectra obtained from the simulation and from the experiment at the same V_S shows a good match

Therefore, the DEM model is able to properly reproduce the experimental results.
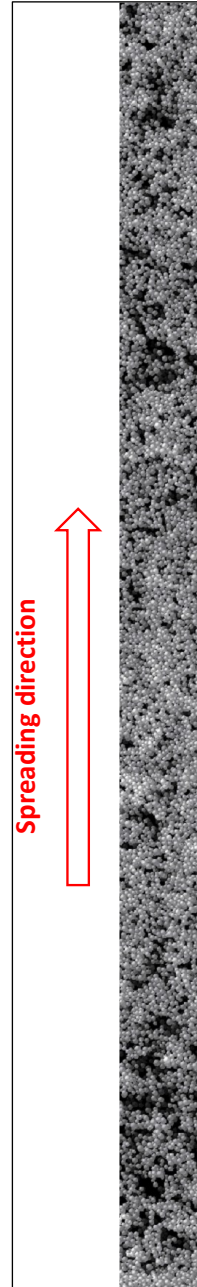
Figure V.7 *Top view of the powder layer obtained with a blade velocity of 3·10⁻² m s⁻¹.*

V.2.2 Comparison among the simulations in which different parameters have been used

As proof that the calibration procedure for the determination of the rolling friction coefficient as described in paragraph IV.4 is the right one, values of the c.l. of roughness obtained by using the parameters of Table IV.4, except the case of a rolling friction coefficient of 0.3, are compared with those (Table IV.7) obtained from the calibration procedures using the static angle of repose and the unconfined yield strength. From each image of the simulated powder layer, the c.l. of roughness has been calculated in correspondence of the peak value of the wavelet power spectrum.

In all the simulations a blade velocity of $3 \cdot 10^{-2}$ m s^{-1} has been used.

To each group of parameters, a number has been assigned (Table V.3) to make easier the comparison. For example, number 2 corresponds to the powder layer of Figure V.7.

Table V.3 *Values of parameters obtained from the calibration procedures: for the determination of coefficient of rolling friction (Spreading), using the static angle of repose (Angle of repose) and using the unconfined yield strength (UYS).*

Simulation number	Calibration procedure	Γ_{P-P} (J m^{-2})	Γ_{P-G} (J m^{-2})	$\mu_{R, P-P} = \mu_{R, P-G}$ (-)
1	Spreading			0.1
2	Spreading	$1.9 \cdot 10^{-3}$	$1.95 \cdot 10^{-3}$	0.19
3	Spreading			0.3
4	Angle of repose	$1 \cdot 10^{-3}$	$1.03 \cdot 10^{-3}$	$6.2 \cdot 10^{-2}$
5	Angle of repose	$1 \cdot 10^{-5}$	$1.03 \cdot 10^{-5}$	$2 \cdot 10^{-1}$
6	Angle of repose	$4 \cdot 10^{-3}$	$4.1 \cdot 10^{-3}$	$6.7 \cdot 10^{-3}$
7	Angle of repose	$5 \cdot 10^{-3}$	$5.13 \cdot 10^{-3}$	$2.2 \cdot 10^{-4}$
8	Angle of repose	$2 \cdot 10^{-3}$	$2.05 \cdot 10^{-3}$	$3.2 \cdot 10^{-2}$
9	Angle of repose	$3 \cdot 10^{-3}$	$3.08 \cdot 10^{-3}$	$1.9 \cdot 10^{-2}$
10	Angle of repose	$5 \cdot 10^{-4}$	$5.13 \cdot 10^{-4}$	$7.6 \cdot 10^{-2}$
11	UYS	$1 \cdot 10^{-2}$	$1.03 \cdot 10^{-2}$	$3.26 \cdot 10^{-1}$

As examples, the images of the powder layer surface obtained for simulations 4 and 5 are reported in Figure V.8. Images from all the other simulations are reported in Appendix D.
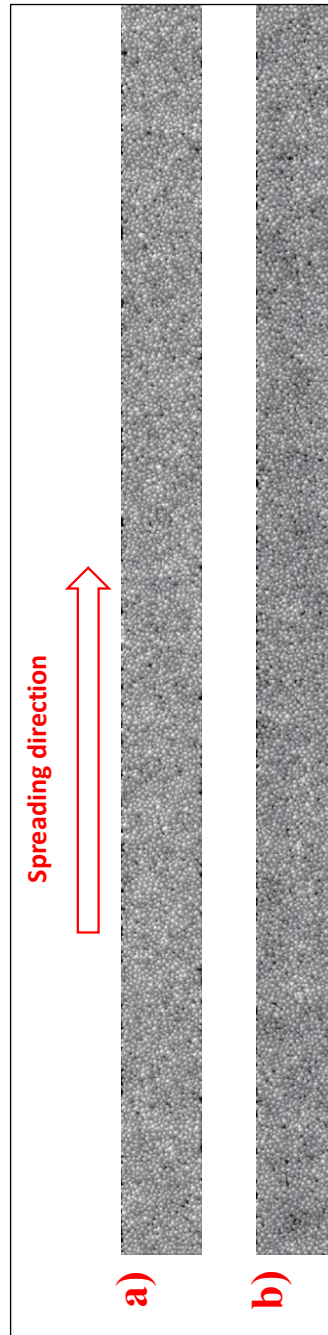
Figure V.8 *Image of the powder layer viewed from top for simulations: a) number 4 and b) number 5 of Table V.3.*

Simulations number 3 and 11 (Table V.3) provide results which are not reliable due to the presence of large portions of the deposition tray which remain not covered with powder. If the black in the image is due to the deposition tray rather than to the particles in the lower part of the layer, the c.l. of roughness, which is evaluated by using the procedure based on power spectra, does not correspond to the actual one. For this reason, the results obtained in these two cases are reported in Appendix D and are not compared with those achieved with the other simulations.

The results of the comparison are reported in Figure V.9.

Analysis of Figure V.9 shows that only in case of simulation 2 for which the porosity (Figure V.9a) and the bulk density (Figure V.9b) match the experimental values, there is also a good match with the experiments in terms of surface quality, represented by the c.l. of roughness. In all the other cases, quality of the powder surface is different from the one obtained in the experiments. In the graphs, the red hyphenated lines correspond to the deviation of the experimental c.l. of roughness, evaluated as the standard deviation of the values of characteristic length obtained in correspondence of the peak value of power spectra for different tests. Blue hyphenated lines correspond to the standard deviation of porosity calculated from different measurements of mass (Figure V.9a), while black hyphenated lines correspond to the standard deviation of the experimental values of the bulk density obtained from different measurements (Figure V.9b), as described in paragraph IV.4.1.

Analysis of Figure V.9a and b shows also that the lower the bulk density and hence the higher the porosity, the higher is the c.l. of roughness. This result should not be surprising since the roughness is related to lesser capacity of the powder to deposit due to cohesiveness of the powder, as reported in many works (Haeri *et al.*, 2017; Chen *et al.*, 2020; Lee *et al.*, 2020). Therefore, the higher the internal friction of the powder the lower the capacity of the particles to fall and form dense layers.

123
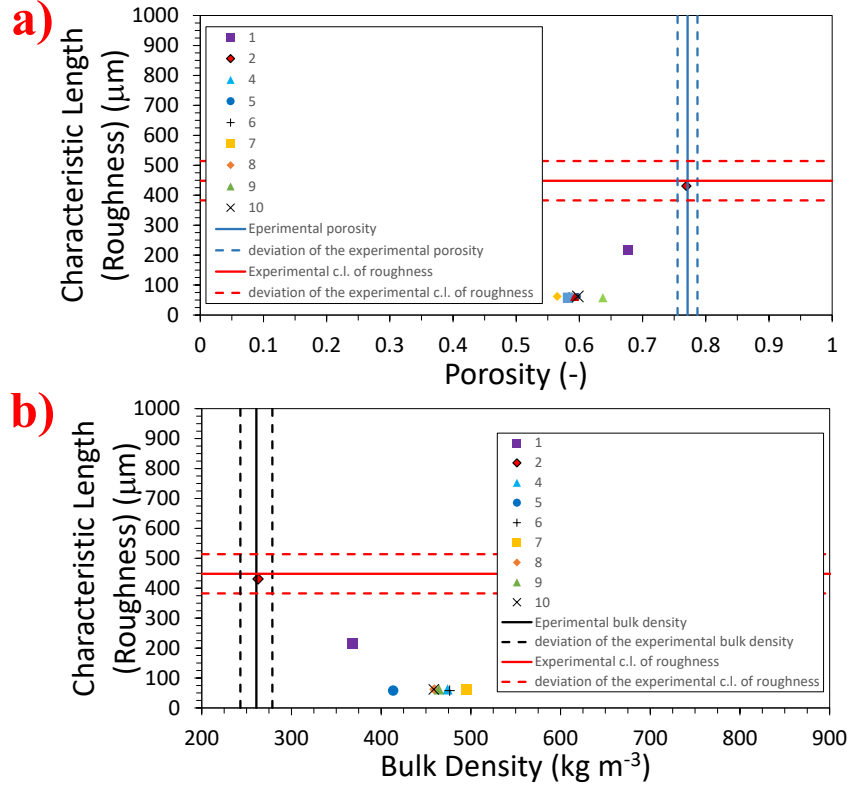
Figure V.9 *Characteristic length of roughness as function of porosity (a) and of bulk density (b) for all the simulations tried and comparison with the experimental values. Each simulation is represented by a number. Details about the values of the parameters used are reported in Table V.3. Red, black and blue solid lines correspond to the experimental characteristic length (c.l.) of roughness, bulk density and porosity, respectively. Hyphenated lines of the same colour correspond to the deviation of the aforementioned properties.*

The adopted procedure, based on the comparison between the c.l. of surface roughness of the experimental and the simulated deposited powder, revealed to be a correct way to validate the DEM model. The match between the values of the c.l. of surface asperities, obtained from the wavelet power spectra applied to both the simulated and the actual powder layer, suggests that the powder representation in the DEM model, although it is not rigorous, is sufficient to describe the actual powder behaviour in the same spreading conditions of the experimental tests.

Conclusions

Purpose of this work was to develop some tools, which could be useful to determine the best spreading conditions for each powder analysed.

Two tools were adopted: a new experimental setup and a DEM model.

The experimental setup allows to distribute a powder heap to form a thin layer of different heights. Moreover, different spreading conditions can be tried due to the possibility to vary the spreading tool, its scrolling velocity, its inclination with respect to the spreading direction.

The spreading system allows also to combine the action of a blade and of a roller. In fact, application of the Johanson's model to the compaction of the powder layer suggested that a possible configuration could be that of putting the blade in front of the roller. By doing so, the blade spreads the powder and fixes the angle of attack of the powder on the roller, which then compresses the deposited layer. This configuration, to the best of my knowledge, is new and could be a good solution especially in cases in which powders that are not purposely designed for the SLS are used. In fact, the poor quality of spreading could be counterbalanced by the attainment of a denser layer due to the compaction. Furthermore, the setup was designed in view of its future applications. For example, stainless steel was chosen as material for many of the parts of the setup due to its high mechanical and thermal resistance. In fact, in the case that the roller is used, high compression stresses are exerted on the deposition plate and hence high resistance to deformation of the plate is necessary in order not to affect the thin thickness of the powder layer. And also, there is the future intention to spread powders at temperatures higher than the ambient one to study the effect of temperature on the quality of the distributed powder.

In this work, tests on the polyamide 6 powder at two different scrolling velocities of the blade and at ambient temperature were carried out.

It was possible to set up a very precise system for proper display of the powder layer. It consists of moving a microscope coupled to a high-resolution camera to look at the surface of the powder layer at a particle level in precise positions along the surface under certain lighting conditions. Grazing light was used to highlight the shadows projected by the local hills on the neighbour

valleys of the powder surface. Size of the shadows gives an idea about the powder surface asperity and hence of the quality of the surface.

With a specifically developed procedure, based on the application of the wavelet power spectrum, it was possible to determine the characteristic length (c.l.) of the powder surface roughness by analysing the grey level image of the powder layer, captured with the camera. Dimension of powder surface asperities is representative of powder spreadability because results from the combined effects of particle properties as well as the stress conditions during spreading.

Experiments with a blade at $3 \cdot 10^{-3}$ and at $3 \cdot 10^{-2}$ m s^{-1} showed that c.l. of roughness slightly depends on the scrolling velocity. In fact, quality of the deposited powder layer worsened a little as the velocity was increased by an order of magnitude.

The c.l. of roughness resulted to be around $3.6 \div 9$ times the average particle diameter (D_{50}), in case of a scrolling velocity of the blade of $3 \cdot 10^{-3}$ m s^{-1}, and $5.5 \div 11$ times D_{50}, in case of a velocity of $3 \cdot 10^{-2}$ m s^{-1}.

The slight dependence of surface asperity from the scrolling velocity of the blade demonstrates that the spreading process is not merely related to the gravity forces acting on the powder particles but depends on the actual state of stress of the powder due to movement of the spreading tool.

Therefore, this result would suggest that there is not a direct relationship between c.l. of roughness and dimension of aggregates, evaluated from the Bo number.

Comparison between powder layers obtained by using fresh and re-used powder in the same spreading conditions showed deterioration of the surface layer quality. This result highlighted the importance of proper preparation of the powder in the case that it is re-used. Probably it is necessary to test powders in a temperature and humidity-controlled environment and to properly dry and sieve the powder sample before its re-use.

With a DEM model it was possible to simulate powder layering in different spreading conditions.

In the future, the DEM model will be used as a tool to understand how and why specific operating conditions and powder properties affect the quality of the deposited powder layer.

The main actions to properly develop the model turned out to be: 1) choice of suitable model for calculating the interaction forces between the objects in the simulations, namely particles and geometries; 2) calibration of the DEM parameters; 3) validation of the model.

The Hertz-Mindlin (no slip) with JKR cohesive model allowed to take into account viscoelastic deformation and adhesion between the contacting objects. In the case of the interaction between the particles, this choice is justified by the fact that the value of the measured unconfined yield strength of the material is relatively independent with the consolidation stress, thus

supporting the hypothesis of viscoelastic deformation of the particles at the contact points.

All the calibration procedures tried were able to provide values of the parameters by which the experimental and the simulated properties are matched.

However, the calibration procedure which turned out to be suitable was the one based on the determination of the coefficient of rolling friction between the particles and between the particles and the geometries by comparing the bulk density and the porosity obtained from the simulation of powder spreading with those obtained from the experiments in the same spreading conditions.

The appropriateness of this procedure was due to two reasons.

The first one was that by adopting the parameters found with this procedure, it was possible to validate the DEM model of powder spreading.

The second reason was that these parameters proved to be the only ones among those of the tried calibration procedures able to match the bulk density, the porosity and the c.l. of roughness between the simulation and the experiments.

The image of the simulated powder layer allowed to validate the model. Different colours along the height of the simulated layer were attributed to the particles according to their position, in order to roughly replicate the lighting conditions of the experiments. This allowed to apply to the image a wavelet power spectrum analysis to highlight and quantify the c.l. of the sample surface roughness. The comparison between the values of the c.l. of roughness between the simulated powder layer and the experimental one showed a good agreement.

Comparison between simulations with different values of the DEM parameters showed that the lower the bulk density and the higher the porosity, the higher is the c.l. of roughness. This result agrees with the correlation between the roughness and the capacity of the powder to settle, which depends on its cohesiveness. The higher the internal friction of the powder, the lower the capacity of the particles to fall and to form dense layers.

Future work

In the future, starting from the validated model, different spreading configurations will be simulated and tested to understand which is the effect on the quality of the powder layer surface when are used:

- blades with different inclinations with respect to the deposition tray;
- different angles of the blade's tip;
- different scrolling velocities of the blade;
- different layer thicknesses;
- the roller in combination with the blade or alone to compact the powder layer or to spread the powder, by adopting different scrolling and rotational velocities and different directions of rotation;

In the latter case, it is likely that a different model for the evaluation of the contact forces should be used to consider plastic deformation between the objects involved (particles and geometries) in the contact point due to high compression stresses exerted by the roller.

A system to measure the pressures in different points across the powder layer will be implemented with the purpose of validating the Johanson's model. This model could be used to know whether the compression with a roller is feasible or not for the tested powder.

The DEM model will be used as a tool to understand how and why specific operating conditions and powder properties affect the quality of the deposited powder layer for each powder analysed. Rather than finding the best spreading configuration for a commercialised SLS powder, theoretically, it could be possible to engineer appropriate powders for a defined spreading configuration, with the purpose of optimizing the distribution process and consequently the quality of the spread powder layer.

An automatic procedure for collecting images of portions of the powder layer will be developed to speed up the image acquisition procedure.

A system for controlling the environmental conditions during powder spreading will be implemented for two reasons:

1) guarantee a temperature and humidity-controlled environment in order to have more reproducible tests and to use the same powder sample many times with the advantage of reduced costs for buying the powder;

Future work

2) test powders at temperatures closer to those of a typical SLS process, namely higher than ambient temperature, to study the effect of temperature on powder distribution.

Also, deposited powder layers will be sintered with a laser and studies about the effects of quality of the spread powder layer on the quality of the sintered layer will be carried out.

References

Ben Abbes, A. *et al.* (2018) Comparative study of three satellite image time-series decomposition methods for vegetation change detection. *European Journal of Remote Sensing*, **51**(1), 607–615.

Abdullah, E. C. and Geldart, D. (1999) The use of bulk density measurements as flowability indicators. *Powder Technology*, **102**(2), 151–165.

Ahmed, M. *et al.* (2020) A simple method for assessing powder spreadability for additive manufacturing. *Powder Technology*, **367**, 671–679.

Ai, J. *et al.* (2011) Assessment of rolling resistance models in discrete element simulations. *Powder Technology*, **206**(3), 269–282.

Aldahsh, S. (2013) Dependence of SLS Parameters on Thermal Properties of Composite Material of Cement with Polyamide 12. *Journal of Applied Mechanical Engineering*, **2**(5).

Alder, B. J. and Wainwright, T. E. (1957) Phase transition for a hard sphere system. *The Journal of Chemical Physics*, **27**(5), 1208–1209.

Alickovic, E., Kevric, J. and Subasi, A. (2018) Performance evaluation of empirical mode decomposition, discrete wavelet transform, and wavelet packed decomposition for automated epileptic seizure detection and prediction. *Biomedical Signal Processing and Control*, **39**, 94–102.

Alizadeh, E., Bertrand, F. and Chaouki, J. (2013) Development of a granular normal contact force model based on a non-Newtonian liquid filled dashpot. *Powder Technology*, **237**, 202–212.

Alizadeh, M. *et al.* (2017) The effect of particle shape on predicted segregation in binary powder mixtures. *Powder Technology*, **319**, 313–322.

Alizadeh, M. *et al.* (2018) A methodology for calibration of DEM input parameters in simulation of segregation of powder mixtures, a special focus on adhesion. *Powder Technology*, **339**, 789–800.

Amado, A. *et al.* Advances in SLS powder characterization. Proc. of the *22nd Annual International Solid Freeform Fabrication Symposium - An Additive Manufacturing Conference,* August 8-10, 2011, Texas (USA), p. 438–452.

References

Amado, A., Schmid, M. and Wegener, K. Flowability of SLS powders at elevated temperature. Proc. of the *10th Rapid. Tech Conference*, May 14-15, 2013, Erfurt (Germany), p. 1–7.

Angus, A. *et al.* (2020) Calibrating friction coefficients in discrete element method simulations with shear-cell experiments. *Powder Technology*, **372**, 290–304.

Averardi, A. *et al.* (2020) Effect of particle size distribution on the packing of powder beds: A critical discussion relevant to additive manufacturing. *Materials Today Communications*, **24**.

Baran, O. *et al.* DEM simulation of a schulze ring shear tester. Proc. of the *6th international conference on micromechanics of granular media*, July 13–17, 2009, Golden (Colorado), p. 409–412.

Barletta, D., Donsi, G., *et al.* (2007a) Solid flow rate prediction in silo discharge of aerated cohesive powders. *AIChE Journal*, **53**(9), 2240–2253.

Barletta, D., Donsì, G., *et al.* (2007b) A rotational tester for the characterization of aerated shear flow of powders. *Particle and Particle Systems Characterization*, **24**(4–5), 259–270.

Barletta, D. and Poletto, M. (2012) Aggregation phenomena in fluidization of cohesive powders assisted by mechanical vibrations. *Powder Technology*, **225**, 93–100.

Barletta, D., Poletto, M. and Santomaso, A. C. (2019) Bulk powder flow characterisation techniques. In *Flow of dry particulates solids: theory, characterisation and applications* London (Hare, C., Hassanpour, A., and Pasha, M. Eds), Royal Society of Chemistry, London, Chapter 4.

Bashir, Z., Gu, H. and Yang, L. (2018) Evaluation of poly(ethylene terephthalate) powder as a material for selective laser sintering, and characterization of printed part. *Polymer Engineering & Science*, **58**(10), 1888–1900.

Behjani, M. A. *et al.* (2017) An investigation on process of seeded granulation in a continuous drum granulator using DEM. *Advanced Powder Technology*, **28**(10), 2456–2464.

Berretta, S. *et al.* Size, shape and flow of powders for use in Selective Laser Sintering (SLS). Proc. of *the 6th International Conference on Advanced Research and Rapid Prototyping*, October 1-5, 2013, Leiria (Portugal), p. 49–54.

Bertrand, P. *et al.* (2007) Ceramic components manufacturing by selective laser sintering. *Applied Surface Science*, **254**(4), 989–992.

Bhushan, B. and Caspers, M. (2017) An overview of additive manufacturing (3D printing) for microfabrication. *Microsystem Technologies*, **23**(4), 1117–1124.

Bindhumadhavan, G. *et al.* (2005) Roll compaction of a pharmaceutical excipient: Experimental validation of rolling theory for granular solids. *Chemical Engineering Science*, **60**(14), 3891–3897.

Bortolotti, C. T. *et al.* (2013) Hydrodynamic study of a mixture of west

132

Indian cherry residue and soybean grains in a spouted bed. *The Canadian Journal of Chemical Engineering*, **91**(11), 1871–1880.

Buist, K. A. *et al.* (2016) On an efficient hybrid soft and hard sphere collision integration scheme for DEM. *Chemical Engineering Science*, **153**, 363–373.

Buscombe, D. (2013) Transferable wavelet method for grain-size distribution from images of sediment surfaces and thin sections, and other natural granular patterns. *Sedimentology*, **60**(7), 1709–1732.

Cazelles, B. *et al.* (2008) Wavelet analysis of ecological time series. *Oecologia*, **156**(2), 287–304.

Chen, H. *et al.* (2017a) Flow behavior of powder particles in layering process of selective laser melting: Numerical modeling and experimental verification based on discrete element method. *International Journal of Machine Tools and Manufacture*, **123**, 146–159.

Chen, H. *et al.* (2017b) Flow behavior of powder particles in layering process of selective laser melting: Numerical modeling and experimental verification based on discrete element method. *International Journal of Machine Tools and Manufacture*, **123**, 146–159.

Chen, H. *et al.* (2020) Packing quality of powder layer during counter-rolling-type powder spreading process in additive manufacturing. *International Journal of Machine Tools and Manufacture*, **153**, 103553.

Chiang, P. H. *et al.* Forecasting of Solar Photovoltaic System Power Generation Using Wavelet Decomposition and Bias-Compensated Random Forest. Proc. of the *Ninth Annual IEEE Green Technologies Conference*, March 29-31, 2017, Colorado (USA), p. 260–266.

Chirone, R. *et al.* (2016) Bulk flow properties of sieved samples of a ceramic powder at ambient and high temperature. *Powder Technology*, **288**, 379–387.

Chirone, R. *et al.* (2018) A comparison between interparticle forces estimated with direct powder shear testing and with sound assisted fluidization. *Powder Technology*, **323**, 1–7.

Coetzee, C. (2020) Calibration of the discrete element method: Strategies for spherical and non-spherical particles. *Powder Technology*, **364**, 851–878.

Coetzee, C. J. (2017) Review: Calibration of the discrete element method. *Powder Technology*, **310**, 104–142.

Continuous Wavelet Transform and Scale-Based Analysis - MATLAB & Simulink - MathWorks Italia. https://it.mathworks.com/help/wavelet/gs/continuous-wavelet-transform-and-scale-based-analysis.html

Cundall, P. A. (1971) A computer Model for Simulating Progressive Large Scale Movements in Blocky System. Proc. of *the Int. Symp. on Rock Mechanics*, October 4-6, 1971, Nancy (France), p. 2-8

Cundall, P. A. and Strack, O. D. L. (1979) A discrete numerical model for granular assemblies. *Géotechnique*, **29**(1), 47–65.

References

Courtney Pratt, J. S. C. and Eisner, E. (1957) The effect of a tangential force on the contact of metallic bodies. Proc. of the *Royal Society of London. Series A. Mathematical and Physical Sciences*, **238**(1215), 529–550.

Danezan, A. *et al.* (2018) Selective laser sintering of porcelain. *Journal of the European Ceramic Society*, **38**(2), 769–775.

Dintwa, E., Tijskens, E. and Ramon, H. (2008) On the accuracy of the Hertz model to describe the normal contact of soft elastic spheres. *Granular Matter*, **10**, 209–221. Available at: www.biw.kuleuven.be/aee/amc/index.htm (Accessed: 30 April 2021).

Domo | Product Finder (no date). Available at: https://www.technyl.com/product-finder/SINTERLINE POWDER PA6 3400 HT 110 NATURAL/001463 (Accessed: 13 September 2021).

Escano, L. I. *et al.* (2018) Revealing particle-scale powder spreading dynamics in powder-bed-based additive manufacturing process by high-speed x-ray imaging. *Scientific Reports*, **8**(1), 1–11.

Van den Eynde, M., Verbelen, L. and Van Puyvelde, P. (2015) Assessing polymer powder flow for the application of laser sintering. *Powder Technology*, **286**, 151–155.

Favier, J. F. *et al.* (1999a) Shape representation of axi-symmetrical, non-spherical particles in discrete element simulation using multi-element model particles. *Engineering Computations (Swansea, Wales)*, **16**(4), 467–480.

Favier, J. F. *et al.* (1999b) Shape representation of axi-symmetrical, non-spherical particles in discrete element simulation using multi-element model particles. *Engineering Computations (Swansea, Wales)*.

Ferrari, M. (2014) *Analisi Wavelet del segnale di perfusione cutanea*. Master's thesis, Università degli studi di Padova.

Fina, F. *et al.* (2017) Selective laser sintering (SLS) 3D printing of medicines. *International Journal of Pharmaceutics*, **529**(1–2), 285–293.

Fouda, Y. M. and Bayly, A. E. (2020) A DEM study of powder spreading in additive layer manufacturing. *Granular Matter*, **22**, 10.

Foufoula-Georgiou, E. and Kumar, P. (1994) Wavelet Analysis in Geophysics: An Introduction. In *Wavelet Analysis and Its Applications* (Efi Foufoula-Georgiou, Praveen Kumar Eds.), Academic Press, Cambridge (USA), Book 4, p. 1-43.

Freeman, R. (2007) Measuring the flow properties of consolidated, conditioned and aerated powders - A comparative study using a powder rheometer and a rotational shear cell. *Powder Technology*, **174**(1–2), 25–33.

Fu, X. *et al.* (2012) Effect of particle shape and size on flow properties of lactose powders. *Particuology*, **10**(2), 203–208.

Goodridge, R. D., Tuck, C. J. and Hague, R. J. M. (2012) Laser sintering of polyamides and other polymers. *Progress in Materials Science*, **57**(2), 229–267.

Grima, A. P. and Wypych, P. W. (2011) Development and validation of calibration methods for discrete element modelling. *Granular Matter*, **13**,

134

127–132.

Haeri, S. *et al.* (2017) Discrete element simulation and experimental study of powder spreading process in additive manufacturing. *Powder Technology*, **306**, 45–54.

Haeri, S. (2017) Optimisation of blade type spreaders for powder bed preparation in Additive Manufacturing using DEM simulations. *Powder Technology*, **321**, 94–104.

He, Y. *et al.* (2020) A digital-based approach for characterising spread powder layer in additive manufacturing. *Materials and Design*, **196**, 109102.

He, Y., Hassanpour, A. and Bayly, A. E. (2021) Combined effect of particle size and surface cohesiveness on powder spreadability for additive manufacturing. *Powder Technology*, **392**, 191–203.

Hertz, H. (1881) Über die Berührung fester elastischer Körper. *Journal für die reine und angewandte Mathematik*, **92**, 156–171.

Hesse, R., Krull, F. and Antonyuk, S. (2021) Prediction of random packing density and flowability for non-spherical particles by deep convolutional neural networks and Discrete Element Method simulations. *Powder Technology*, **393**, 559–581.

Hsu, S.-H., Reklaitis, G. V and Venkatasubramanian, V. (2010) Modeling and Control of Roller Compaction for Pharmaceutical Manufacturing. Part I: Process Dynamics and Control Framework. *J Pharm Innov*, **5**, 14–23.

Islam, M. S., Pears, R. and Bacic, B. (2018) A wavelet approach for precursor pattern detection in time series. *Journal of Electrical Systems and Information Technology*, **5**(3), 337–348.

Jenike, W., A. (1959) On the Plastic Flow of Coulomb Solids beyond Original Failure. *Appl. Mech.*, **81**, 599–602.

Jenike, A. (1964) *Storage and Flow of Solids.* Bulletin No. 123. Utah Engineering Experiment Station, Utah (USA), Vol. 53, No. 26.

Ji, S. and Shen, H. H. (2006) Effect of Contact Force Models on Granular Flow Dynamics. *Journal of Engineering Mechanics*, **132**(11), 1252–1259.

Jia, X. *et al.* (2017) Evolution of world crude oil market integration and diversification: A wavelet-based complex network perspective. *Applied Energy*, **185**, 1788–1798.

Johanson, J. R. (1965) A Rolling Theory for Granular Solids. *Journal of Applied Mechanics*, **32**(4), 842.

Johnson, K. L., Kendall, K. and Roberts, A. D. (1971) Surface Energy and the Contact of Elastic Solids. *Proceedings of the Royal Society A: Mathematical, Physical and Engineering Sciences*, **324**(1558), 301–313.

Karkala, S. *et al.* (2019) Calibration of Discrete-Element-Method Parameters for Cohesive Materials Using Dynamic-Yield-Strength and Shear-Cell Experiments. *Processes*, **7**(5), 278.

Kompella, K. C. D., Mannam, V. G. R. and Rayapudi, S. R. (2016) DWT based bearing fault detection in induction motor using noise cancellation. *Journal of Electrical Systems and Information Technology*, **3**(3), 411–427.

References

Krantz, M., Zhang, H. and Zhu, J. (2009) Characterization of powder flow: Static and dynamic testing. *Powder Technology*, **194**(3), 239–245.

Kruth, J. P. *et al.* (2004) Selective laser melting of iron-based powder. *Journal of Materials Processing Technology*, **149**(1–3), 616–622.

Kumar, P. and Foufoula-Georgiou, E. (1997) Wavelet analysis for geophysical applications. *Reviews of Geophysics*, **35**(4), 385–412.

Lakes, R. (1987) Foam structures with a negative Poisson's ratio. *Science*, **235**, 1038–1041.

Lee, H. *et al.* (2017) Lasers in additive manufacturing: A review. *International Journal of Precision Engineering and Manufacturing - Green Technology*, **4**(3), 307–322.

Lee, Y. *et al.* (2020) Effect of Particle Spreading Dynamics on Powder Bed Quality in Metal Additive Manufacturing. *Integrating Materials and Manufacturing Innovation 2020 9:4*, **9**(4), 410–422.

Liang Deng, X. and Davé, R. N. (2013) Dynamic simulation of particle packing influenced by size, aspect ratio and surface energy. *Granular Matter*, **15**, 401–415.

Liu, S. and Shin, Y. C. (2019) Additive manufacturing of Ti6Al4V alloy: A review. *Materials and Design*, **164**, 107552.

Lumay, G. *et al.* (2012) Measuring the flowing properties of powders and grains. *Powder Technology*, **224**, 19–27.

Lupo, M. *et al.* (2019) Calibration of DEM Simulation of Cohesive Particles. *CHEMICAL ENGINEERING TRANSACTIONS*, **74**, 379–384.

Macrì, D. *et al.* (2017) Experimental and theoretical analysis of TiO2 powders flow properties at ambient and high temperatures. *Chemical Engineering Science*, **167**, 172–190.

Marchais, K. *et al.* (2021) A 3D DEM simulation to study the influence of material and process parameters on spreading of metallic powder in additive manufacturing. *Computational Particle Mechanics 2021 8:4*, **8**(4), 943–953.

Marigo, M. and Stitt, E. H. (2015) Discrete Element Method (DEM) for Industrial Applications: Comments on Calibration and Validation for the Modelling of Cylindrical Pellets. *KONA Powder and Particle Journal*, **32**, 236–252.

Markauskas, D. *et al.* (2010) Investigation of adequacy of multi-sphere approximation of elliptical particles for DEM simulations. *Granular Matter*, **12**, 107–123.

Medhe, M., Pitchumani, B and Tomas, J. (2005) Flow characterization of fine powders using material characteristic parameters. *Advanced Powder Technology*, **16**(2), 123–135.

Medhe, M., Pitchumani, B. and Tomas, J. (2005) Flow characterization of fine powders using material characteristic parameters. *Advanced Powder Technology*, **16**(2), 123–135.

Meier, C. *et al.* (2019) Critical influences of particle size and adhesion on the powder layer uniformity in metal additive manufacturing. *Journal of*

Materials Processing Technology, **266**, 484–501.

Mindlin, R. D. (1949) Compliance of Elastic Bodies in Contact. *Journal of Applied Mechanics*, **16**(3), 259–268

Mindlin, R. D. (1989) Compliance of Elastic Bodies in Contact. In *The Collected Papers of Raymond D. Mindlin Volume I* (Deresiewicz, H., Bieniek, M.P., Di Maggio Eds.), Springer-Verlag New York, p. 197-206.

Mindlin, R. D. and Deresiewicz, H. (1989) Elastic Spheres in Contact Under Varying Oblique Forces. In *The Collected Papers of Raymond D. Mindlin Volume I*, 269–286.

Misiti, M. *et al.* (1997) *Wavelet Toolbox^{TM} 4 User's Guide*. Available at: www.mathworks.com (Accessed: 9 March 2021).

Molerus, O. (1975) Theory of yield of cohesive powders. *Powder Technology*, **12**(3), 259–275.

Morse Wavelets - MATLAB & Simulink - MathWorks Italia. https://it.mathworks.com/help/wavelet/ug/morse-wavelets.html

Nan, W. *et al.* (2018) Jamming during particle spreading in additive manufacturing. *Powder Technology*, **338**, 253–262.

Nan, W. and Ghadiri, M. (2019) Numerical simulation of powder flow during spreading in additive manufacturing. *Powder Technology*, **342**, 801–807.

Nan, W., Pasha, M. and Ghadiri, M. (2020) Numerical simulation of particle flow and segregation during roller spreading process in additive manufacturing. *Powder Technology*, **364**, 811–821.

Nedderman, R. M. (1992) *Statics and Kinematics of Granular Materials.* Cambridge University Press, Cambridge (UK)

Ng, P. (2020) *Simulating particle packing during powder spreading for selective laser melted additive manufacturing using the discrete element method in abaqus.* Master's thesis, Faculty of California Polytechnic State University.

Ngo, T. D. *et al.* (2018) Additive manufacturing (3D printing): A review of materials, methods, applications and challenges. *Composites Part B: Engineering*, **143**, 172–196.

Niino, T. (2009) Effect of Powder Compaction in Plastic Laser Sintering Fabrication. *Solid Freeform Fabrication Symposium*, **12**, 193–205.

Obermayr, M. *et al.* (2014) A discrete element model and its experimental validation for the prediction of draft forces in cohesive soil. *Journal of Terramechanics*, **53**(1), 93–104.

Parrella, L. *et al.* (2008) Comparison between a Uniaxial Compaction Tester and a Shear Tester for the Characterization of Powder Flowability. *KONA Powder and Particle Journal*, **26**, 178–189.

Parteli, E. J. R. and Pöschel, T. (2016) Particle-based simulation of powder application in additive manufacturing. *Powder Technology*, **288**, 96–102.

Pasha, M. *et al.* (2016) Effect of particle shape on flow in discrete element method simulation of a rotary batch seed coater. *Powder Technology*, **296**, 29–

36.

Pavlov, A. N. *et al.* (2006) Application of wavelet-based tools to study the dynamics of biological processes. *Briefings in Bioinformatics*, **7**(4), 375–389.

Polanco-Martínez, J. M. and Faria, S. H. (2018) Estimation of the significance of the foster's wavelet spectrum by means of a permutation test and its application for paleoclimate records. *Boletin Geologico y Minero*, **129**(3), 549–564.

Polyamide 6 - Nylon 6 - PA 6.

https://www.azom.com/article.aspx?ArticleID=442 (Accessed: 13 January 2020).

Prescott, J. and Barnum, R. A. (2000) On powder flowability. *Pharmaceutical Technology*, **24**, 60–84.

Regenfuss, P. *et al.* (2004) Microparts by a novel modification of selective laser sintering. in *Technical Paper - Society of Manufacturing Engineers*.

Di Renzo, A. and Di Maio, F. P. (2004) Comparison of contact-force models for the simulation of collisions in DEM-based granular flow codes. *Chemical Engineering Science*, **59**(3), 525–541.

Di Renzo, A. and Paolo Di Maio, F. (2005) An improved integral non-linear model for the contact of particles in distinct element simulations. *Chemical Engineering Science*, **60**(5), 1303–1312.

Riley, G. S. and Mann, G. R. (1972) Effects of particle shape on angles of repose and bulk densities of a granular solid. *Materials Research Bulletin*, **7**(2), 163–169.

Roessler, T. and Katterfeld, A. (2019) DEM parameter calibration of cohesive bulk materials using a simple angle of repose test. *Particuology*.

Romaní Fernández, X. and Nirschl, H. (2013) Simulation of particles and sediment behaviour in centrifugal field by coupling CFD and DEM. *Chemical Engineering Science*, **94**, 7–19.

Roy, N. K. and Cullinan, M. A. μ-SLS of Metals: Design of the powder spreader, powder bed actuators and optics for the system. Proc. of *the 26th Annual International Solid Freeform Fabrication Symposium - an Additive Manufacturing Conference*, August 10-12, 2015, Texas (USA), p. 134–155.

Ruggi, D., Barrès, C., *et al.* (2020) A quantitative approach to assess high temperature flow properties of a PA 12 powder for laser sintering. *Additive Manufacturing*, **33**, 101143.

Ruggi, D., Lupo, M., *et al.* (2020) Flow properties of polymeric powders for selective laser sintering. *Powder Technology*, **370**(15), 288–297.

Rumpf, H. (1958) Grundlagen und Methoden des Granulierens. *Chemie Ingenieur Technik - CIT*, **30**(3), 144–158.

Rumpf, H. The strength of granules and agglomerates. Proc. of *the First International Symposium on Agglomeration,* Philadelphia (USA), 1962, p. 379–418.

Sakaguchi, H., Ozaki, E. and Igarashi, T. (1993) Plugging of the Flow of Granular Materials during the Discharge from a Silo. *International Journal of*

Modern Physics B, **07**, 1949–1963.

Salehi, H. *et al.* (2018) Experiments and simulation of torque in Anton Paar powder cell. *Particulate Science and Technology*, **36**(4), 501–512.

Scale-averaged wavelet spectrum - MATLAB scaleSpectrum - MathWorks Italia. https://it.mathworks.com/help/wavelet/ref/cwtfilterbank.scalespectrum.html?searchHighlight=wavelet power spectrum&s_tid=srchtitle.

Scale to frequency - MATLAB scal2frq - MathWorks Italia. https://it.mathworks.com/help/wavelet/ref/scal2frq.html.

Schmid, M. *et al.* (2014) Flowability of powders for Selective Laser Sintering (SLS) investigated by Round Robin Test. Proc. of *the 6th International Conference on Advanced Research and Rapid Prototyping*, October 1-5, 2013, Leiria (Portugal), p. 49–54.

Schmidt, J. *et al.* (2014) A novel process route for the production of spherical LBM polymer powders with small size and good flowability. *Powder Technology*.

Schueren, B. Van Der and Kruth, J. P. (1995) Powder deposition in selective metal powder sintering. *Rapid Prototyping Journal*, **1**(3), 23–31.

Schulze, D. (2010) Flow properties of powders and bulk solids (fundamentals). http://www.dietmar-schulze.de/grdle1.pdf.

Seville, J., Tüzün, U. and Clift, R. (1997) *Processing of Particulate Solids*. Springer, Dordrecht.

Sing, S. L. *et al.* (2017) Direct selective laser sintering and melting of ceramics: A review. *Rapid Prototyping Journal*, **23**(3), 611–623.

Snow, Z., Martukanitz, R. and Joshi, S. (2019) On the development of powder spreadability metrics and feedstock requirements for powder bed fusion additive manufacturing. *Additive Manufacturing*, **28**, 78–86.

Sofia, D., Barletta, D. and Poletto, M. (2018) Laser sintering process of ceramic powders: The effect of particle size on the mechanical properties of sintered layers. *Additive Manufacturing*, **23**, 215–224.

Streek, A. *et al.* Laser micro sintering - A quality leap through improvement of powder packing. Proc. of the *19th Annual International Solid Freeform Fabrication Symposium,* August 4-6, 2008, Texas (USA), p. 297-308.

Strondl, A. *et al.* (2015) Characterization and Control of Powder Properties for Additive Manufacturing. *JOM*, **67**, 549–554.

Sun, Y. Y. *et al.* (2015) Manipulation and Characterization of a Novel Titanium Powder Precursor for Additive Manufacturing Applications. *JOM*, **67**, 564–572.

Tang, H. H., Chiu, M. L. and Yen, H. C. (2011) Slurry-based selective laser sintering of polymer-coated ceramic powders to fabricate high strength alumina parts. *Journal of the European Ceramic Society*, **31**(8), 1383–1388.

Teffo, V. B. and Naudé, N. (2013) Determination of the coefficients of restitution, static and rolling friction of Eskom-grade coal for discrete element

modelling. *Journal of the Southern African Institute of Mining and Metallurgy*, **113**, 351–356.

Thornton, C. (2015) *Granular Dynamics, Contact Mechanics and Particle System Simulations: A DEM study*. Springer, Cham.

Tomasetta, I., Barletta, D. and Poletto, M. (2013) The High Temperature Annular Shear Cell: A modified ring shear tester to measure the flow properties of powders at high temperature. *Advanced Powder Technology*, **24**(3), 609–617.

Utela, B. *et al.* (2008) A review of process development steps for new material systems in three dimensional printing (3DP). *Journal of Manufacturing Processes*, **10**(2), 96–104.

Üzüm, M. (2015) *Metal polymer hybrids: Multiscale adhesion behaviour and polymer dynamics*. Master's thesis, Fakultät II- Mathematik und Naturwissenschaften der Technischen Universität Berlin.

Wang, D. *et al.* (2018) A hybrid wavelet de-noising and Rank-Set Pair Analysis approach for forecasting hydro-meteorological time series. *Environmental Research*, **160**, 269–281.

Wang, L. *et al.* (2015) Experimental determination of parameter effects on the coefficient of restitution of differently shaped maize in three-dimensions. *Powder Technology*, **284**, 187–194.

Wang, L. *et al.* (2018) Determination of the coefficient of rolling friction of an irregularly shaped maize particle group using physical experiment and simulations. *Particuology*, **38**, 185–195.

Wang, L. *et al.* (2020) Adhesion effects on spreading of metal powders in selective laser melting. *Powder Technology*, **363**, 602–610.

Wavelet Toolbox^{TM} 4 User's Guide. https://www.ltu.se/cms_fs/1.51590!/wavelet%20toolbox%204%20user's%20 guide%20(larger%20selection).pdf

Wei, L., Fwa, T. F. and Zhe, Z. (2005) Wavelet Analysis and Interpretation of Road Roughness. *Journal of Transportation Engineering*, **131**(2), 120–130.

Wensrich, C. M. and Katterfeld, A. (2012) Rolling friction as a technique for modelling particle shape in DEM. *Powder Technology*, **217**, 409–417.

Weon, J. Il (2009) Mechanical and thermal behavior of polyamide-6/clay nanocomposite using continuum-based micromechanical modeling. *Macromolecular Research*, **17**(10), 797–806.

Wilczek, M., Bertling, J. and Hintemann, D. (2004) Optimised technologies for cryogenic grinding. *International Journal of Mineral Processing*, **74**, S425–S434.

Williams, J. D. and Deckard, C. R. (1998) Advances in modeling the effects of selected parameters on the SLS process. *Rapid Prototyping Journal*, **4**, 90–100.

Wong, K. V. and Hernandez, A. (2012) A Review of Additive Manufacturing. *ISRN Mechanical Engineering*, **2012**, 1–10.

Wu, P., Wang, J. and Wang, X. (2016) A critical review of the use of 3-D

printing in the construction industry. *Automation in Construction*, **68**, 21–31.

Xiang, Z. *et al.* (2016) Simulation of Forming Process of Powder Bed for Additive Manufacturing. *Journal of Manufacturing Science and Engineering*, **138**(8), 081002.

Xu, H. *et al.* (2017) CFD-DEM study on cohesive particles in a spouted bed. *Powder Technology*, **314**, 377–386.

Yee, I. (2018) *Powder Bed Surface Quality and Particle Size Distribution for Metal Additive Manufacturing and Comparison with Discrete Element Model*. Master's thesis, California Polytechnic State University.

Zafar, U. *et al.* (2014) Drop test: A new method to measure the particle adhesion force. *Powder Technology*, **264**, 236–241.

Zhou, Y. C. *et al.* (1999) Rolling friction in the dynamic simulation of sandpile formation. *Physica A: Statistical Mechanics and its Applications*, **269**(2–4), 536–553.

Ziegelmeier, S. *et al.* (2015) An experimental study into the effects of bulk and flow behaviour of laser sintering polymer powders on resulting part properties. *Journal of Materials Processing Technology*, **215**(1), 239–250.

Nomenclature

a	: Contact radius	[m]
a_f	: Scale factor	[-]
A (Appendix A)	: Parameter defined in the appendix	[°]
Bo	: Bond number	[-]
Bo_1	: Bo number obtained by using $F_{int,1}$	[-]
Bo_2	: Bo number obtained by using $F_{int,2}$	[-]
C	: Cohesion	[Pa]
C_W	: Wavelet coefficient	[-]
C_0	: Cohesion in correspondence of zero consolidation	[Pa]
$d_{3,2}$	: Sauter mean diameter	[m]
$d_{4,3}$	: Volume mean diameter	[m]
D (Appendix A)	: Roller diameter	[m]
D_a	: Particle agglomerate diameter	[m]
$D_{a,1}$	: Particle agglomerate diameter obtained by using Bo_1	[m]

Nomenclature

$D_{a,2}$	: Particle agglomerate diameter obtained by using Bo_2	[m]
D_{10}	: Particle diameter corresponding to the 10th percentile of the cumulative particle size	[m]
D_{50}	: Particle diameter corresponding to the 50th percentile of the cumulative particle size	[m]
D_{90}	: Particle diameter corresponding to the 90th percentile of the cumulative particle size	[m]
e	: Coefficient of restitution	[-]
e_{P-G}	: Coefficient of restitution between the particles and the geometry	[-]
e_{P-P}	: Coefficient of restitution between the particles	[-]
E	: Young's Modulus	[Pa]
E_i, E_j	: Young's Modulus of each sphere in contact	[Pa]
E_{kin}	: Kinetic energy	[J]
$E_{kin,impact}$	: Kinetic energy at the impact	[J]

144

$E_{kin,rebound}$	: Kinetic energy after the collision	[J]
E^*	: Equivalent Young's Modulus	[Pa]
f	: Signal	[-]
f_c	: Unconfined yield strength	[Pa]
F (Appendix A)	: Coefficient of proportionality between RF and P_{m}	[-]
F_{int}	: Interparticle force	[N]
$F_{int,1}$	: Interparticle forces calculated from the Rumpf equation by by using $\sigma_{0,1}$	[N]
$F_{int,2}$	: Interparticle forces calculated from the Rumpf equation by by using $\sigma_{0,2}$	[N]
F_i^f	: Particle-fluid interaction force	[N]
F_{ij}^c	: Contact force due to interaction between the particle i and the nearby ones j or the wall	[N]
F_{ik}^{nc}	: Non-contact forces like van der Waals and electrostatic forces acting on particle i by particle k or the other possible forces	[N]

Nomenclature

F_{ij}^t	: Tangential force on particle i by particle j	[N]
F_{JKR}	: Normal elastic contact force according to the JKR model	[N]
F_n	: Normal contact force	[N]
F_n^{el}	: Elastic repulsive force between two perfectly elastic spherical objects in contact	[N]
F_n^d	: Normal viscous damping force	[N]
F_{nc}	: Pull-out force	[N]
$F_{N,total}$	: Total normal force exerted by the lid on the powder bed	[N]
$F_{pullout}$	: Pull-out force	[N]
F_t	: Tangential force	[N]
F_t^d	: Tangential damping force	[N]
F_t^{el}	: Tangential elastic force	[N]
g	: Acceleration due to the gravity	$[m \cdot s^{-2}]$
G	: Shear modulus	[Pa]
G_i, G_j	: Shear modulus of each sphere in contact	[Pa]
G^*	: Equivalent shear modulus.	[Pa]
h	: Height of image	[px]

146

h_0 (Appendix A)	: Half the roller gap	[m]
H	: Initial height of the powder bed	[m]
I_i	: Moment of inertia	[kg · m^2]
k	: Shifting factor	[-]
K (Appendix A)	: Compressibility factor	[-]
l	: Width of image	[px]
L	: Lower part of the image representing the portion of the powder layer analysed	
M	: Middle part of the image representing the portion of the powder layer analysed	
m_i	: Mass of particle i	[kg]
m_j	: Mass of particle j	[kg]
m^*	: Effective mass	[kg]
n	: Number of particles of the aggregate	[-]
P	: Compressive stress	[Pa]
P_{in} (Appendix A)	: Vertical feed pressure	[Pa]
P_m (Appendix A)	: Maximum horizontal pressure exerted by the rollers on the material	[Pa]
P_θ (Appendix A)	: Horizontal pressure between the rollers at position θ	[Pa]

Nomenclature

R	: Particle radius	[m]
RF (Appendix A)	: Roll-separating force	[N]
R_i, R_j	: Radius of each sphere in contact	[m]
R_{min}	: Minimum particle radius in the simulation	[m]
RT (Appendix A)	: Torque on each roller	[N · m]
R^*	: Equivalent radius	[m]
s (Appendix A)	: Twice the layer thickness and the roller gap	[m]
S (Appendix A)	: Upper surface of the powder element	[m^2]
S_n	: Normal stiffness	[N · m^{-1}]
S_t	: Tangential stiffness	[N · m^{-1}]
t	: Time	[s]
T	: Tensile stress	[Pa]
T_i	: Torque between two in-contact surfaces	[N · m]
$\mathcal{T}$ (Appendix A)	: Coefficient of proportionality between RT and P_m	[-]
U	: Upper part of the image representing the portion of the powder layer analysed	

148

v_i	: Velocity of particle i	$[m \cdot s^{-1}]$
$v_n^{\overrightarrow{rel}}$	: Normal component of the relative velocity	$[m \cdot s^{-1}]$
$v_t^{\overrightarrow{rel}}$	: Relative tangential velocity	$[m \cdot s^{-1}]$
v_{impact}	: Impact velocity	$[m \cdot s^{-1}]$
$v_{rebound}$	: Rebound velocity	$[m \cdot s^{-1}]$
V	: Scrolling velocity of the circular piston lid	$[m \cdot s^{-1}]$
V_a	: Volume of the particle aggregate	$[m^3]$
V_{Exp}	: Total volume of particles with a diameter within a specific range of values by using the experimental PSD	$[m^3]$
V_{Gauss}	: Total volume of particles with a diameter within a specific range of values by using the Gaussian distribution	$[m^3]$
V_p	: Volume of a single particle	$[m^3]$
V_{ps}	: Total volume of particles within the powder layer	$[m^3]$
V_S	: Scrolling velocity of the blade	$[m \cdot s^{-1}]$
V_{total}	: Total volume within the powder layer (particles plus voids)	$[m^3]$
W (Appendix A)	: Width of the roller	$[m]$

Nomenclature

W_p	: Particle weight	[kg]
x	: Spreading direction	[m]
x (Appendix A)	: Opposite direction to that of advancement of the roller	[m]
y	: Perpendicular direction with respect to the spreading direction in the same spreading plane	[m]
y (Appendix A)	: Direction along the layer thickness	[m]
z	: Vertical direction	[m]

Greek symbols

α	: Static angle of repose	[°]
α_N (Appendix A)	: Nip angle	[°]
α_O	: Overlap between two spheres	[m]
$\alpha_{O,f}$	: Overlap (negative) at which the contact breaks	[m]
α_{sim}	: Static angle of repose from the simulation	[°]
α_t	: Tangential overlap	[m]
β	: Damping parameter	[-]
γ_1, γ_2	: Surface free energies of the two spheres	$[J \cdot m^{-2}]$
$\gamma_{1,2}$	: Interface surface energy	$[J \cdot m^{-2}]$

150

Γ	: Interfacial Surface Energy (or work of adhesion)	$[\text{J} \cdot \text{m}^{-2}]$
Γ_{P-G}	: Interfacial adhesive surface between the particles and the geometries	$[\text{J} \cdot \text{m}^{-2}]$
Γ_{P-P}	: Interfacial adhesive surface energy between the particles	$[\text{J} \cdot \text{m}^{-2}]$
$\Gamma_{P-P,1}$	: Interface surface energy between the particles obtained from $F_{int,1}$	$[\text{J} \cdot \text{m}^{-2}]$
$\Gamma_{P-P,2}$	: Interface surface energy between the particles obtained from $F_{int,2}$	$[\text{J} \cdot \text{m}^{-2}]$
δ (Appendix A)	: Effective angle of internal friction	$[°]$
Δx (Appendix A)	: Infinitely small change in the variable x	$[\text{m}]$
Δt_R	: Rayleigh time	$[\text{s}]$
ε (Appendix A)	: Powder porosity	$[\text{-}]$
ε_{exp}	: Porosity within the powder bed obtained in the experiment	$[\text{-}]$
ε_{sim}	: Porosity within the powder bed obtained in the simulation	$[\text{-}]$
ε_0	: Powder voidage for the unconsolidated material	$[\text{-}]$
θ (Appendix A)	: Angular position of the powder with respect to the roller	$[°]$

151

Nomenclature

θ_{att} (Appendix A)	: Angle of attack of the powder on the roller	[°]
θ_{in} (Appendix A)	: Angular position at which feed pressure P_{in} is applied	[°]
θ_M	: Angle of rotation of the microscope around the y axis	[°]
θ_S	: Angle of sliding friction [°]	[°]
μ (Appendix A)	: Friction coefficient	[-]
μ_R	: Coefficient of rolling friction	[-]
$\mu_{R,P-G}$	: Coefficient of rolling friction between the particles and the geometry	[-]
$\mu_{R,P-P}$	: Coefficient of rolling friction between the particles	[-]
μ_S	: Coefficient of sliding friction	[-]
$\mu_{S,P-G}$	: Coefficient of sliding friction between the particles and the geometry	[-]
$\mu_{S,P-P}$	: Coefficient of sliding friction between the particles	[-]
ν	: Poisson's ratio	[-]
ν (Appendix A)	: Acute angle between the tangent to the roller surface and the direction of the major principal stress	[°]

152

ν_i, ν_j	: Poisson ratio of each sphere in contact	[-]
ρ_b	: Bulk density of the powder	$[kg \cdot m^{-3}]$
$\rho_{b,exp}$	: Bulk density of the powder bed from the experiment	$[kg \cdot m^{-3}]$
$\rho_{b,sim}$	: Bulk density of the powder bed from the simulation	$[kg \cdot m^{-3}]$
ρ_{layer}	: Layer density	$[kg \cdot m^{-3}]$
ρ_m	: Material density of the polymer	$[kg \cdot m^{-3}]$
ρ_P	: Packing density	$[kg \cdot m^{-3}]$
$\rho_{P,max}$	: Maximal packing density	$[kg \cdot m^{-3}]$
ρ_p (Appendix A)	: Particle density $[kg/m^3]$	$[kg \cdot m^{-3}]$
ρ_s	: Density of the solid	$[kg \cdot m^{-3}]$
ρ_{tap}	: Tapped density	$[kg \cdot m^{-3}]$

Nomenclature

ρ_α (Appendix A)	: Bulk density evaluated in correspondence of $\theta = \alpha$	$[kg \cdot m^{-3}]$
ρ_θ (Appendix A)	: Bulk density evaluated at a generic angle θ	$[kg \cdot m^{-3}]$
σ (Appendix A)	: Mean normal stress	$[Pa]$
σ_D	: Standard deviation of particle size distribution	$[m]$
$\sigma_{H,x}$ (Appendix A)	: Horizontal normal stress acting on the powder element at x	$[Pa]$
$\sigma_{H,x+\Delta x}$ (Appendix A)	: Horizontal normal stress acting on the powder element at $x + \Delta x$	$[Pa]$
$\sigma_{H,0}$ (Appendix A)	: Horizontal normal stress at $x = 0$	$[Pa]$
σ_V (Appendix A)	: Vertical stress	$[Pa]$
σ_w (Appendix A)	: Wall normal stress	$[Pa]$
σ_0	: Isostatic tensile strength of the unconsolidated material	$[Pa]$
σ_0 (Appendix A)	: Mean normal stress at $x = 0$	$[Pa]$
$\sigma_{0,1}$	: Isostatic tensile strength of the unconsolidated material, evaluated according to the eq. (32)	$[Pa]$

$\sigma_{0,2}$	: Isostatic tensile strength of the unconsolidated material, evaluated according to the eq. (33)	[Pa]
σ_1	: Major principal stress	[Pa]
σ_2 (Appendix A)	: Minor principal stress	[Pa]
σ_α (Appendix A)	: Mean normal stress in correspondence of the nip angle	[Pa]
$\sigma_{\alpha,sim}$	: Standard deviation of the static angle of repose from the simulation	[°]
σ_θ (Appendix A)	: Mean normal stress along the radial direction	[Pa]
Σ (Appendix A)	: Half the lateral surface of the powder element	[m^2]
τ	: Shear stress	[Pa]
τ_w (Appendix A)	: Wall shear stress	[Pa]
ϕ_i	: Static angle of internal friction	[°]
ϕ_{i0}	: Static angle of internal friction in correspondence of zero consolidation	[°]
ϕ_{st}	: Slope angle of the linearized DYL	[°]
ϕ' (Appendix A)	: Angle of wall friction	[°]
Ψ	: Wavelet function	[-]

Nomenclature

ω (Appendix A)	: Angular velocity of the roller	$[\text{rad} \cdot \text{s}^{-1}]$
ω_a	: Frequency	$[\text{s}^{-1}]$
ω_i	: Angular velocity of particle i	$[\text{rad} \cdot \text{s}^{-1}]$
$\widehat{\omega_i}$	: Unit angular velocity of particle i	$[\text{-}]$
ω_w	: Center frequency of the wavelet	$[\text{s}^{-1}]$

Acronyms

AM	: Additive Manufacturing	
AOR	: Static Angle of Repose	$[°]$
AR	: Aspect ratio	
CE	: Equivalent circle diameter	$[\text{m}]$
CT	: Collection Tray	
CWT	: Continuous Wavelet Transform	
DEM	: Discrete Element Method	
DRA	: Dynamic repose angle	$[°]$
DT	: Deposition tray	
DYL	: Dynamic Yield Locus	
FF	: Flow Factor	$[\text{-}]$
HR	: Hausner Ratio	$[\text{-}]$
JKR	: Johnson-Kendall-Roberts	
L	: Lower part of the image	

156

M	: Middle part of the image	
MFR	: Mass flow rate of the powder	$[kg \cdot s^{-1}]$
PA6	: Domo's Sinterline unfilled polyamide 6 3400 HT110 Natural	
PA12	: Polyamide 12	
PR	: Packing Ratio	[-]
PS	: Power spectrum	
PSD	: Particle Size Distribution	
P1	: Plate which supports the deposition plate	
P2	: Deposition plate	
SEM	: Scanning Electron Microscopy	
SLM	: Selective Laser Melting	
SLS	: Selective Laser Sintering	
TPU	: Thermoplastic polyurethane	
T1	: First tray in the simulation	
T2	: Deposition tray in the simulation	
U	: Upper part of the image	
UYS	: Unconfined Yield Strength	[Pa]
VER	: Volume Expansion Ratio	[-]

Appendices

Appendix A: Johanson's rolling theory for granular solids

A.1   The Johanson's model

Granulation is the process by which powder particles can adhere to form larger, multiparticle aggregates called granules (Hsu, Reklaitis and Venkatasubramanian, 2010). This process can be useful because prevents segregation of the constituents of the powder mixture and improves the flow properties of the mixture. During roller compaction (Figure A.1), the powder is continuously fed to the roller compactor through one or two augers. The roller compactor is made of two rotating rollers, by which the powder is compressed to form a ribbon. Afterwards, the ribbon is milled and sieved to produce granules.

Appendix A
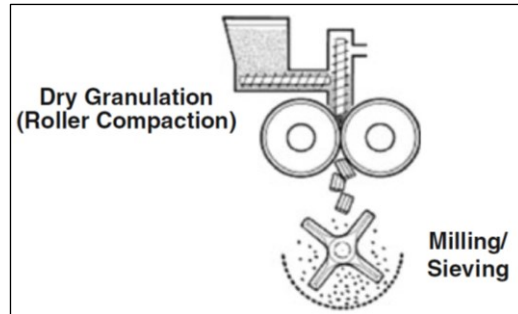
Figure A.1 *Dry granulation process.*

A model which provides relationships among the material properties, the press dimensions and the operating conditions is the Johanson's rolling theory for granular materials (Johanson, 1965). According to the model, the material is isotropic, frictional, cohesive, compressible and obeys the effective yield locus (Figure A.2) proposed by Jenike and Shield (Jenike, W., 1959).
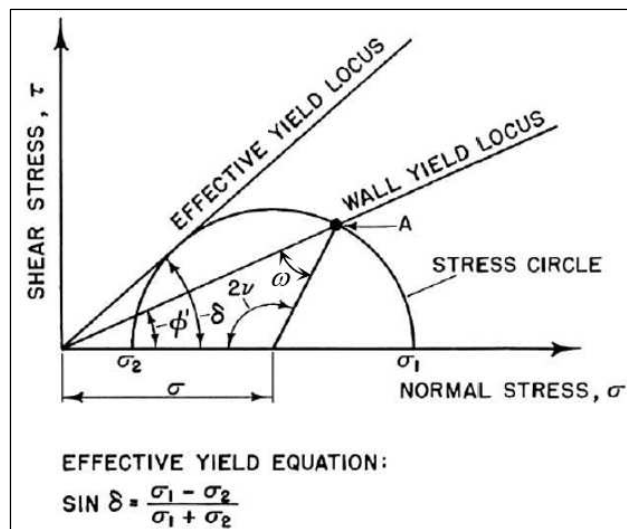
Figure A.2 Jenike–Shield yield criterion. ϕ' is the angle of wall friction, δ is the effective angle of internal friction and ν is the acute angle between the tangent to the roller surface and the direction of the major principal stress, σ_1 (Johanson, 1965).

The relationship between the tangential and the normal stresses at the roller surface is given by the wall yield locus (Figure A.2) which is described by the angle of wall friction ϕ'.

Johanson's rolling theory is useful to predict the stress distribution, which can be used to evaluate the roller force and torque and therefore to design and

160

simulate the process. This model was validated by Bindhumadhavan et al. (Bindhumadhavan *et al.*, 2005). According to the Johanson's theory, the material passes through two different regions: the slip and the nip region (Figure A.3). The angle α_N, called nip angle, defines the transition from the slip region, for $\theta > \alpha_N$, in which the rollers move faster than the material, to the nip region, for $\theta < \alpha_N$, in which there is no relative motion between the granular material and the rollers.
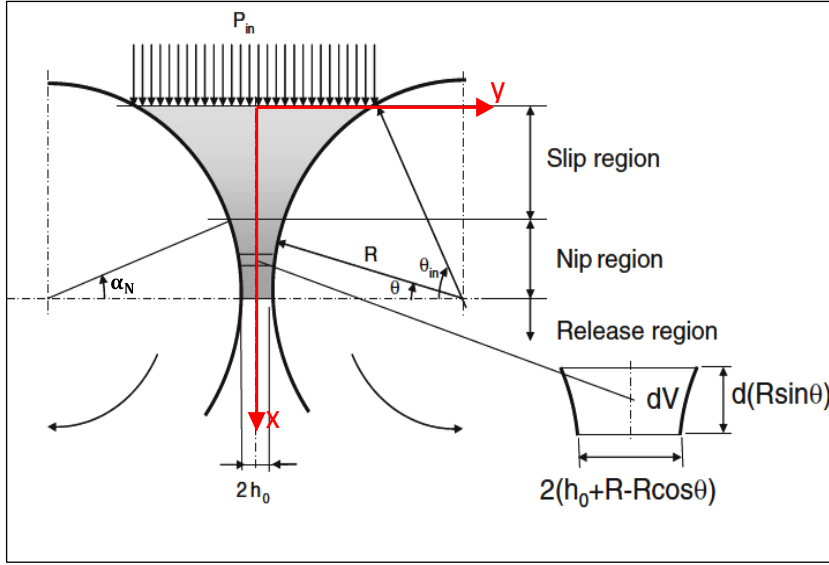
Figure A.3 *Johanson's rolling theory* (Hsu, Reklaitis and Venkatasubramanian, 2010).

By combining the yield locus with the equilibrium equations, Johanson obtained a system of partial hyperbolic differential equations, which he solved by using appropriate boundary conditions. As a result, in the slip region the mean normal stress (σ) gradient is given by the following relationship:

$$\left(\frac{d\sigma}{dx}\right)_{slip} = \frac{4\sigma\left(\frac{\pi}{2} - \theta - \nu\right)\tan\delta}{\frac{D}{2}\left[1 + \frac{S}{D} - \cos\theta\right]\left[\cot(A - \mu) - \cot(A + \mu)\right]} \tag{A.1}$$

where:

- $\sigma = \frac{\sigma_1 + \sigma_2}{2}$, is the mean normal stress in the granular solid;
- θ is the angular position at the surface of a roller (Figure A.3), such that $\theta = 0$ corresponds to the minimum gap;

161

Appendix A

- v (Figure A.2) is the acute angle between the tangent to the roller surface and the direction of the major principal stress σ_1. It is given by: $2v = \pi - sin^{-1}\frac{sin\,\phi'}{sin\,\delta} - \phi'$;
- $s = 2\,h_0$ is the roller gap and D is the roller diameter;
- A is a parameter, defined as follows: $A = \frac{\theta+v+\frac{\pi}{2}}{2}$;
- μ is the friction coefficient, that is: $\mu = \frac{\pi}{4} - \frac{\delta}{2}$

Johanson assumes that the normal stresses do not change along the layer thickness, i.e. in the y-direction (Figure A.3).

For the nip region, Johanson applied a simplified material model. He assumed that no slip occurred along the roller surface and the granular material is compressed to form a compact ribbon with a thickness equal to the gap between the rollers. For smooth rollers, the mean normal stress at any $\theta < \alpha_N$, is related to the mean normal stress at the nip angle σ_α by the following relationship between stress and density:

$$\sigma = \sigma_\alpha \left[\frac{\rho_\theta}{\rho_\alpha}\right]^K = \sigma_\alpha \left\{\frac{\left[1 + \left(\frac{s}{D}\right) - \cos\alpha_N\right]\cos\alpha_N}{\left[1 + \left(\frac{s}{D}\right) - \cos\theta\right]\cos\theta}\right\}^K \tag{A.2}$$

where: K is the compressibility factor, which is determined from the slope of logarithmic plot of the bulk density of the powder as a function of the mean normal stress in uniaxial compaction; ρ_θ is the bulk density evaluated at a generic angle θ and ρ_α is the bulk density evaluated in correspondence of $\theta = \alpha$.

The main normal stress gradient in the nip region is given by:

$$\left(\frac{d\sigma}{dx}\right)_{nip} = K\,\frac{\sigma\left[2\cos\theta - 1 - \left(\frac{s}{D}\right)\right]\tan\theta}{\left(\frac{D}{2}\right)\left\{\left[1 + \left(\frac{s}{D}\right) - \cos\theta\right]\cos\theta\right\}} \tag{A.3}$$

According to Johanson, in correspondence of the nip angle there is the coincidence between the mean normal stress gradient of the slip region and that of the nip region. Therefore:

$$\left(\frac{d\sigma}{dx}\right)_{slip} = \left(\frac{d\sigma}{dx}\right)_{nip} \tag{A.4}$$

Therefore, the nip angle is the angular position by which the curves (Figure A.4), corresponding to both gradients, intersect. The nip angle can be derived by solving the previous equality, that is:

$$\frac{4\left[\left(\frac{\pi}{2}\right)-\alpha_N-\nu\right]\tan\delta}{[\cot(A-\mu)-\cot(A+\mu)]} = K\,\frac{\left[2\cos\alpha_N-1-\left(\frac{S}{D}\right)\right]\tan\alpha_N}{\cos\alpha_N} \tag{A.5}$$

Therefore, α_N depends on the compressibility factor, the roller diameter, the gap and on the material flow properties, i.e. the effective angle of internal friction and the angle of wall friction.
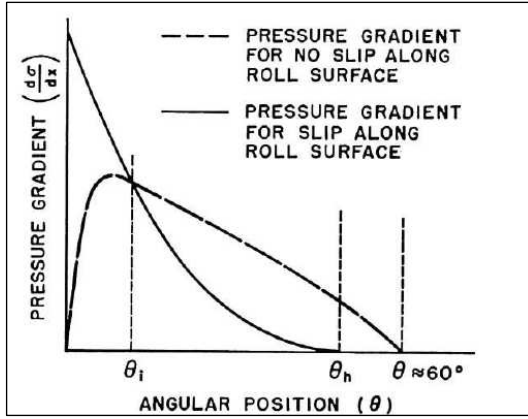
Figure A.4 *Main normal stress gradient as function of the angular position* (Johanson, 1965).

When the pressure distribution between the rollers is known, the resulting roll-separating force (RF), namely the force applied to the rollers in horizontal direction, can be evaluated as:

$$RF = \int_{\theta=0}^{\theta=\theta_{in}} P_\theta\,W\,\frac{D}{2}\,\cos\theta\;d\theta \tag{A.6}$$

where θ_{in} is the angular position at which feed pressure P_{in} is applied, W is the width of the roller, and P_θ is the horizontal pressure between the rollers at position θ, that is:

$$P_\theta = \sigma_\theta(1 + \sin\delta) \tag{A.7}$$

where σ_θ is the mean normal stress at position θ.

Therefore P_θ corresponds to the major principal stress, σ_1, at position θ.

Often the pressure in the slip region ($\theta > \alpha_N$) is negligible compared with the pressure in the slip region. Consequently, the roll force can be approximated to:

$$RF = P_m\,F\,W\,\frac{D}{2} \tag{A.8}$$

163

where F is:

$$F = \int_{\theta=0}^{\theta=\alpha_N} \left\{ \frac{\left[\left(\frac{S}{D} \right) \right]}{\left[1 + \left(\frac{S}{D} \right) - \cos\theta \right] \cos\theta} \right\}^K \cos\theta \; d\theta \qquad (A.9)$$

and P_m is the maximum horizontal pressure exerted by the rollers on the material.

The torque (RT) on each roller can be evaluated in a similar way. Therefore:

$$RT = P_m \; \mathcal{T} \; W \; \frac{D^2}{8} \qquad (A.10)$$

where $\mathcal{T}$ is:

$$\mathcal{T} = \int_{\theta=0}^{\theta=\alpha_N} \left\{ \frac{\left[\left(\frac{S}{D} \right) \right]}{\left[1 + \left(\frac{S}{D} \right) - \cos\theta \right] \cos\theta} \right\}^K 2 \; \sin\theta \cos\theta \; d\theta \qquad (A.11)$$

The maximum amount of deformation of the granular solid, thereby the maximum thickness reduction is determined by RF, RT, the roller diameter and width, the material flow properties, and the mechanical strength of the rolled material.

Low roller diameter results in low roller contact area and consequently in low value of the RF and the RT required for achieving a certain thickness reduction.

Johanson's model can also be applied when there are one fixed and one movable roller (Hsu, Reklaitis and Venkatasubramanian, 2010) .

A.2　　　　Application of the Johanson's theory

As has been said in the paragraph I.1.5, to obtain sufficient flowability during the spreading step in the SLS process, powders need to be properly engineered, for example, by adding flow promoters (Bashir, Gu and Yang, 2018) or by improving the particle shape, generally using high sphericity particles. These actions increase the cost of the SLS powder. Rather than improve the powder itself, a possible solution could be to compress the powder with a roller. In so doing, a normal force is added to the particle weight in order to counteract the inter-particle cohesive force. To compact powder

could lead to the increase of the layer density and thus to better mechanical properties (Niino, 2009; Ziegelmeier *et al.*, 2015) and surface finishing of the produced parts (Goodridge, Tuck and Hague, 2012). Moreover, by employing this strategy, cheaper powders could be used.

To understand the feasibility of the compaction applied to powders spread in the SLS process, the Johanson's model has been applied with some modifications to the compaction of powders to form denser layers. In this case the powder is not confined between two rollers but it is compressed by a roller against the deposition tray (Figure A.5). However, the same assumptions about the material, used by Johanson in case of the granulation process, are considered in the compaction in the SLS process.
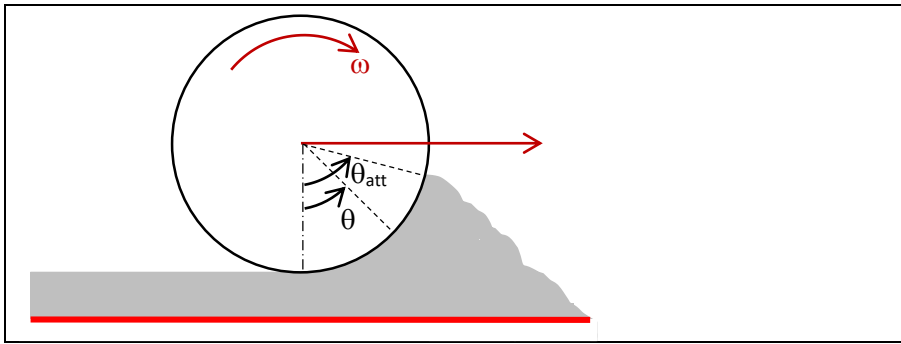

Figure A.5 *Roller compaction.* θ_{att} *is the angle of attack that is the angular position at which the powder (in gray in the figure) starts to touch the roller. The red line corresponds to the bottom of the tray. ω is the rotational speed of the roller and the red arrow is the advancement direction of the roller.*

In the Johanson's model for the granulation process, the shear stress on the powder at the centreline is zero because of the symmetry of the problem (Figure A.3). In case of compaction of the powder between the roller and the deposition tray in the SLS process, the layer thickness is like it is half the thickness (Figure A.6) of the powder in the case of the compaction between two rollers in the granulation process (Figure A.3). Therefore, the tray of Figure A.6, represented as a red line, is located in correspondence of an ideal centreline between two rollers as in Figure A.3. In Figure A.6, to show the resemblance of the compaction between the roller and the deposition tray with that between the two rollers, the other roller is represented faded because it does not exist in reality.

Since the powder element deforms because of the compression, there should be a shear stress on the tray (red line). But since small angles of attack of the powder on the roller will be used in order to minimise the rolling force and consequently to avoid too high shear stresses on the deposited layer, which may cause its entrainment by the roller, the shear stress of the powder

at the tray level ($y = 0$) is considered equal to zero during the whole compaction, namely between the angle of attack and $\theta = 0°$. By doing this assumption, the problem is exactly as the one proposed by Johanson (Johanson, 1965), where no shear stress is considered at the centreline.

However, the maximum error in the assessment of the shear stress corresponds to the value of the stress at $\theta = 0°$, where the compaction (σ_w) reaches its maximum value, namely:

$$\tau_w(\theta = 0°) = tan\,\phi' \cdot \sigma_w(\theta = 0°) \tag{A.12}$$

where ϕ' is the angle of wall friction and σ_w is the wall normal stress, that, in this case, is the vertical stress or the major principal stress (Nedderman and Cambridge University Press., 1992).

Contrary to the original Johanson's model for which the vertical stress is considered uniform along the layer thickness, i.e. in y-direction (Figure A.3), actually the compression of the powder between the roller and the deposition tray could lead to a profile of the stress along the layer thickness. In fact, the portion of the layer close to the deposition tray could be less compressed than the portion closer to the roller surface. As a result, the lower part of the powder layer could have lower strength compared to the adhesion of the portion of the layer in contact with the roller surface. Consequently, the powder could be dragged by the roller for $\theta < 0°$, namely when the roller comes up after the whole compression of the layer. This phenomenon could cause the formation of a poor-quality layer and must be avoided.

The force balance in x-direction on a differential powder element (Figure A.6) is:

$$\left(\sigma_{H,x} - \sigma_{H,x+\Delta x}\right) \frac{\Sigma}{2} + \tau_w\,S - \sigma_\theta\,S = 0 \tag{A.13}$$

where:
- $\sigma_{H,x}$ is the horizontal normal stress acting on the powder element at x (Figure A.6). It corresponds to the minor principal stress, according to the Johanson's model;
- $\sigma_{H,x+\Delta x}$ is the horizontal normal stress acting on the powder element at $x + \Delta x$;
- $\frac{\Sigma}{2}$ is the lateral surface of the powder element. It is defined as follows:

$$\frac{\Sigma}{2} = \left[\frac{s}{2} + \frac{D}{2}\,(1 - cos\,\theta)\right] W \tag{A.14}$$

where $s/2$ is the layer thickness, D is the roller diameter and W is the roller width;

- τ_w is the wall shear stress on the powder element;
- σ_θ is the normal stress along the radial direction;
- S is the upper surface of the powder element. It is defined as:

$$S = \frac{1}{\cos\theta} \, W \, \Delta x \tag{A.15}$$
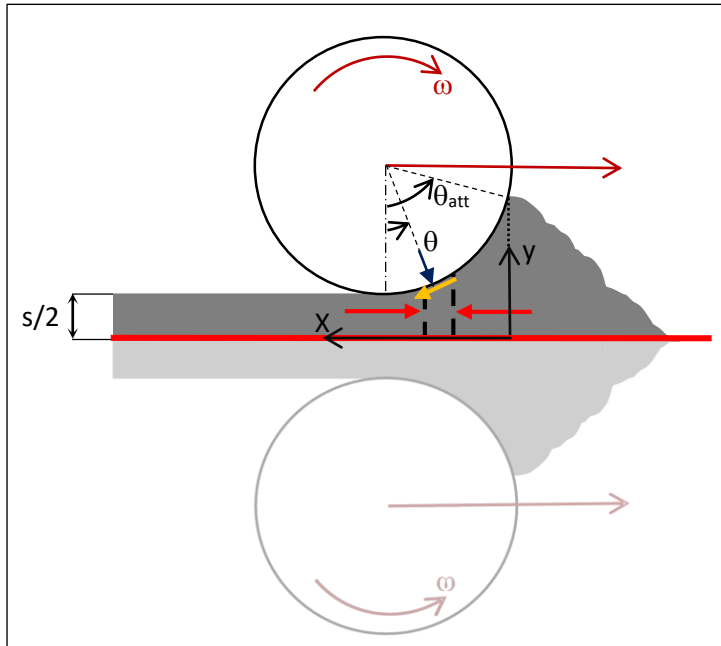
Figure A.6 *Stress on the differential powder element. Red, blue and yellow arrows correspond to horizontal, radial normal stresses and wall shear stress, respectively. The faded part of the figure is a way to show the resemblance to the original Johanson's model applied to the granulation process. The red line corresponds to the centreline of the original Johanson's model.*

The relationship between τ_w and σ_H is (Figure A.2):

$$\tau_w = \frac{\sigma_H}{1 - \sin\delta} \, [\sin\delta \; \sin(\pi - 2\nu)] \tag{A.16}$$

where σ_H is assumed to be coincident with σ_2, and τ_w corresponds to point A in Figure A.2.

Appendix A

σ_θ is related to σ_H as follows:

$$\sigma_\theta = \frac{\sigma_H}{1 - \sin\delta} \left[1 + \sin\delta \, \cos(\pi - 2\nu)\right] \tag{A.17}$$

where: $\omega + \phi' = \pi - 2\nu$.
By replacing eqs. (A.14) - (A.17) in eq. (A.13) and as $\Delta x \to 0$ we have:

$$\left(\frac{d\sigma_H}{dx}\right)_{slip} =$$
$$\frac{\left\{\sigma_H \, \tan\theta + \frac{\sigma_H}{1 - \sin\delta}\{[\sin\delta \, \sin(\pi - 2\nu)] - \tan\theta \, [1 + \sin\delta \, \cos(\pi - 2\nu)]\}\right\}}{\frac{D}{2}\left[\frac{S}{D} + 1 - \cos\theta\right]} \tag{A.18}$$

with the boundary condition (BC):
$$x = \frac{D}{2}\left(\sin\theta_{att} - \sin\theta\right) = 0 \qquad \sigma_H = \sigma_{H,0}$$
where θ_{att} is the initial angle of attack of the powder on the roller surface.

The mean normal stress is related to the horizontal stress, as follows:

$$\sigma = \frac{\sigma_H}{1 - \sin\delta} \tag{A.19}$$

Therefore, if we assume that δ changes very little with x, we have:

$$\left(\frac{d\sigma}{dx}\right)_{slip} = \tag{A.20}$$
$$\frac{\left\{\sigma \, \tan\theta + \frac{\sigma}{1 - \sin\delta}\{[\sin\delta \, \sin(\pi - 2\nu)] - \tan\theta \, [1 + \sin\delta \, \cos(\pi - 2\nu)]\}\right\}}{\frac{D}{2}\left[\frac{S}{D} + 1 - \cos\theta\right]}$$

with BC:
$$x = \frac{D}{2}\left(\sin\theta_{att} - \sin\theta\right) = 0 \qquad \sigma = \sigma_0$$
and

$$\sigma_V = \sigma_1 = \sigma\left(1 + \sin\delta\right) \tag{A.21}$$

where σ_V is the vertical stress, that is the normal stress along the y axis, and which corresponds to the major principal stress.
Therefore, RF is:

$$RF = \int_{\theta=0}^{\theta=\theta_{att}} \sigma_V(\theta) \, W \, \frac{D}{2} \, \cos\theta \, d\theta \tag{A.22}$$

168

To properly assess RF, it is necessary to find the condition by which the nip angle is equal to zero. In fact, the aim is to compress the powder trying to avoid the nip region which may cause the layer dragging.

The nip angle is the angle for which the following equality is satisfied.

$$\left(\frac{d\sigma}{dx}\right)_{slip} =$$

$$\frac{\left\{\tan\theta + \frac{1}{1-\sin\delta}\{[\sin\delta\ \sin(\pi-2\nu)] - \tan\theta\ [1+\sin\delta\ \cos(\pi-2\nu)]\}\right\}}{\frac{D}{2}\left[\frac{s}{D}+1-\cos\theta\right]} = \quad\quad (A.23)$$

$$K\ \frac{\left[2\cos\theta - 1 - \left(\frac{s}{D}\right)\right]\ \tan\theta}{\left(\frac{D}{2}\right)\left\{\left[1+\left(\frac{s}{D}\right)-\cos\theta\right]\ \cos\theta\right\}} = \left(\frac{d\sigma}{dx}\right)_{nip}$$

A.2.1 *Materials*

The materials which were considered for the application of the Johanson's model to the compaction of the powder layer in the SLS process are reported in Table A.1.

Table A.1 *Material properties of silica sand and magnesium carbonate (Barletta, Donsì, et al., 2007b): $d_{4,3}$ is the particle volume mean diameter, δ is the effective angle of internal friction, K is the compressibility factor, ϕ' is the angle of wall friction; α_N is the nip angle; ρ_p is the particle density; f_c is the unconfined yield strength; ε is the powder porosity.*

Material	$d_{4,3}$ (μm)	δ (°)	K	ϕ' (°)	α_N (°)	f_c (Pa)	ρ_p (kg m^{-3})	ε (-)
Silica	28	51	8.64	21.8	10.7	50	2650	0.69
Magnesium Carbonate	17	44.4	6.97	24.75	11.3	100	2600	0.71

The values of δ and ϕ' have been obtained as an average value among those obtained by Barletta et al. (Barletta, Donsì, *et al.*, 2007b) for different values of σ_1 in conditions of no aeration. The compressibility factor has been inferred from the values of σ_1 and the corresponding bulk densities, according the relation (A.2). The low values of K demonstrate that these powders are compressible and therefore suitable to be compressed by the roller. The unconfined yield strength has been evaluated as the extrapolation of f_c at $\sigma_1 = 0$ (Barletta, Donsì, *et al.*, 2007b).

A.2.2 *Results and discussion*

The eq. (A.20) is different from that obtained by Johanson, that is eq. (A.1). For the slip region, Johanson reported the sine of the angular position as a function of the logarithm of the ratio between the mean normal stress and the

mean normal stress in correspondence of the application of the feed pressure (Johanson, 1965), where the mean normal stress has been obtained by eq. (A.1). If the functions, obtained from eqs. (A.1) and (A.20), are reported on the same chart (Figure A.7) by using the same boundary condition, powder properties, D and layer thickness, the two plots turn out to be very similar, except for low angular positions, where they differ a bit. The plots have been obtained by considering the properties for silica powders (Table A.1) with $D = 5$ cm, $s/2 = 100$ µm and the boundary condition: $\sigma_{H,0} = \sigma_H(x = 0, \theta = \theta_{att} = 10°) = f_c$. Contrary to the granulation process in which there is a vertical feed pressure, which is a known variable, in case of the compaction of the powder layer in the SLS process, the horizontal stress is not known because the powder is simply deposited in front of the roller in a loose condition. Therefore, the horizontal stress in correspondence of the angle of attack of the powder on the roller and consequently the vertical stress at the inlet between the two rollers has been set equal to the unconfined yield strength. In fact, the powder, before being compressed, is not confined and not consolidated.
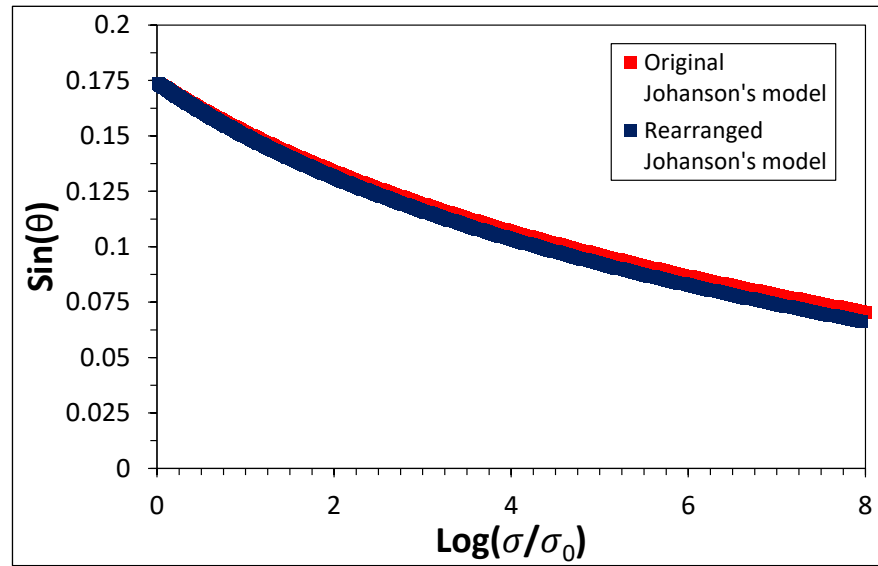

Figure A.7 *Comparison between the pressure distribution from eq. (A.1) obtained in the original Johanson's model (red squares) (Johanson, 1965) and the pressure distribution obtained from eq. (A.20) (blue squares).*

If the values of δ, K and ϕ', reported in Table A.1, as well as $D = 5$ cm and $s/2 = 100$ µm are used, $\alpha_N = 10.7°$ for silica and $\alpha_N = 11.3°$ for magnesium carbonate are obtained. $s/2 = 100$ µm is a typical value of powder layer thickness in the conventional SLS process.

Roll-separating force can be calculated once the σ_1 profile is known.

σ_1 profile along the angular position, for different angles of attack of the powders on the roller, can be obtained from eq. (A.20) for the slip region and from eq. (A.3) for the nip region given that σ_1 is related to σ as follows:

$$\sigma_1 = \sigma(1 + \sin\delta) \qquad\qquad\qquad (A.24)$$

If $\sigma_{H,0} = \sigma_H(x = 0, \theta = \theta_{att}) = f_c$ is considered as the boundary condition and the values of δ, K and ϕ' from Table A.1 and $D = 5\ cm$, $s/2 = 100\ \mu m$ are used, then the σ_1 profiles for silica and magnesium carbonate are those reported in Figure A.8.
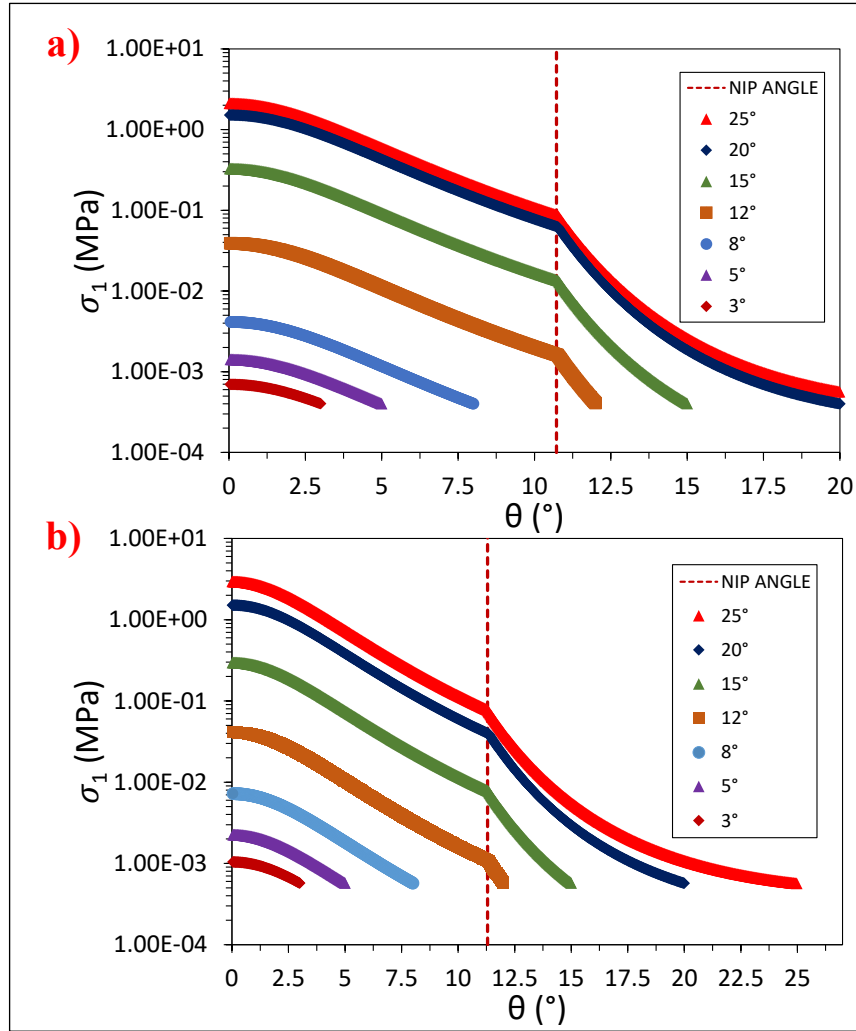

Figure A.8 *Major principal stress as a function of the angular position for different values of the angle of attack for: a) silica, b) magnesium*

171

carbonate, if the values, reported in Table A.1, are used, with $D = 5$ cm, $s/2 = 100$ µm and $\sigma_{H,0} = f_c$. The hyphenated red line corresponds to the nip angle.

The maximum vertical stress exerted on the powder is σ_1 at $\theta = 0°$. The value of this stress for each considered angle of attack is reported in Figure A.9 for silica and magnesium carbonate.
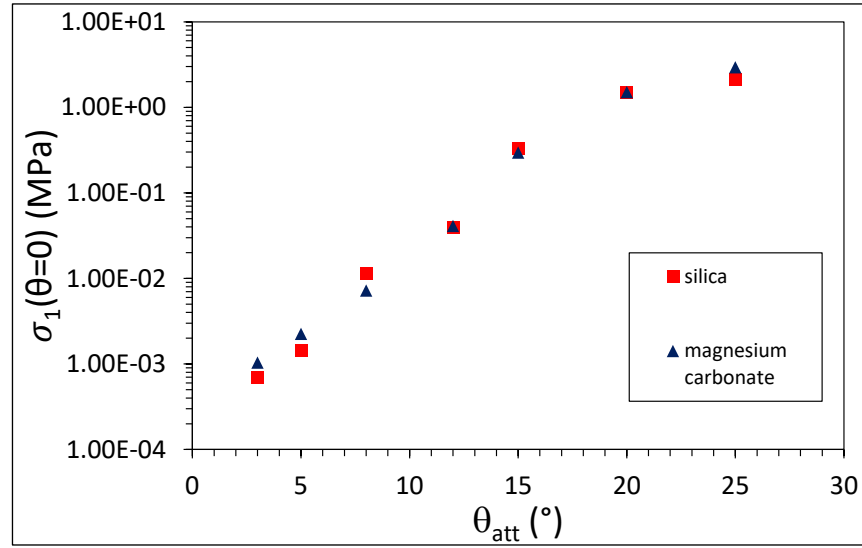

Figure A.9 *Major principal stress at $\theta = 0$ for different values of θ_{att} for:* ■ *silica,* ▲ *magnesium carbonate.*

The corresponding values of the roll-separating force, if the roller length (W) is 10 cm, are reported in Table A.2.

Table A.2 *RF and ε as function of θ_{att} for silica and magnesium carbonate, if a roller with $D = 5$ cm and $W = 10$ cm is used, with a layer thickness of 100 µm and with $\sigma_{H,0} = f_c$.*

	Silica		**Magnesium Carbonate**	
θ_{att} (°)	RF (N)	ε (-)	RF (N)	ε (-)
25	373	0.16	495	0.22
20	267.4	0.20	254	0.28
15	58	0.33	49.9	0.40
12	6.8	0.47	6.8	0.53
8	1.4	0.54	1.15	0.61
5	0.2	0.64	0.32	0.66
3	0.08	0.67	0.11	0.69

Also, the final porosity (ε) of the powder layer as function of the angle of attack is reported in Table A.2.

In accordance with eq. (A.2), ε has been evaluated from the following relationship:

$$\frac{\sigma(\theta_{att})}{\sigma(\theta = 0°)} = \left[\frac{1 - \varepsilon(\theta_{att})}{1 - \varepsilon(\theta = 0°)}\right]^K \tag{A.25}$$

where the value of the angle in round brackets indicates that the mean normal stress and the porosity are evaluated at that value of the angle. $\varepsilon(\theta_{att})$ has been evaluated from the relationship:

$$\rho_b(\theta_{att}) = \rho_p \left[\left(1 - \varepsilon(\theta_{att})\right)\right] \tag{A.26}$$

As expected, the lower the θ_{att}, the lower the compression and the reduction of the porosity, and thus the lower the reduction of the bulk density of the powder layer (Table A.2).

The analysis presented here has demonstrated that the nip region cannot be avoided. In fact, the nip angle is greater than 0° for compressible powders like those examined here. In case of angles of attack very small, namely smaller than the nip angle, the powder enters directly in the nip region (Figure A.8). This condition is not convenient because there is a risk of dragging of the deposited layer, which would mean ruining the deposited and compressed layer. In fact, in the nip region there is no relative motion between the powder and the roller, which means high capacity of the roller to drag the powder.

Therefore, it is necessary to investigate which is the actual vertical stress distribution along the layer thickness, namely in y-direction (Figure A.6), and which are the conditions which could lead to inadequate compression of the whole depth of the layer. In fact, if the layer does not have sufficient strength compared to the adhesion with the roller surface, the layer or part of it could be dragged by the roller, after being compressed.

Moreover, Table A.2 has shown that by reducing the angle of attack of the powder on the roller there is a decrease of the rolling force, which is a desired result. In fact, RF has to be minimised to avoid too high shear stresses within the powder bed in the fabrication cylinder of a typical SLS machine (Figure I.1), which may compromise the integrity of the final object. Thus, small angles of attack should be used.

Appendix B: MATLAB code for the construction of wavelet power spectra

```matlab
I=imread('1.jpg'); % The powder layer image is
opened in MATLAB
G = rgb2gray(I); % Image is converted to greyscale
h=height(G) % Number of rows of G are counted
w=width(G) % Number of columns of G are counted
defaultValues_h = 0.00095; % The actual height of
the   image   is   assigned   to   the   variable
"defaultValues_h"
defaultValues_w = 0.0015; % The actual length of
the   image   is   assigned   to   the   variable
"defaultValues_w"
k1= (defaultValues_h)./(h);  % Definition of the
first calibration factor k1 i.e. real height of the
image(meter)/image heigth (pixel)
% Main code for selecting specific rows and strips
and for analysing the signals
while(1)
n= input ('insert a number from 1:h'); % User is
asked to input the strip location 'n'
m= input ('insert a number for strip thickness');
% User is asked to input the strip width 'm'
% Note that the real strip thickness is equal to
(2*m)+1
% A row vector (c) is created. The elements of c
are the means of the values of the columns belonging
to the submatrix whose rows are the ones between the
position i and j of the matrix G.
b=zeros(1,w);
for i=n-m,j=n+m
```

```matlab
  c = mean(G([i:j], :), 1);
  f=cast(c,'single');  %values  in  vector  c  are
converted to single-precision
  b=b+f;   % b is the final signal whose values are
the pixel intensities
  x = 1:w;  % x is the distance range
  figure; % figure creates a new figure window using
default property values
  subplot(3,1,1)  %  subplot  divides  the  current
figure into an 3-by-1 grid and creates axes in the
position 1
  plot(x,b)  Signal  is  plotted  as  a  function  of
distance
  axis tight % Tight fits the axes box tightly around
the data by setting the axis limits equal to the
range of the data.
  axis([1 w 0 255]) % axis specifies the limits for
the   current   axes   so   that   the x-axis ranges
from 1 to w and the y-axis ranges from 0 to 255.
  title('Signal')  %  title  "Signal"  is  displayed
above the plot
  xlabel('Distance (Pixel)') % xlabel labels the x-
axis with "Distance (Pixel)"
  ylabel('Pixel Values') % ylabel labels the y-axis
with "Pixel Values"
  yticks([0 100 200]) % yticks sets the y-axis tick
values,  which  are  the  locations  along  the y-axis
where the tick marks appear.
  [cfs,frq] = cwt(b);  % cwt turns the continuous
wavelet  transform  (CWT)  of b.   Two  arrays  are
created:  cfs  which  corresponds  to  the  wavelet
coefficients  and  frq  which  corresponds  to  the
corresponding frequencies.
  Fs =frq./k1;% Default  frequency  (1/pixel)  is
converted to the wavenumber.
  %FF = 0:Fs;
  %cwt(b)
  subplot(3,1,2)  %  subplot  divides  the  current
figure  into  an 3-by-1 grid   and  creates  axes  in
position 2.
  surface(x,Fs,abs(cfs)) % surface function creates
a    three-dimensional surface plot,    i.e.    the
scalogram. The function plots the absolute values of
each element in array cfs as heights above a grid in
the x-y plane  defined  by x and Fs.  The  colour  of
```

176

```
the surface varies  according  to  the  heights
specified by abs(cfs).
  colorbar     %     colorbar     displays     a
vertical colorbar to the right of the current axes
or chart
  axis tight
  %axis([1 w 1 Fs])
  shading flat % The shading function controls the
colour shading of  surface  and  patch  graphics
objects; flat means that each mesh line segment and
face has a constant colour determined by the colour
value at the endpoint of the segment or the corner
of the face that has the smallest index or indices.
  title('Magnitude Scalogram')
  xlabel('Distance (Pixels)')
  ylabel('Wavenumber (m^-1)')
  %ylim([0 100])
  %yticks([0 150 300 450])
  fb = cwtfilterbank ( 'SignalLength',numel(b));
  % cwtfilterbank  creates  a  continuous  wavelet
transform (CWT) filter bank. The default wavelet used
in  the  filter  bank  is  the  analytic  Morse(3,60)
wavelet, where 3 is the symmetry parameter and 60 is
the time-bandwidth.
  [tavgp,centerF]=timeSpectrum(fb,b,'SpectrumType',
'power','Normalization','pdf');
  %[tavgp,centerF]=timeSpectrum(fb,b) returns   the
time-averaged wavelet power spectrum of the signal b,
using the continuous wavelet transform (CWT) filter
bank fb,  and  the  center  frequencies.   By
default, tavgp is  obtained  by  time-averaging  the
magnitude-squared scalogram over all times. The power
of the time-averaged wavelet spectrum is normalized
to equal the variance of b.
  WN=centerF./k1; % center frequencies are converted
to wavenumbers.
  subplot(3,1,3)  %  subplot  divides  the  current
figure  into  an 3-by-1 grid   and  creates  axes  in
position 3.
  plot(WN,tavgp) % Plot of the time-averaged wavelet
power spectrum of  the  signal b  as  function  of  the
wavenumber is created.
  axis tight
  %axis([0 Fs 0 1])
  title('Power wavelet spectrum ')
```

Appendix B

```matlab
ylabel('Power')
xlabel('Wavenumber (m^-1)')
end
m1=input('Do you want to continue, Y/N [Y]:','s')
% input(prompt) displays the text in prompt and waits
for the user to input a value
if m1=='N'
break
end
end
```

178

Appendix C: Accurate reproduction of the powder in EDEM

Rather than consider spherical particles and use proper coefficient of rolling friction to account for non-sphericity of particles as a way to replicate the powder in the simulations (Zhou *et al.*, 1999), a different approach could be used.

This approach is the *clumped sphere* method (Favier *et al.*, 1999a), according to which each particle is approximated by a number of overlapping or touching spheres of different sizes. The advantage of this method is a good representation of the particles. However, in case of highly irregularly shaped particles, many spheres should be used to replicate the actual shape. As a result, the computational efficiency is very low and the method turns out to be unsuitable, unless very powerful computers are used. Therefore, this approach can be used once a good compromise between sufficient number of spheres to represent actual particles and acceptable computational efficiency is found (Markauskas *et al.*, 2010; Pasha *et al.*, 2016).

To properly reproduce the shape of particles, Morphologi G3 (Malvern Panalytical Ltd., Malvern, UK)(Figure C.1) has been used in combination with the Scanning Electron Microscope (SEM). By using Morphologi G3, a sample of 5 mm^3 has been dispersed on a holder, which can be inserted in the SEM apparatus, at an injection pressure of 5 bar, at an injection time of 20 ms and at a settling time of 60 s. All these parameters have been chosen so as to ensure uniform dispersion of particles and thus to avoid their overlapping. Then the holder has been inserted in the TM3030Plus Tabletop SEM (Hitachi, JP) under 5 kV acceleration voltage (Figure C.2). Images like those reported in Figure III.1 have been obtained.
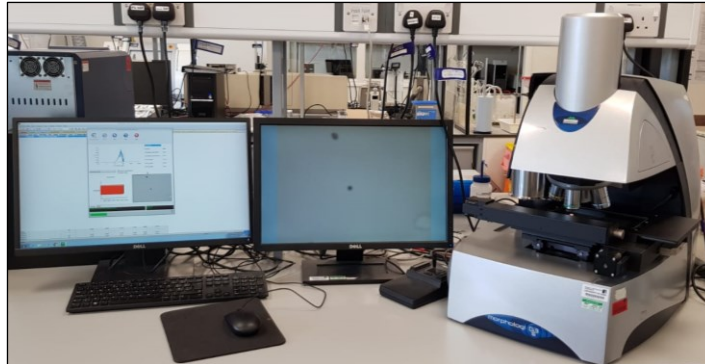
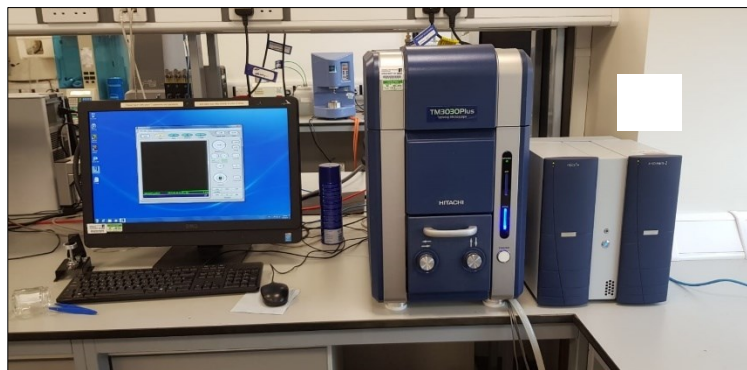**Figure C.1** *Morphologi G3 (Malvern Panalytical Ltd., Malvern, UK).*

Figure C.2 *Hitachi TM3030Plus Tabletop SEM (Hitachi, JP).*

From the SEM images, more than one thousand particles have been detected.

Morphologi G3 is able to derive the particle size distribution from the circle equivalent diameter (CE). CE is the diameter of a circle with the same exposed area of the particle. CE has been calculated looking at the surface area exposed of the dispersed particles. Based on the particle size distribution, the particles have been classified into three main size classes, as shown in Figure C.3.
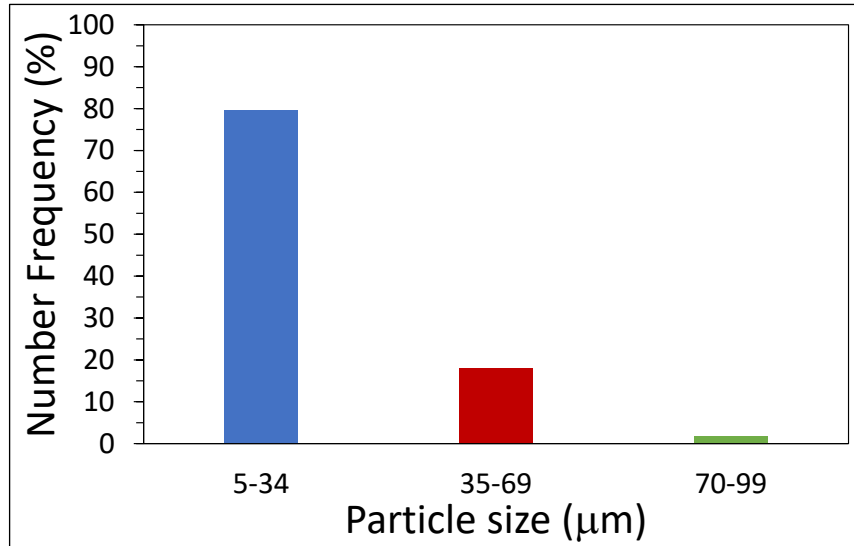
Figure C.3 *Particle size distribution (CE diameter) of polyamide 6 powder with three size classes. Blue bar: 5 μm<CE<34 μm; Red bar: 35 μm<CE<69 μm; Green bar: 70 μm<CE<99 μm.*

For each size class, 5 particles have been randomly selected from the SEM images for simulating different shapes.

By using the ImageJ software, from three to twelve circles of different diameters have been used to cover the surface area exposed of the selected particles (Figure C.4). In EDEM, a sphere with the same diameter of the circle has been centred in the same position of the circle. Therefore, each particle, chosen as a reference for a certain size class, has been approximated to overlapped spheres, whose number depends on the complexity of the particle shape and on the desired accuracy in the reproduction of the actual particles (Figure C.5).
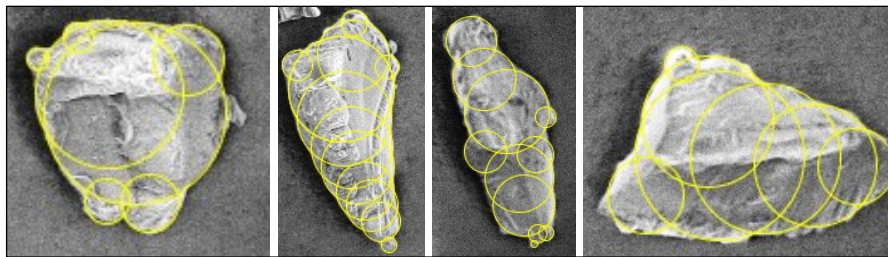

Figure C.4 *Approximation of the surface area exposed of the particles with circles (yellow in the figure).*
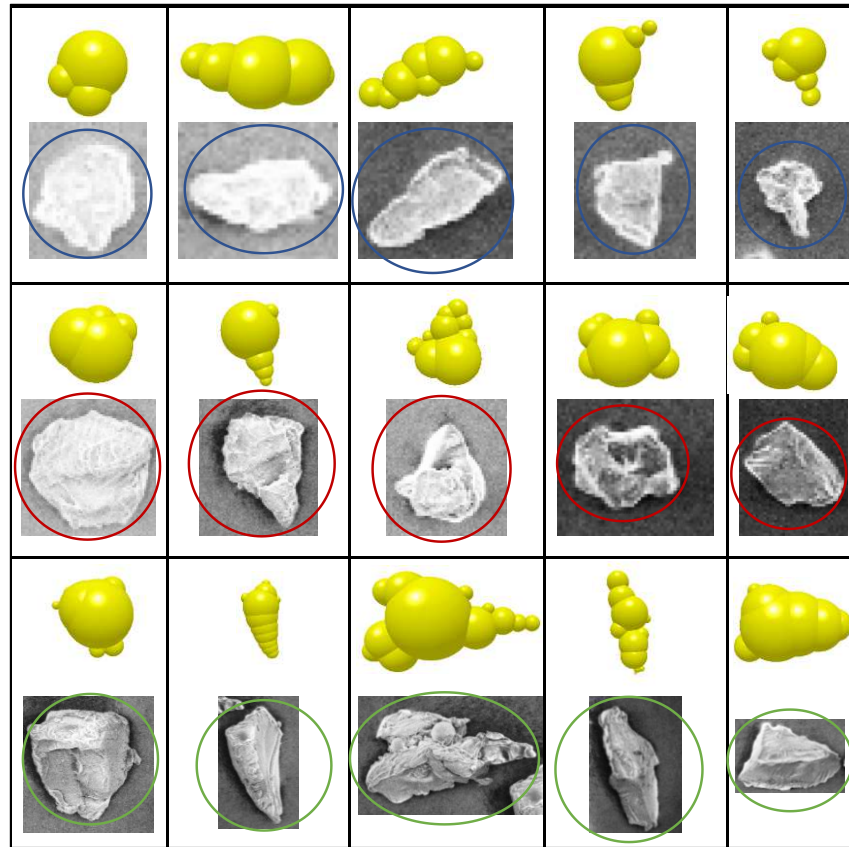
Figure C.5 *Particle shapes for DEM simulations. Each size class is represented by a coloured curve: 5 blue curves (5–34 µm), 5 red curves (35–69 µm) and five green curves (70–99 µm).*

This approach has been tried in the simulations for calibration of the model parameters but the simulation time dramatically increased because of the size of the smallest spheres and of the increase of the number of particles in the simulation, as described in paragraph IV.4.1. Therefore, the clumped sphere approach, for the case of the polyamide 6 powder, seems to be not suitable unless very powerful computers are used.

Appendix D: Measurement of the characteristic length of roughness for additional simulations

Images of powder layers obtained with simulations, which are not reported in paragraph V.2.2, instead, are reported in Figure D.1.
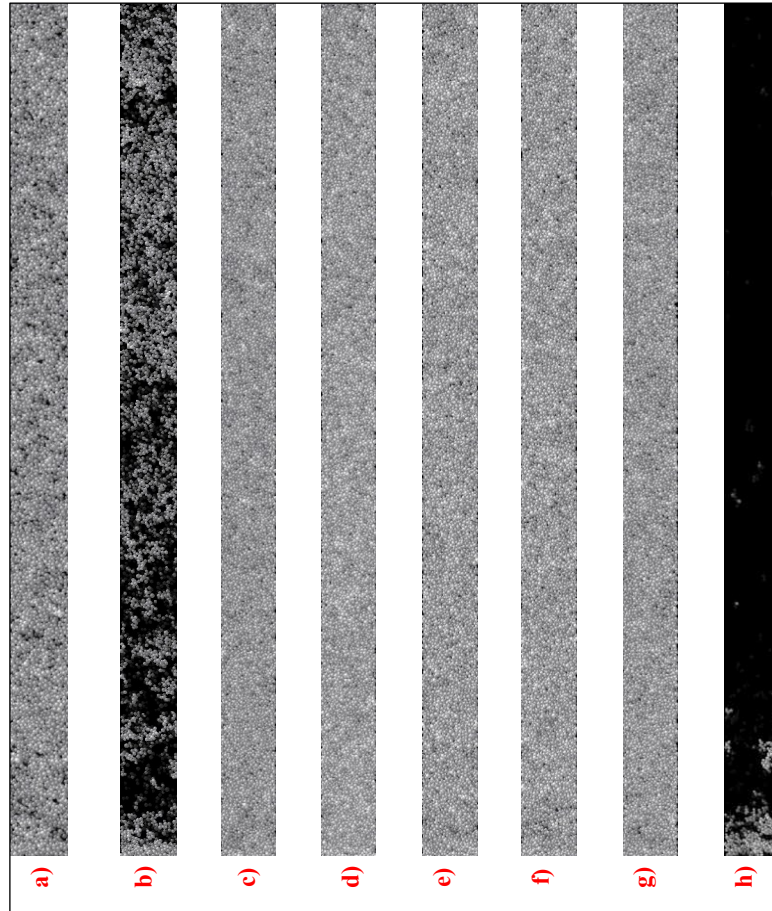
Figure D.1 *Images of the powder layer surface for simulations number: a)1; b)3; c)6; d)7; e)8; f)9; g)10; h)11. For reference see Table V.3.*

In case of simulation 3 (Figure D.1b) and 11 (Figure D.1h), portions of the image where there are particles have been analysed with MATLAB to get the power spectra.

In case of simulation 3, the portions of the powder layer that have been considered are those reported in Figure D.2.

Values of the characteristic length (c.l.) of roughness in correspondence of the peak value of the power spectrum and of the two-thirds of the peak value (Min and Max) are reported for the seven portions of the layer together with the average values in Table D.1.
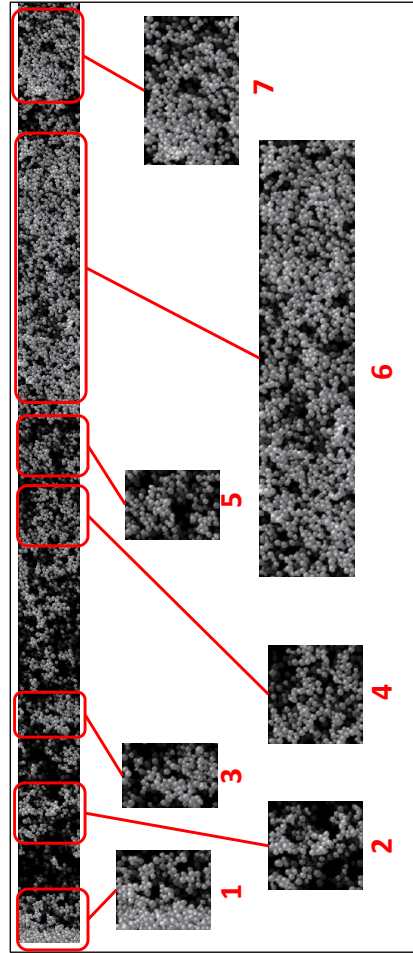
Figure D.2 *Different portions of the powder layer (1-7) related to simulation number 3 (Table V.3) analysed with MATLAB to get the wavelet power spectra.*

In case of simulation 11, the portions of the powder layer considered are those reported in Figure D.3 and the values of c.l. of roughness are reported in Table D.2.

Table D.1 *Characteristic lengths (c.l.) of powder surface roughness in correspondence of the peak value of the power spectrum and of the two-thirds of the peak value (Min and Max) for the 7 portions of the powder*

layer of Figure D.2 with the average and the standard deviation values among those obtained for the 7 portions.

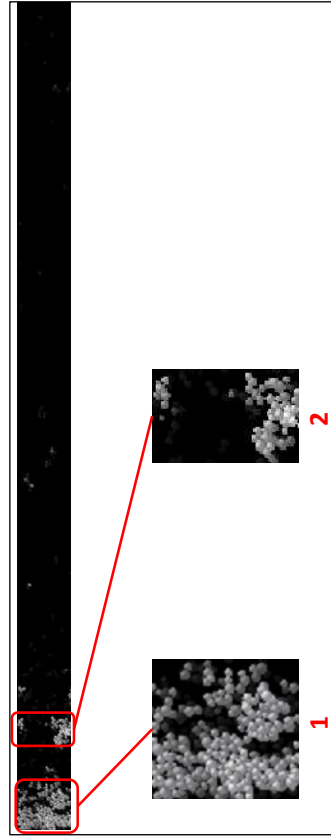| Portion number	*c.l. of roughness*		
	Min (μm)	Peak (μm)	Max (μm)
1	141	163.2	188.7
2	256	265	265
3	127	152.2	177
4	110	123.6	210.5
5	103	123.6	144.9
6	127	374.8	645.2
7	208	265	400
Average	153.1	209.7	290.2
Standard deviation	57	94.6	177.6

Figure D.3 *Different portions of the powder layer (1-2) related to simulation number 11 (Table V.3) analysed with MATLAB to get the wavelet power spectra.*

Table D.2 *Characteristic lengths (c.l.) of powder surface roughness in correspondence of the peak value of the power spectrum and of the two-thirds of the peak value (Min and Max) for the 2 portions of the powder layer of Figure D.3 with the average and the standard deviation values among those obtained for the 2 portions.*

| Portion number | *c.l. of roughness* | | |
	Min (μm)	Min (μm)	Max (μm)
1	206	230.7	265.1
2	145	163.2	174.9
Average	175.5	197	220
Standard deviation	43.1	47.7	63.8

Appendix D

The average values of c.l. of roughness obtained from both the simulations are not consistent with the values obtained with all the other simulations and which are reported in Figure V.9. In fact, even if the powder does not deposit easily along the spreading direction as demonstrated by Figure D.2, Figure D.3 and by the lowest values of bulk density and the highest values of porosity compared to the other simulations (Figure D.4), the final c.l. of roughness is not the highest one, as might be expected. In fact, c.l. of roughness turns out to be close to the one obtained in case of simulation 1, which is reported in Figure V.9.

Therefore, in the event that large portions of the deposition tray remain not covered by the powder, namely large portions of the deposition tray remain black, the analysis based on wavelet power spectra does not always provide reliable results.
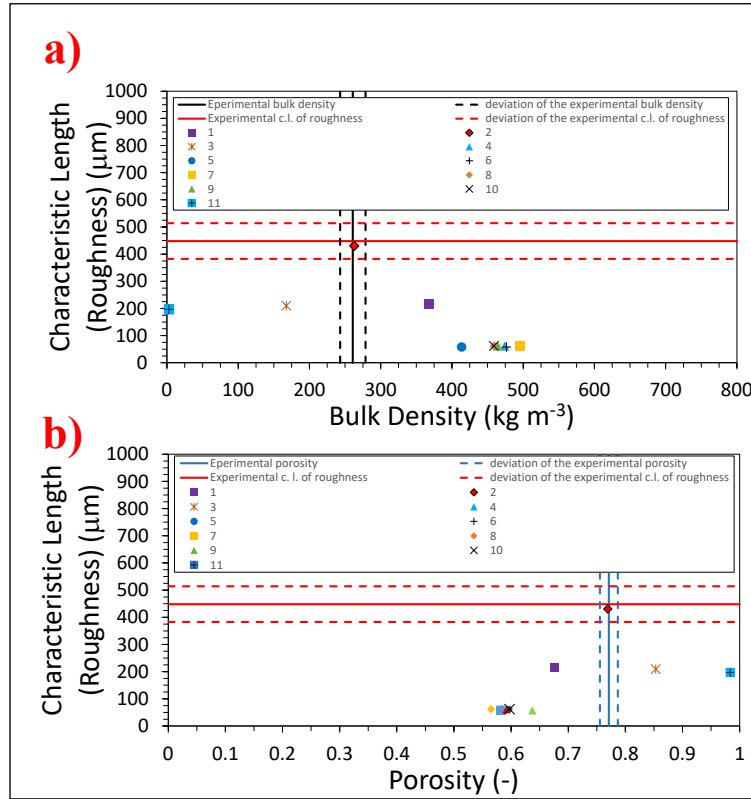

Figure D.4 *Characteristic length of roughness as function of bulk density (a) and of porosity (b) for all the simulations tried and comparison with the experimental values. Each simulation is represented by a number. Details about the values of the parameters used are reported in Table V.3. Red, black and blue solid lines correspond to the experimental characteristic length (c.l.) of roughness, bulk density and porosity, respectively.*

Hyphenated lines of the same colour correspond to the deviation of the aforementioned properties

Appendix E: Other attempt of analysis of the powder layer

Before adopting the procedure described in paragraph IV.6.1, a different approach has been tried with the purpose of reconstructing the simulated powder layer and applying the same lighting conditions, that have been used to show shadows on the powder layer surface obtained with the experiments.

Data saved from the simulations have been used to recreate the whole powder layer.

In particular, in EDEM the powder layer has been divided into 6 geometry bins with the aim of reconstructing 3 subsequent portions of the powder layer. By doing so, data of particles inside the bins have been extracted. Each bin (Figure E.1) is a box with a length of $2.5 \cdot 10^{-3}$ m, a width and a thickness like those of the powder layer, namely $95 \cdot 10^{-5}$ m and $300 \cdot 10^{-6}$ m, respectively.
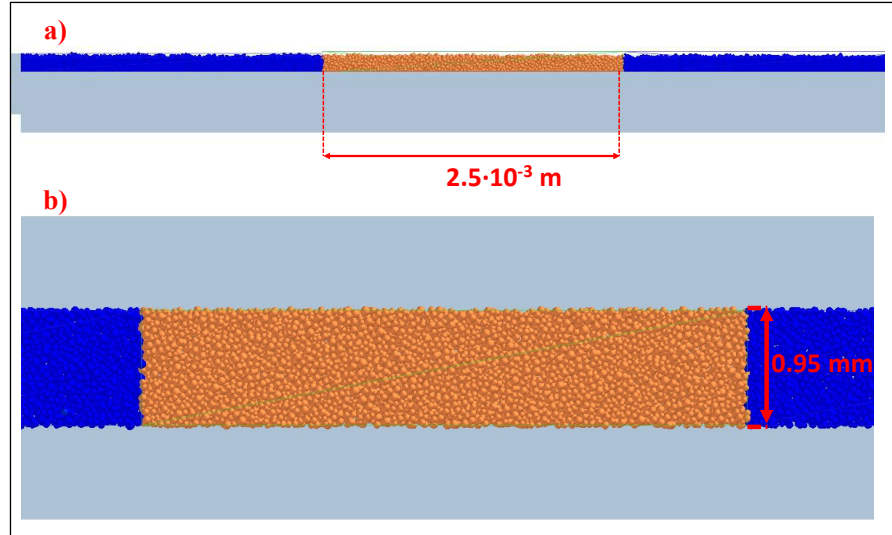
Figure E.1 *a) Side and b) top view of one bin.*

In each bin, data of positions x, y and z, and of diameter of the particles have been extracted as .csv files from the EDEM's Export Data Dialog (Figure E.2).
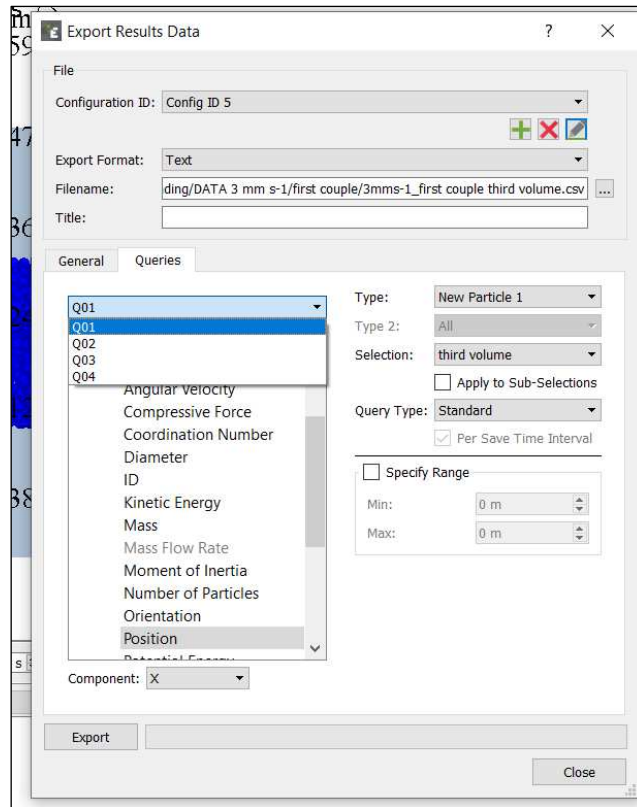
Figure E.2 *Extraction of data of positions (x, y and z) and diameter of all the particles in a bin.*

Data reported in each of these files have been copied in a different .csv file in an appropriate form so as to be opened in the *Rhinoceros* software (seventh version) by means of a *Phyton* script.

In each .csv file, data have been reported in column A but in different rows (Figure E.3): in the first row, the time of the simulation at which the data have been extracted; in the second, third and fourth rows, the position x, y and z of the particles in a specific bin, respectively; in the fifth row the diameter of each particle in that bin.

Appendix E

▲	A	B	C	D	E	F	G	H	I
1	TIME:,2.30387								
2	Q01 : Particle Position X:,0.169366,0.168806,0.171626,0.168481,0.170734,0.167674,0.170120,0.								
3	Q02 : Particle Position Y:,0.001248,0.000857,0.000982,0.001227,0.001292,0.001174,0.001518,0.								
4	Q03 : Particle Position Z:,0.063150,0.062966,0.063012,0.063062,0.063014,0.063062,0.062968,0.								
5	Q04 : Particle Diameter:,0.000056,0.000048,0.000056,0.000059,0.000055,0.000079,0.000051,0.0								
6									

Figure E.3 *Creation of a .csv file for the reconstruction of the portion of the powder layer (bin) with Rhinoceros. Data have been reported in 5 different cells of column A.*

The Phyton script, based on the data about the position and the diameter of each single particle, reconstructs the portions of the powder layer, which correspond to different bins (Figure E.4). The script has been downloaded from the EDEM User Forum.
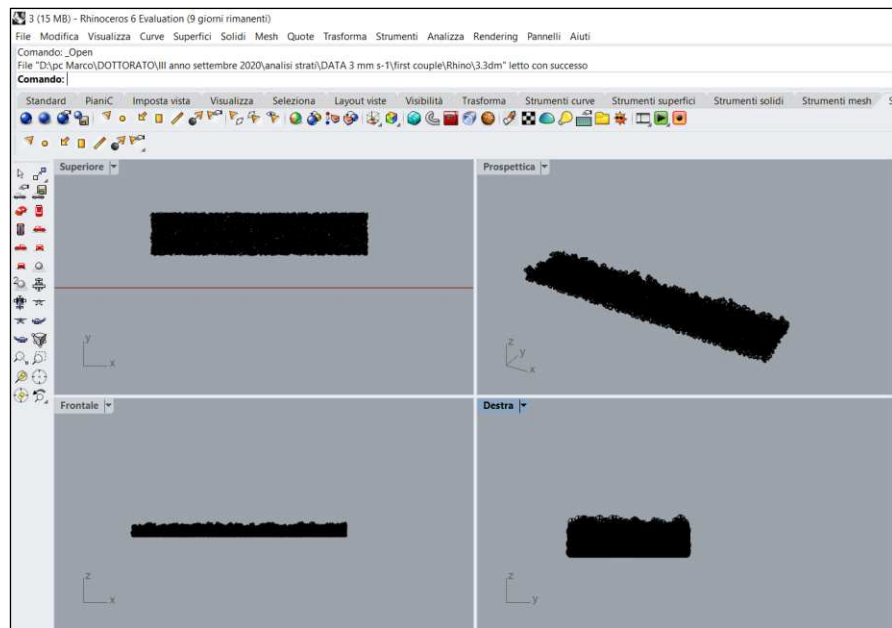

Figure E.4 *Portion of the layer, corresponding to a specific bin, is reconstructed by the Rhinoceros software.*

From Rhynoceros, a .stl file for each portion of layer reconstructed has been created in order to be opened in the *SolidWorks* software.

In SolidWorks, it has been possible to illuminate the powder surface with a directional light, trying to reproduce the same lighting condition of the experiments. In fact, the recreated layer has been illuminated under a light

194

with an inclination 45° with respect to the powder layer and along the spreading direction.

For each portion of the powder layer, an image of the surface has been saved as .tif file from SolidWorks (Figure E.5). In ImageJ, the same procedure as the one described in the paragraph III.4 has been adopted to cut out a rectangle with the sides of the same desired dimensions of the layer, namely a length of $2.5 \cdot 10^{-3}$ m and a height of $95 \cdot 10^{-5}$ m.

Then the three images have been joined to reconstruct the whole powder layer.

The final image has been opened in Microsoft Paint to get the same height in pixels of the images obtained from the experiment.

In the end, the images have been analysed by means of MATLAB, as described in paragraph III.4.2.
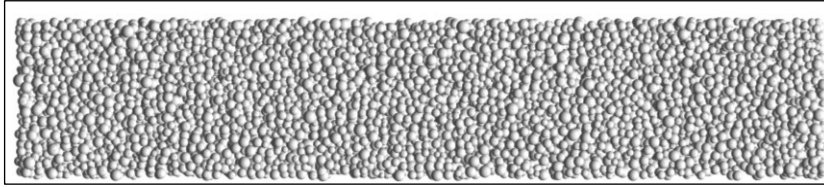

Figure E.5 *a) Image of a portion of the powder layer taken from the SolidWorks software.*

The whole procedure adopted to analyse images of simulated powder layers is reported in Figure E.6.
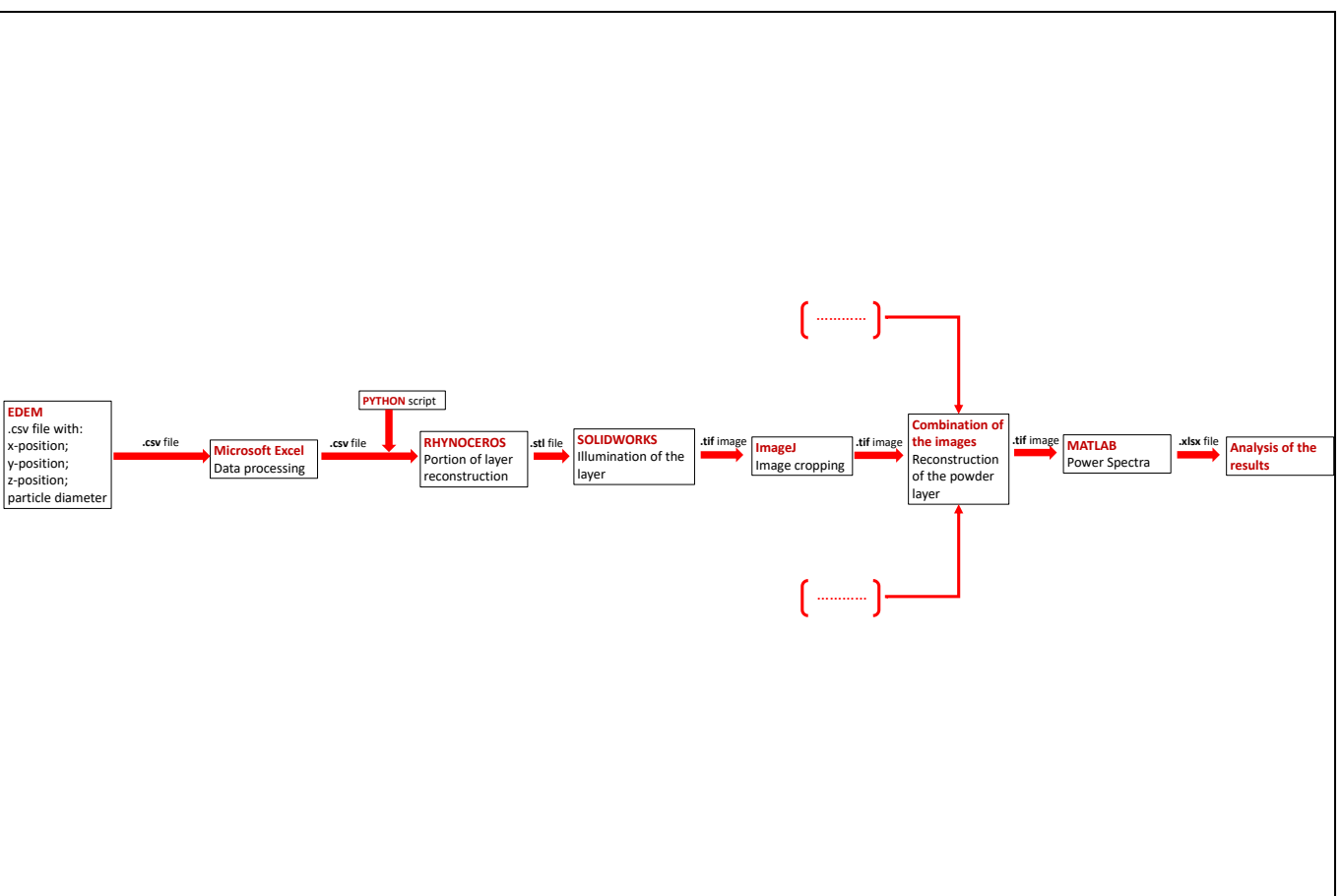
Figure E.6 *Steps for reconstruction and analysis of the powder layer images. Dots in brackets represent the repetition of the procedure for the other two images, i.e. the other two portions of the powder layer.*

However, if the wavelet power spectrum is applied to the images obtained from the simulations (Figure E.7), the resulting c.l. representative of the powder surface roughness is always approximately equal to the average particle (D_{50}) (Table E.1). In Figure E.7 and Table E.1 are reported only two examples but the results are almost the same for all the simulations.

If we look closely at one of these images (Figure E.8), it is immediately clear that this result depends on the shadows shown on the surface. In fact, by using SolidWorks it is possible to have for each particle only the shadows obtained because of the grazing light but it is not possible to show the projection of shadows of the surrounding particles. It seems that each particle is not affected by the presence of the other particles, that is the light projected on each particle is not shielded by other particles in front or above. It is as if all the particles are at the same height and are all exposed to the light in the same manner. As a result, the characteristic length obtained by the power spectrum roughly corresponds to the particle diameter because the most frequent characteristic length is that of the dark shadow on each particle, which evidently has approximately the same dimension of the particles.
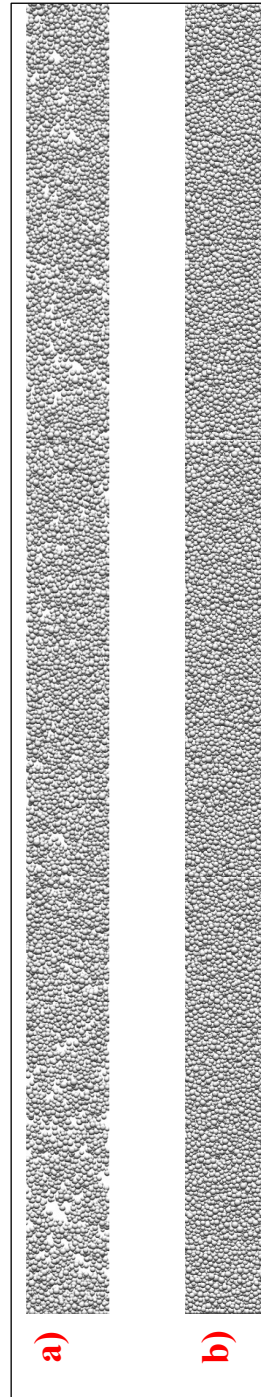
Figure E.7 *Top view of the powder layer reconstructed with SolidWorks in case of simulation number 2 (a) and 4 (b).*

Table E.1 *Characteristic lengths (c.l.) of powder surface roughness in correspondence of the peak value of the power spectrum and of the two-thirds of the peak value (Min and Max) for simulations number 2 and 4. For details about the simulations see Table V.3.*

	c.l. of roughness		
Simulation number	**Min (μm)**	**Min (μm)**	**Max (μm)**
2	43.4	57.7	77.5
4	42.8	61.8	79.1

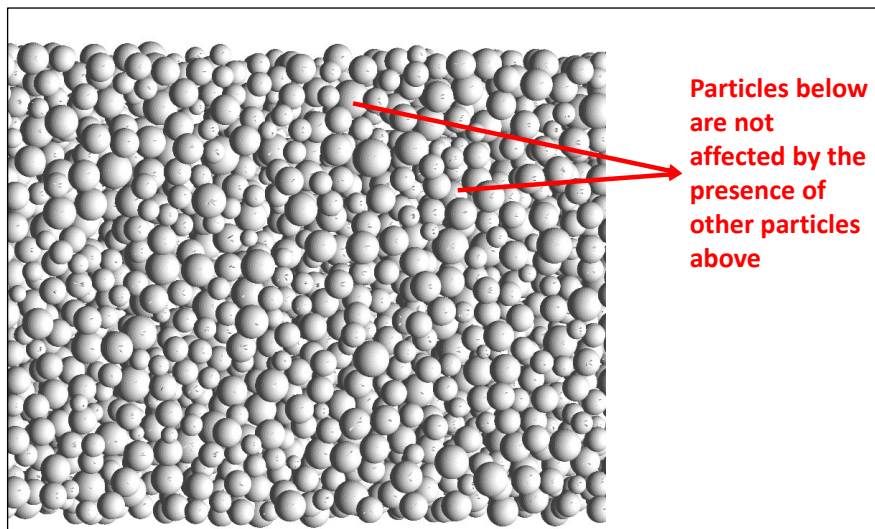Particles below are not affected by the presence of other particles above

Figure E.8 *Close-up image of the powder layer showing the shadows on the particles due to grazing light.*

Therefore, the three-dimensional reconstruction of the powder layer has the advantage of seeing the exact arrangement of the particles in the space but does not allow to highlight the surface quality of the deposited powder layer. Moreover, this method is time-consuming compared to the one used and described in paragraph IV.6.1. In fact, due to the large amounts of data to be managed by Rhinoceros and SolidWorks, the procedure requires a lot of time and unless powerful computer are used, it is necessary to reconstruct single portions of the powder layer before joining the final images.